Dynamics of sub-volcanic systems in sedimentary basins and related mechanisms of host rock deformation

by

Tobias Schmiedel

THESIS

for the degree of

Philosophiae Doctor

Faculty of Mathematics and Natural Sciences

University of Oslo

September 2018

Supervisors:

Dr. Olivier Galland

PGP-NJORD, Department of Geosciences, University of Oslo, Norway

Dr. Sverre Planke

Centre for Earth Evolution and Dynamics (CEED) Centre of Excellence, Department of Geosciences, University of Oslo, Norway and Volcanic Basin Petroleum Research AS (VBPR), Oslo, Norway

Acknowledgements

In July 2015 I started here at the University of Oslo at PGP (Physics of Geological Processes). Now, three years later I am about to finish my PhD here at the newly founded centre of NJORD. The name change of the host institution symbolizes only one of the many changes in my life during these last years. I remember proudly presenting my first twelve minute presentation for a conference in front of the Volcano group, just to get it afterwards word by word dissected in a more than three hour long lasting discussion. Since that time I have grown, not in the least due to the support from my two supervisors Olivier Galland and Sverre Planke, and from the Volcano guys: Frank Guldstrand, Øystein Haug, Alban Souche, Håvard Bertelsen, Ole Rabbel and Ben Rogers.

My greatest thanks goes to Olivier: thanks for always making time when I came knocking your door for a "short question". I am thankful for your advice and support in all the good and not so good aspects a PhD project has to offer. Sverre, thank you for your support during the seismic part of the project. I learned from you how to deal with short deadlines. Special thanks goes to the Volcano guys, my friends and officemates: Frank, thanks for always having an open ear for discussions, sharing the stages of the PhD and bringing some positive vibes into the office. Øystein, thanks for the geology-physics knowledge exchange and the Audi-driver jokes which always managed to cheer me up. Alban, during my first year 90% of our discussions left me more confused than I was before, however, over time I learned to understand your input and I am thankful for your help with MatLab. Håvard, Ole and Ben, thanks for the support in the laboratory, the talks about the "seismic stuff", minerals and all the other more or less important things in the world.

Thanks to all the great friends and colleagues at PGP/NJORD and the Department of Geoscience who made the daily life here in Oslo in and outside of university a pleasure – it would have been so much harder and less fun without you. Big thanks also to my friends in Germany who came to visit or always tried to meet up as soon as there was a chance. I am thankful to my parents and my sister for being there and supporting me, even when supporting me was not always easy. Finally, a major thanks to Anne, for sharing the joy and hardships in- and outside of the PhD life as the most important person in my life since more than a year.

Abstract

Voluminous magmatic intrusions in sedimentary basins worldwide are investigated, amongst others for their mechanical deformation of the host rock. Common features of these magmatic systems in the Earth's brittle crust are tabular intrusions ranging from thin sheet intrusions (sills, saucer-shaped sills, cone sheets) to thicker, or massive, intrusions (domed and punched laccoliths). Logically, this diversity of intrusion shapes should reflect the different emplacement mechanisms caused by contrasting host rock and magma rheologies. However, the majority of the current models for tabular intrusion emplacement assume that the host rock behaves purely elastic. In contrast, numerous field observations and seismic data show that natural rocks are actually elasto-plastic materials which are prone to shear failure. This thesis is one of the first to investigate the effect of cohesion (strength) of the natural host rocks with Mohr-Coulomb properties on magma emplacement. I first analysed the Tulipan sill (mid-Norwegian margin) and its surrounding, sedimentary host rock through 3D seismic interpretation. This is followed by laboratory experiments using dry, granular model rock of variable cohesion that satisfy a Mohr-Coulomb-type failure criterion.

The 3D seismic case study, on data of the Tulipan sill (c. 56 Ma) reveals a dome structure and hydrothermal vent complexes (HTVCs) above a saucer-shaped intrusion geometry. Further, the 3D seismic interpretation of five horizons in the Paleogene-Cretaceous sedimentary host rock shows that the (so far common) assumption of a purely elastic overburden cannot explain the observed dome and the occurrence of the HTVCs. Thus, to explain these structures, I infer that a combination of different host rock deformation mechanisms, including (1) elastic bending, (2) shear failure and (3) differential compaction, is needed.

To test these mechanisms for intrusion emplacement I then performed a series of scaled laboratory experiments injecting model magma (Végétaline oil) into dry, granular Mohr-Coulomb model hosts of variable cohesion. The laboratory results corroborate the 3D seismic interpretation and show that both sheet and massive tabular intrusions indeed cause inelastic deformation and shear failure of their overburden. The shear failure localises along an inclined damage zone triggered by an initial sill with a critical radius R, which scales linearly with the overburden's cohesion. Two alternative scenarios are then possible: (1) the overburden is sufficiently cohesive to allow for opening of a planar fracture in the subsurface to accommodate viscous magma flow along the shear damage zones, leading to the emplacement of inclined sheets, or (2) the overburden is not cohesive enough, so the sill inflates and lifts up the overburden along shear zones to form a massive intrusion.

To summarize, my results show that the assumption of elastic overburden is an oversimplification. Instead, the emplacement of sheet and massive tabular intrusions are parts of one mechanical regime, in which the Mohr-Coulomb behaviour of the Earth's brittle crust plays an essential role. This thesis contributes to the general understanding of magmatic plumbing systems and their physical mechanisms controlling the formation of

magmatic intrusions. Finally, this will help to better understand the consequences of magma emplacement for the surrounding host rock, e.g. permeability, deformation, volcanism. This has implications for geo-hazard forecast and prevention associated with volcanoes as well as for the exploration of potential hydrocarbon and geothermal systems in the sedimentary host rock around magmatic intrusions.

Abstract (plain language)

The current 2018 Kilauea fissure eruption on Hawaii shows us the danger and unpredictability of active volcanoes. Volcanoes are the "taps" for the worldwide occurring flow of molten rock in the subsurface. Molten rock in the underground is called magma. It uses an existing plumbing system to move from depth towards the Earth's surface, where the "pipes" are interconnected cracks and/or other weak structures, such as soft rocks. When magma pressures become too high, the magma will leave the existing system and create new pathways to flow through. These new pathways in the Earth's shallow crust (<6 km deep) exhibits various shapes, ranging from thin plates and saucer-shaped to massive bell- or piston-like bodies. What controls this broad variety of shapes? How do the rocks in the Earth's crust make space for the incoming magma from depth?

Many active volcanoes and their underground are continuously monitored, and still we know very little about the physical processes that lead to what we see in the field and in seismic data ("images of the underground"). Most laboratory and computer-based models used today, explain magma flow through the Earth's crust like a knife cutting through a block of jelly. However, these models cannot reproduce the full natural diversity of magma body shapes. Moreover, observations of natural rocks of the Earth's shallow crust commonly show breaking and crumbling when magma forces its way through.

To overcome this mismatch between (1) the elastic jelly-like deformation in models and (2) the breaking and irreversible deformation in nature, I investigated in this thesis the effect of weak or strong rocks on the shape of magma bodies in the subsurface. I used high-quality 3D seismic data of a natural magma body located under the ocean floor of the Norwegian Sea, and tested experimental models in the laboratory. These scaled models simulate the complex properties of Earth's shallow crust by using various dry powders as model rock.

As a more general result, my laboratory experiments suggest that thin plate and saucer-shaped magma bodies form in strong rocks, whereas massive bell- or piston-like bodies form in weak rocks. All experiments result in a dome structure above the forming body in the underground. These dome structures and the sometimes bread crust-like cracks within them cannot be explained by a jelly-like behaviour or the surrounding material. Thus, my results suggest that dominant irreversible breaking and only a minor component of elastic deformation led to the observed structures in both the experiments and the analysed seismic data, respectively.

This laboratory setup is worldwide the first to simulate a wide range of shapes similar to the ones observed from magma bodies in nature. In future, the knowledge gained from our models may help to improve the forecast of potential risks related to active volcanoes, such as the 2018 Kilauea eruption on Hawaii. Moreover, the knowledge derived from this thesis about the deformation of rocks around magma bodies may help to improve the strategic search for potential oil/gas/mineral-resources and/or the exploitation of geothermal energy associated with volcanic areas.

Table of Contents

1 Introduction

Since the late 19th century, several voluminous magmatic systems in sedimentary basins have been described from both field and seismic data (e.g., Gilbert, 1877; Corry, 1988; Magee, et al., 2016). Multiple studies have demonstrated that magmatic intrusions emplaced in sedimentary basins have major impacts on the structural and thermal evolution of the sedimentary host rock (e.g., Johnson and Pollard, 1973; Svensen et al., 2004; Sydnes et al., 2018). Thus, these magma-host rock interactions can have significant consequences for the evolution of hydrocarbon systems in the sedimentary host rock (Senger et al., 2017; Rodriguez Monreal et al., 2009; Spacapan, et al., 2018). However, our current understanding of magmatic systems and the incomplete knowledge about the mechanical processes leading to intrusion-induced structures in the sedimentary host rocks (fault/fracture patterns, dome structures, etc.), render exploration more challenging. This lack of knowledge is caused by the inaccessibility of these structures in the subsurface and the limited data mainly provided by seismic and borehole data (Planke et al., 2018).

Together, seismic acquisition and interpretation are amongst the most commonly used methods in geosciences to image the subsurface, especially in the field of hydrocarbon exploration. 2D seismic studies are common since the first half of the 20th century, and in the last 30 years the number of 3D seismic acquisitions has increased rapidly due to improved infrastructure for digital processing. However, 2D seismic studies come with a number of significant uncertainties, i.e., they provide only the apparent structural dip and a relatively coarse lateral resolution, and correlation of stratigraphic and structural features is difficult due to the large spatial grid spacing of 2D seismic lines (10's of kilometres). Modern 3D seismic data shows not only highly resolved geometrical information on geological structures, but also provides seismic attributes to aid the interpretation of their physico-chemical properties (e.g., Klarner and Klarner, 2012).

The first part of this thesis presents a high-quality 3D seismic dataset from the Møre Basin on the mid-Norwegian margin to understand the deformation of the host rock induced by the emplacement of an igneous sill complex (Tulipan sill). The emphasis is on the spatial correlation between the intrusion geometry and the overlying dome structure with associated hydrothermal vent complexes (HTVCs), as well as their age (Chapter 3.1). The limitations of the 3D seismic data are that it provides (1) only large-scale deformation features, ranging from several meters to kilometres, and (2) snapshots of the final shape and not the evolution in time.

To overcome these limitations, and to better understand the evolution of the emplaced igneous intrusions, we use laboratory experiments. Analogue models came in use over 200 years ago, with the aim to reproduce and explain geological observations in the field (Hall, 1815). During the last 15 years, the development of new materials, better control on material properties, as well as high-resolution monitoring techniques, have transformed analogue models into a versatile tool in geosciences. Today, these quantitative laboratory models provide significantly improved control on the parameters used to model physical

processes of natural systems. In addition, the integration of numerical simulations led to a shift from a mere tool for qualitative visualisation to an established quantitative method (Galland et al., 2018a; Kavanagh et al., 2018).

In the second part of this thesis I use such a modern quantitative laboratory model to evaluate magma emplacement into the upper crust. Rocks in nature show a large variety in strength (e.g. shale vs sandstone) generally described with the cohesion and the angle of internal friction. Field studies suggest that this variety in strength is a likely candidate to control the mechanisms through which the host rock accommodates the space needed for an emplacing magmatic intrusion (Figure 1.1). The laboratory model features intrusions of solidifying model magma into a granular model host rock similar to natural rocks. Thus, the laboratory setup enables a quantitative assessment of the effect of variable host rock strength (i.e., cohesion) and depth on the intrusion geometry (Chapter 3.2).

a) Sill intrusion emplaced through tensile opening of the host rock
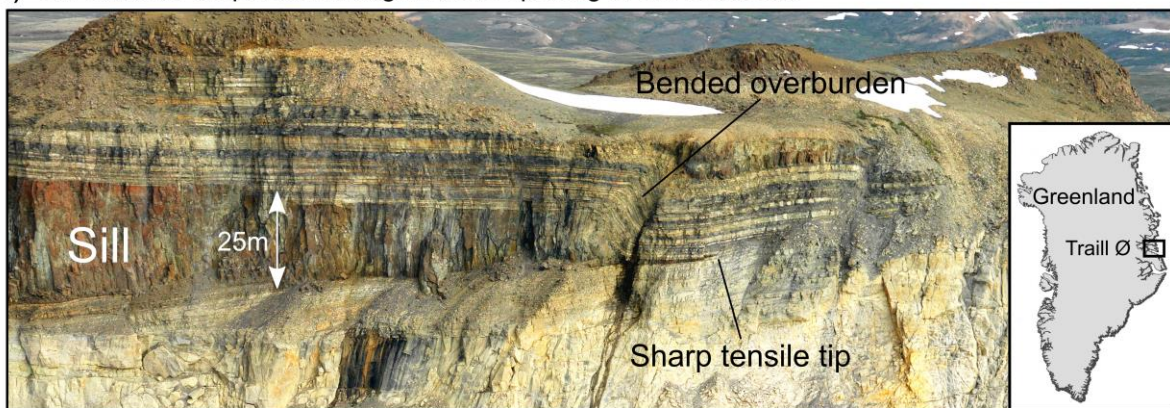
b) Sill intrusion emplaced through shear failure of the host rock
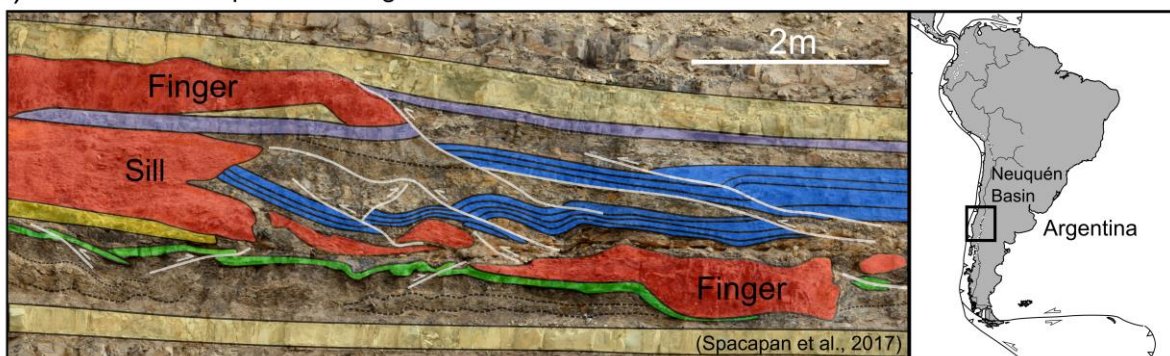

Figure 1.1: Field photos showing various features of host rock deformation to accommodate the emplacement of a sill intrusion. (a) Host rock behaves elastic; tensile opening of a fracture and bending of the host rock around the sill (Graphic adapted from Galland et al., 2018). **(b)** Host rock behaves plastic; broken (shear fractures) and stacked host rock ahead of the sill (Graphic modified after Spacapan et al., 2017; Galland et al., 2018).

The combination of geological, physical and geophysical methods in this multidisciplinary work improves our current understanding of the evolution of magmatic systems and their impact on the host rock in sedimentary basins, overcoming the limitations

of each single method. The high quality 3D seismic data provides a natural case study of structural and mechanical features associated with an intrusion in the subsurface. The laboratory models simulate the emplacement of an intrusion as well as the resulting structures, and can be used to verify and understand the mechanisms behind the structures in nature as observed by seismic data. In addition, the findings from this thesis may have implications for the following societal and industrial interests:

- *Society:* Upgraded risk assessment of potential geohazards related to volcanic systems, due to the enhanced understanding of the underlying magmatic plumbing system.

- *Resource industry:* Enhanced exploration prospects in petroleum and ore industry, due to better understanding of the subsurface structures and mechanical deformation related to magmatic systems.

- *CO_2 storage:* Information on additional CO_2 storage reservoirs in the structures resulting from magmatic intrusions.

- *Environment:* Contribution to the knowledge about historic climate change/mass extinction events, related to former large-scale greenhouse gas release triggered by large igneous systems, due to the increased understanding of fluid pathways associated with the emplacement of magmatic intrusions.

2 Scientific background

Worldwide, numerous sedimentary basins are known to host significant volumes of primary emplaced igneous rocks (Figure 2.1; Table 2.1; Breitkreuz and Petford, 2004; Jerram and Bryan, 2018; Planke et al., 2018). In these so-called *volcanic basins* (Planke et al., 2005), the ascent of magma forms interconnected networks of igneous intrusions, known as magmatic/volcanic plumbing systems (Cartwright and Hansen, 2006; Airoldi et al., 2016; Eide et al., 2016). In general, magmatic plumbing systems are constructed from a variety of different intrusion shapes, such as dykes, sills, cone sheets, laccoliths, plugs, plutons, etc. (Figure 2.2; Jerram and Bryan, 2018; Kennedy et al., 2018; Burchardt, 2018). The emplacement of these igneous intrusions in the Earth's crust may result in significant mechanical deformation and brittle failure of the host rock (Chapter 2.2; e.g., Cartwright and Hansen, 2006; Wilson et al., 2016). In addition, multiple field studies have shown that igneous intrusions are preferably emplaced along stratigraphic boundaries in the host rock, and into weak lithologic layers (e.g., Schofield et al., 2012; Schofield et al., 2014; Eide et al., 2016), highlighting the potential impact of stratigraphy on intrusion shape.

Table 2.1: List of selected studies on volcanic basins.

Location	Reference
Volcanic basins	
Karoo Basin (South Africa)	Chevallier et al. (2001)
	Galerne et al. (2011)
	Svensen et al. (2012)
	Svensen et al. (2018b)
Møre and Vøring Basins (Norway)	Berndt et al. (2001)
	Abdelmalak et al. (2015)
	Abdelmalak et al. (2016b)
	Planke et al. (2017)
Saar-Nahe Basin and Halle Basin (Germany)	Lorenz and Haneke (2004)
	Breitkreuz et al. (2009)
	Schmiedel et al. (2015)
	Słodczyk et al. (2015)
	Breitkreuz et al. (2018)
Volcanic basins prospected for hydrocarbon exploration	
East China Sea Shelf Basin (China)	Cukur et al. (2010)
Exmouth Sub-Basin(Australia)	Magee et al. (2017b)
Faroe-Shetland Basin (United Kingdom)	Rateau et al. (2013)
	Mark et al. (2017)
	Schofield et al. (2017)
Møre and Vøring Basins (Norway)	Planke et al. (2005)
	Polteau et al. (2008b)
	Schmiedel et al. (2017b)
Neuquén Basin (Argentina)	Rodriguez Monreal et al. (2009)
	Witte et al. (2012)
	Delpino et al. (2014)
Rockall Basin (Ireland – United Kingdom)	Magee et al. (2014)
Tunguska Petroleum Basin (Russia)	Kontorovich et al. (1997)

Why study igneous intrusion in sedimentary basins specifically? First, a large amount of the Earth's surface consists of sedimentary rocks (Figure 2.1). Moreover, especially in combination with intruded igneous intrusions, sedimentary rocks are of economic interest due to their high potential for hydrocarbon reservoirs, mineral deposits and geothermal energy. Third and last, field and seismic methods used for the exploration profit from the large lithological contrast of magmatic intrusions in a sedimentary environment, i.e., colour, composition, age, density, etc., and thus can provide excellent data.

In particular, all over the world, onshore and offshore, volcanic basins are explored for hydrocarbons (Figure 2.1; Table 2.1; Potter and Konnerup-Madsen, 2003; Schutter, 2003b, a). The interaction between the intruding magma and the organic-rich sedimentary host rock may have significant effects on the development of potential petroleum systems (Senger et al., 2017; Jerram and Bryan, 2018): (1) mechanical deformation may lead to dome structures above the intrusions, acting as oil and gas trap (Hansen and Cartwright, 2006; Jackson et al., 2013; Magee et al., 2014), (2) space for the intrusion accommodated in the host rock may enhance the development of fracture networks, increasing locally the permeability of the host rock (Witte et al., 2012; Agirrezabala, 2015; Senger et al., 2015; Zhang et al., 2017), and (3) heat of the intrusion may locally mature the organic matter in an organic-rich host rock, generating oil and/or gas (Table 2.2; Berndt et al., 2016; Canales et al., 2017; Peace et al., 2017; Spacapan et al., 2018; Sydnes et al., 2018).
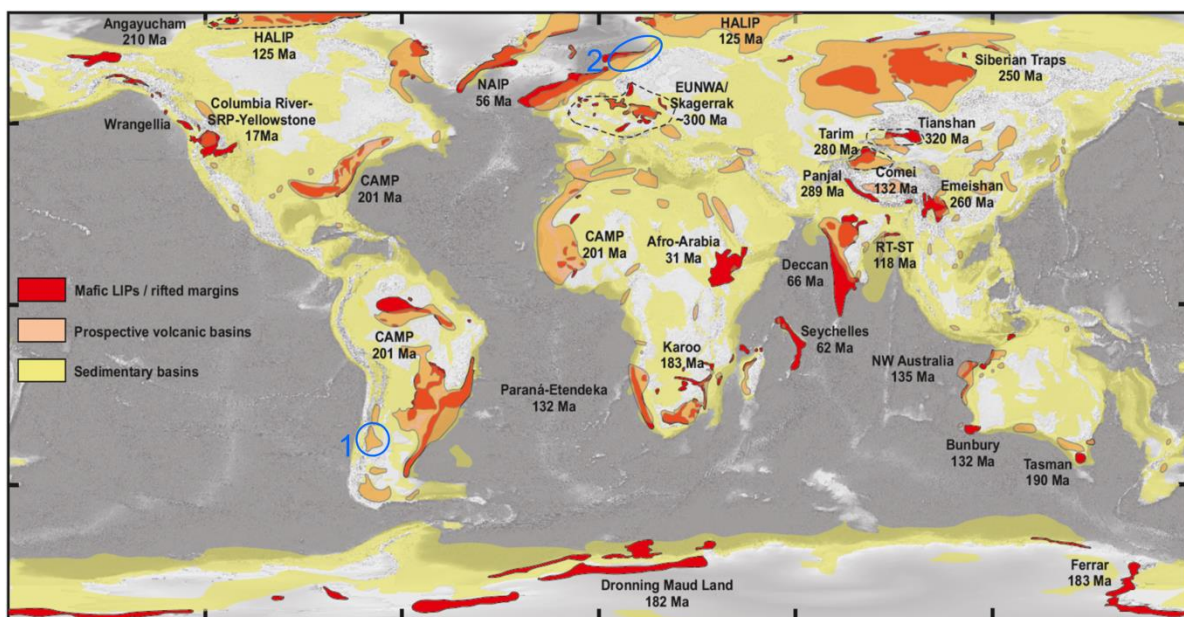

Figure 2.1: World map showing the distribution of sedimentary and important igneous events (after Millett et al., 2016)**.** The blue circles indicate the areas of field work (1 – Neuquén Basin in Argentina) and seismic data (2 – Møre Basin in Norway) underlying this thesis. HALIP – High Arctic Large Igneous Province, SRP – Snake River Plane, CAMP – Central Atlantic Magmatic Province, NAIP – North Atlantic Igneous Province, EUNWA – European Northwest African Large Igneous Province, RT-ST – Rajamahal Traps-Sylhet Traps.

Extreme examples of voluminous magmatic plumbing systems (>1000 km^3) are large igneous provinces (LIPs) and their associated volcanism (Figure 2.1; Bryan et al., 2010; Svensen et al., 2012). These enormous volumes of igneous intrusions have led to a strong enhancement of local metamorphic reactions around the intrusions and extensive release of hydrocarbons and greenhouse gases from organic-rich host rocks into the atmosphere (see Table 2.2 for references). This gas release focuses at pipe-like conduit structures with increased fluid flow originating at or near the intrusion tip as so-called hydrothermal vent complexes, referred to as HTVCs (Table 2.2; Planke et al., 2005). The initiation of HTVCs may already start during or short after (10s of years) the emplacement of the magmatic intrusion, and can last up to 10 kyr after the intrusion emplacement (Iyer et al., 2017; Olive et al., 2018). Today, active HTVCs, which form at the seafloor, are often characterized by black smokers, vents releasing plumes of hot sulphide-rich fluids (e.g., Sánchez-Guillamón et al., 2018). These active hydrothermal systems are investigated as recent examples for ancient HTVCs hosting volcanogenic massive sulphide (VMS) deposits, which are important copper and zinc resources (Galley et al., 2007; Shanks and Thurston, 2012; Berndt et al., 2016). Moreover, the large amounts of released gases throughout these HTVCs, especially associated with LIPs, may have had implications for modern- and paleo-global climate (Svensen et al., 2004; Heimdal et al., 2018; see Table 2.2 for further examples).

Table 2.2: List of studies related to HVTCs and climatic impacts (hydrocarbon/greenhouse gas-release) associated with igneous intrusions.

Hydrocarbon and greenhouse gas-release	References
Hydrothermal vent complexes (HTVCs)	
	Planke et al. (2005)
	Magee et al. (2015)
	Berndt et al. (2016)
	Iyer et al. (2017)
	Villinger et al. (2017)
	Omosanya et al. (2018)
Implications for climatic impacts	
	Svensen et al. (2004)
	Iyer et al. (2013)
	Aarnes et al. (2015)
	Frieling et al. (2016)
	Salmachi et al. (2016)
	Iyer et al. (2017)
	Reynolds et al. (2017)
	Heimdal et al. (2018)
	Planke et al. (2018)
	Svensen et al. (2018a)

2.1 Intrusion geometries

In nature, the diversity of intrusion shapes forming a magmatic plumbing system in the upper brittle crust range from thin sheet intrusions (e.g., dykes, sills, cone sheets) to thick massive intrusions (e.g., laccoliths, stocks, plutons; McCaffrey and Petford, 1997; Breitkreuz and Petford, 2004; Jerram and Bryan, 2018). Note here, that massive in this thesis describes an overall voluminous intrusion geometry, without distinguishing the presence or absence of an internal structure. Each shape of these igneous intrusions reflects a different emplacement mechanism due to the effect of contrasting magma and host rock rheologies (see Chapter 2.2; Galland et al., 2018a). The study presented here focuses specifically on (sub-)horizontally emplaced tabular intrusions in the shallow Earth's crust (Figure 2.2), such as (1) flat or saucer-shaped sills, (2) cone sheets, (3) domed and punched laccoliths. These intrusion shapes are differentiated by their thickness-to-length aspect ratios based on field observations and seismic data, where small thickness-to-length aspect ratios represent the thin sheet intrusions and larger aspect ratios the thick massive intrusions, respectively. Common thickness-to-length values in nature range from 0.0001 to 0.05 for large, usually mafic, sills (Hansen and Cartwright, 2006; Bunger and Cruden, 2011; Cruden et al., 2018) and 0.02 to 1 for laccoliths and thick sills (McCaffrey and Petford, 1997; de Saint-Blanquat et al., 2006; Bunger and Cruden, 2011; Delpino et al., 2014; Schmiedel et al., 2015; Cruden et al., 2018).

Sills were originally defined as layer-concordant tabular sheet intrusions based on their most common occurrence in the field (Table 2.3; Gilbert, 1877; Tweto, 1951; Corry, 1988). In addition, the increasing amount of seismic studies providing large scale data (km-scale) of igneous sill complexes (Table 2.4) shows that locally discordant behaviour is a common observation for sills (Figure 2.2a; Planke et al., 2005). These locally discordant or transgressive parts of the sill complexes, i.e., inclined sheets, can result in an overall saucer-like intrusion shape when they originate from the edges of the initial flat central sill, hence the name saucer-shaped sills (Figure 2.2b; Chevallier and Woodford, 1999).

Cone sheets were originally defined as conical and inward dipping inclined sheets, fed from an overpressurized central magma chamber (Anderson, 1936; Anderson, 1937; Phillips, 1974). However, Galland et al. (2014) highlighted the very close resemblance between sub-circular inward dipping sheets fed either from a magma reservoir (cone sheets) or by a tabular sheet (saucer-shaped sill) observed in the field and seismic data (Table 2.3 and 2.4). Therefore, a confident field-based differentiation between a saucer-shaped sill and a cone sheet can be challenging due to the usually limited exposure of the central magma source (Figure 2.2b).
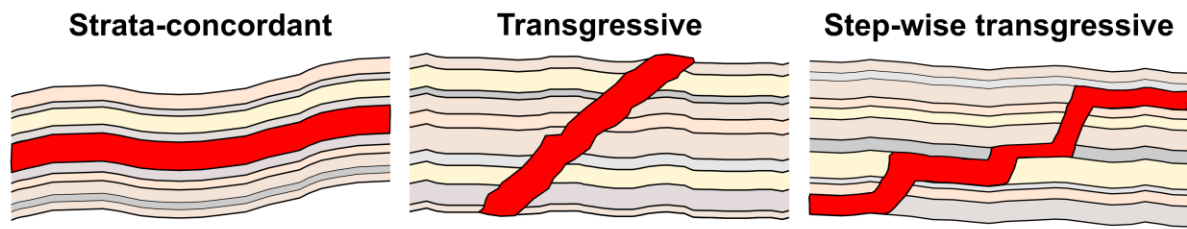
Laccoliths were originally defined as concordant, flat-floored, tabular intrusions with overarched host rock strata (Gilbert, 1877; Daly, 1905). Presently, field observations do not provide consensus on their formation history. One mode of formation is the successive emplacement of a stack of several sheets (Morgan et al., 2008; Horsman et al., 2009), whereas another would be that of one initial, inflating sheet (Johnson and Pollard, 1973; Lorenz and Haneke, 2004; Mattsson et al., 2018; see Table 2.3 for examples). The obvious

similarity between sills and laccoliths (Figure 2.2b; Table 2.3) led to several attempts using their aspect ratio (thickness/diameter) to distinguish them (e.g., Cruden et al., 2018 and references therein), however, none with a general success. Thus, one should be aware that the same igneous intrusion may be addressed as both a sill and/or a laccolith (Galland et al., 2018).

For the sake of completeness, it should be mentioned that these intrusion shapes are common, not only for magmas, but also in sedimentary successions with sandstone intrusions (see Table 2.5 for references). There, conical sheet intrusions are often referred to as V-shaped intrusions, due to their most common appearance in seismic data (Table 2.5). This implies that some of the conclusions on the physical mechanisms for the emplacement of igneous intrusions from this work might be applicable to sedimentary intrusions as well (Haug et al., 2018).

To summarize, (saucer-shaped) sills, cone sheets, and laccoliths may all be described as initially (sub-)horizontal intrusions of variable thickness and length, dominantly concordant, and with possible transgressive parts, e.g. inclined sheets. Each of these intrusion shapes has a distinct geometry based on small-scale field observations and on the interpretation of large-scale seismic data (Table 2.3 and 2.4). However, both field and seismic data come with significant limitations: (1) outcrop size observations are rarely enough to fully describe the complex 3D structures as well as their spatial extent, (2) the thickness in seismic data is often not constrained (travel time acquisition, only top reflection, etc.). Presently, the diversity of natural intrusion shapes is addressed by different models for magma emplacement, one for each intrusion type, rather than one generalized mechanical model for all (see Chapter 2.3).

a) Elements of a sill complex

Strata-concordant **Transgressive** **Step-wise transgressive**

b) Intrusion shapes and host rock deformation

Sheet intrusions **Massive intrusions**

Elastic bending Elastic bending

Sill Laccolith

Elastic bending + shear failure Shear failure

Saucer-shaped sill Punched laccolith
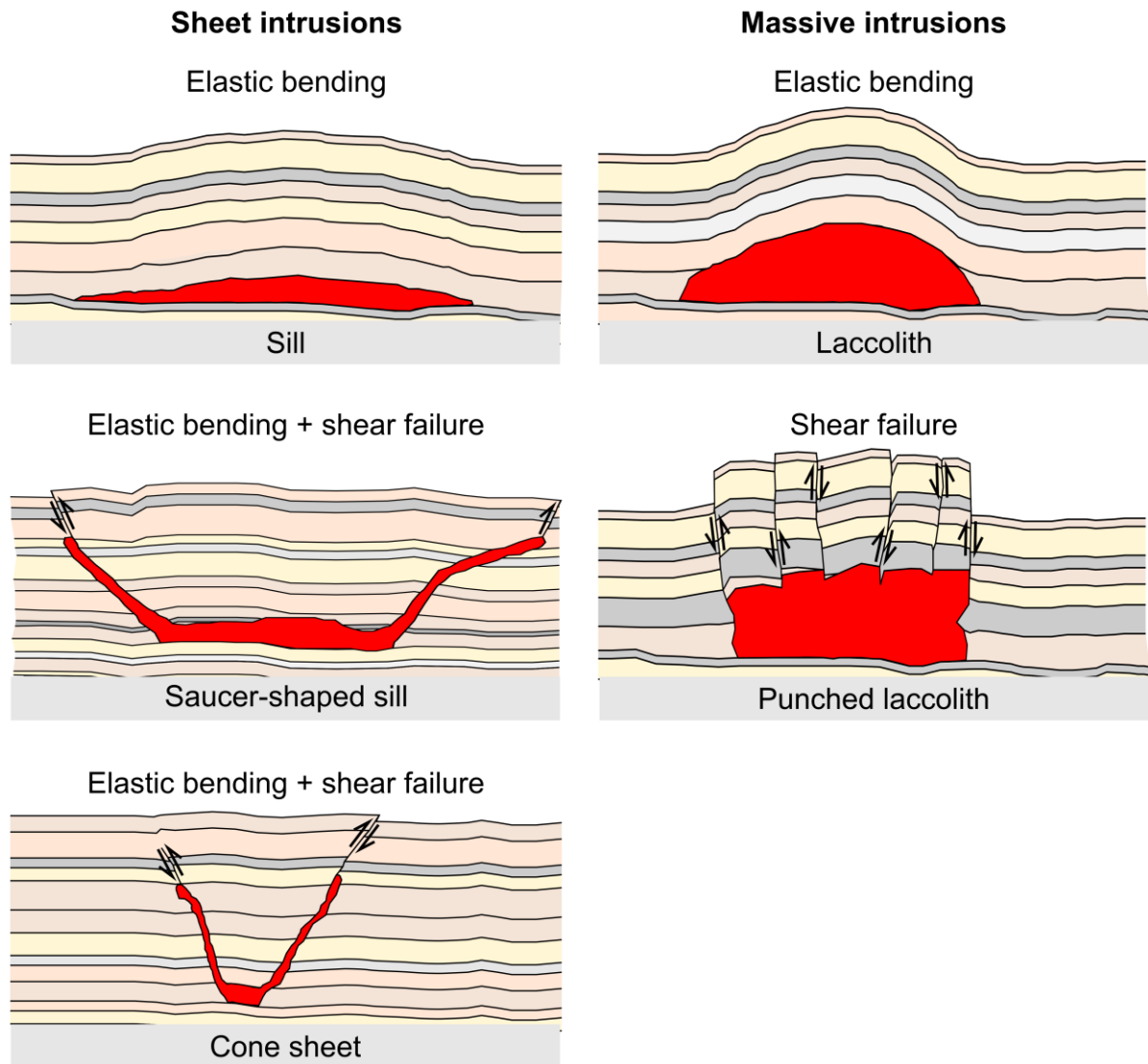
Elastic bending + shear failure

Cone sheet

Figure 2.2: Schematic drawings of magma emplacement (Graphics modified after Galland et al., 2018)**. (a)** Shows possible relations of (sub-)horizontal intrusions and the host strata they are emplaced in. **(b)** Shows shapes of the most common, tabular intrusions.

Table 2.3: List of selected field studies for intrusion shapes.

Location	Reference
Sills	
Ferrar Large Igneous Province (LIP), Transantarctic Mountains (Antarctica)	Muirhead et al. (2014) Airoldi et al. (2016)
Ferrar LIP, Theron Mountains (Antarctica)	Hutton (2009)
Golden Valley Sill Complex, Karoo Basin (South Africa)	Galerne et al. (2008) Polteau et al. (2008a) Schofield et al. (2010) Galerne et al. (2011) Senger et al. (2015)
Loch Scridain Sill Complex, Ilse of Mull (Scotland)	Stephens et al. (2017)
Midland Valley Sill, Midland Valley (Scotland)	Francis (1982)
Neill Klinter Sea Cliff Sill Complex, Jameson Land Basin (Greenland)	Eide et al. (2016) Eide et al. (2017)
Cuesta del Chihuido Sill Complex, Neuquén Basin, (Argentina)	Spacapan et al. (2017)
Secunda Complex, Karoo Basin, (South Africa)	Coetzee and Kisters (2017)
Sill Complex, Werra-Fulda Basin (Germany)	Schofield et al. (2010)
Sill Complexes, Gore Range (USA)	Tweto (1951)
Various sills (Iceland)	Gudmundsson and Løtveit (2014) Gudmundsson et al. (2014)
Various Sills (Worldwide)	McCaffrey and Petford (1997) Cruden et al. (2018)
Cone sheets	
Ardnamurchan Central Igneous Complex, Scottish highlands (Scotland)	Kuenen (1937) Burchardt et al. (2013)
Carlingford Complex, Carlingford Peninsular (Ireland)	Le Bas (1971)
Various cone sheets (Iceland)	Gudmundsson and Løtveit (2014) Gudmundsson et al. (2014)
Laccoliths	
Badrinath-Gangotori Laccolith, Garhwal Himalaya (India)	Scaillet et al. (1995)
Black Mesa, Henry Mountains (USA)	Habert and de Saint-Blanquat (2004) de Saint-Blanquat et al. (2006)
Cordón Caulle, Andean Volcanic Belt (Chile)	Castro et al. (2016)
Elba Laccolithic Complex, Elba Island (Italy)	Dini et al. (2002) Rocchi et al. (2010) Roni et al. (2014)
Halle Volcanic Complex (Germany)	Breitkreuz et al. (2009) Schmiedel et al. (2015) Słodczyk et al. (2015) Breitkreuz et al. (2018)
Henry Mountains (USA)	Gilbert (1877) Hunt et al. (1953) Johnson and Pollard (1973) Corry (1988) de Saint-Blanquat et al. (2006) Morgan et al. (2008) Horsman et al. (2009) Wilson et al. (2016)
Holmes (bysmalith) laccolith, Gallatin Mountains (USA)	Iddings (1898)

Table 2.3 continued.

Location	Reference
Larragan laccolith, Basque-Cantabrian Basin, (Spain)	Agirrezabala (2015)
Sandfell Laccolith, Fáskrúðsfjörður (Iceland)	Mattsson et al. (2018)
Various laccoliths (Iceland)	Gudmundsson and Løtveit (2014)
	Gudmundsson et al. (2014)
Various laccoliths (Worldwide)	Corry (1988)
	McCaffrey and Petford (1997)
	Cruden et al. (2018)

Table 2.4: List of selected seismic studies for intrusion shapes.

Location	Reference
Sills	
Barents Sea, North Atlantic Ocean (Norway – Russia)	Polteau et al. (2016)
Ceduna Sub-Basin, Great Australian Bright Basin, South Indian Ocean (Australia)	Jackson et al. (2013)
	Reynolds et al. (2018)
Danmarkshavn Basin/Thetis Basin, North Atlantic, (Greenland)	Reynolds et al. (2017)
Exmouth Sub-Basin, Northern Carnarvon Basin, Indian Ocean (Australia)	Symonds et al. (1998)
	Magee et al. (2013)
	Magee et al. (2015)
	Magee et al. (2017b)
Faroe-Shetland Basin Sill Complex, North Atlantic Ocean (Faroe Islands – United Kingdom)	Bell and Butcher (2002)
	Smallwood and Maresh (2002)
	Trude et al. (2003)
	Hansen et al. (2004)
	Mark et al. (2017)
	Schofield et al. (2017)
Guaymas Basin, Gulf of California, Pacific Ocean (USA)	Berndt et al. (2016)
Jiaojiang Sag, East China Sea, West Pacific Ocean (China)	Rui et al. (2013)
Møre Basin, Norwegian Sea, North Atlantic Ocean (Norway)	Planke et al. (2005)
	Polteau et al. (2008b)
	Kjoberg et al. (2017)
	Schmiedel et al. (2017b)
Pearl River Mouth Basin, South China Sea, West Pacific Ocean, (China)	Sun et al. (2014)
	Zhao et al. (2014)
Rockall Basin, North Atlantic Ocean (Ireland – United Kingdom)	Smallwood and Maresh (2002)
	Hansen and Cartwright (2006)
	Magee et al. (2014)
Vøring Basin, Norwegian Sea, North Atlantic Ocean (Norway)	Berndt et al. (2000)
	Planke et al. (2005)
	Cartwright and Hansen (2006)
	Omosanya et al. (2017)
	Planke et al. (2018)
Various Sills (Worldwide)	Magee et al. (2016)
Laccoliths	
Ceduna Sub-Basin, Great Australian Bright Basin, South Indian Ocean (Australia)	Jackson et al. (2013)
	Magee et al. (2016)

Table 2.5: List of selected studies on sand intrusions – (saucer-shaped) sills, cone sheets, V-shapes.

Location	Reference
Field studies	
Pancho Giant Injection Complex, California (USA)	Vétel and Cartwright (2010) Hurst and Vigorito (2017)
Seismic studies	
Faroe-Shetland Basin, North Atlantic Ocean (Faroe Islands – United Kingdom)	Shoulders et al. (2007) Cartwright et al. (2008)
Viking Graben/Norwegian North Sea, North Atlantic Ocean (Norway – United Kingdom	Huuse et al. (2004)

2.2 Mechanisms of host rock deformation

As described in Chapter 2.1, the emplacement of magma in the shallow Earth's crust results in various intrusion shapes depending on the magma-host rock interactions. These interactions can take place during or after the emplacement of the intrusion (Section 2.2.1 and 2.2.2). The impact on the host rock due to an igneous intrusion is then often embodied as a large scale dome above the intrusion (Figure 2.3; du Toit, 1920; Jackson and Pollard, 1990; Trude et al., 2003; Magee et al., 2017a) and/or with hydrothermal vent complexes (HTVCs) along the intrusion periphery (Figure 2.4; Table 2.2). These dome structures can serve as structural traps, i.e., four-way dip closures, for hydrocarbons (e.g., Magee et al., 2017b; Omosanya et al., 2017). Moreover, the domes can create or deform stratigraphic traps and thus influence the distribution of reservoir rocks for hydrocarbons, including the onlap of reservoir rocks and the deflection of paleo-channels and rivers (Schutter, 2003b; Delpino et al., 2014). Note that, the HTVCs are often linked to climatic changes due to their potential function as conduits for released hydrocarbons and greenhouse gases into the atmosphere (Svensen et al., 2004; Heimdal et al., 2018; for more references see Table 2.2).
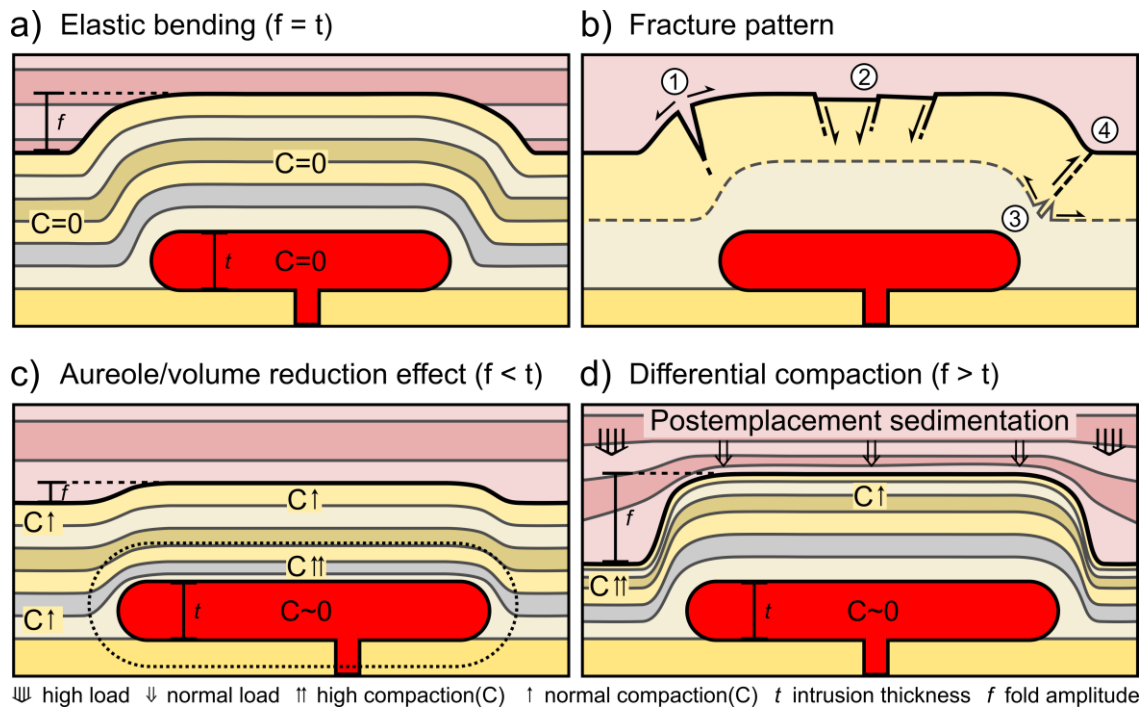
a) Elastic bending (f = t)

b) Fracture pattern

c) Aureole/volume reduction effect (f < t)

d) Differential compaction (f > t)

Postemplacement sedimentation

⇊⇊ high load ⇩ normal load ⇑⇑ high compaction(C) ↑ normal compaction(C) *t* intrusion thickness *f* fold amplitude

Figure 2.3: Schematic diagrams showing mechanisms of overburden deformation associated with the emplacement of a tabular intrusion. (a) Purely elastic host rock: formation of the dome structure above the intrusion as a forced fold (synemplacement). **(b)** Four fracture types related to elastic and inelastic overburden deformation: (1) circumferential, tensile fractures (mode I) in the area of the larges convex curvature of the dome, (2) radial, tensile fractures (mode I) and/or normal faults (mode II) caused by outer-arc stretching, (3) dilatational fractures (mode I) progressing towards the surface, (4) shear fractures (mode II) resulting from differential uplift. **(c)** Inelastic deformation (volume reduction): porosity decrease within the metamorphic aureole around the intrusion. **(d)** Differential compaction: development and/or enhancement of a dome structure above the intrusion under the load of postemplacement sedimentation. (Graphic modified after Schmiedel et al., 2017).

2.2.1 Synemplacement mechanisms

In the last decades, several distinct mechanisms controlling the formation of intrusion-associated dome structures have been proposed. The most common mechanism, often referred to as forced folding (du Toit, 1920; Stearns, 1978; Trude et al., 2003), considers the uplift and doming as directly controlled by the accommodation of the underlying intrusion (e.g., Pollard and Johnson, 1973; Roman-Berdiel et al., 1995; Galland et al., 2018a and references therein). Forced folds above igneous intrusions in seismic data typically occur as overall upward convex features with onlapping reflections; they represent a positive topographic (or bathymetric) structure at the contemporaneous surface and the onlap of sediments deposited during/after the intrusion emplacement onto it (Trude et al., 2003; Magee et al., 2017b; Schofield et al., 2017). The majority of studies on forced folds assume that the synemplacement uplift above the intrusion occurs due to elastic bending (Figure 2.3a) and sometimes failure of the overburden (see Chapter 1.3) induced by the emplacing magma. Note that the synemplacement mechanism of stoping, i.e., blocks of broken-up overburden fall into the upward moving magma body, is not considered in this thesis due to its small volumetric significance (Glazner and Bartley, 2006).

14

The elastic deformation, i.e. elastic bending in the overburden, creates complex stress distributions in the host rock, resulting in outer-arc stretching and inner-arc compression (Timoshenko and Woinowsky-Krieger, 1959; Ramsay, 1967; Pollard and Johnson, 1973). According to Ramsay (1967) outer-arc stretching may lead to a thinning of the uppermost layers of the dome structure. In case the strength of the host rock is exceeded by the stresses produced in response to the elastic deformation, host rock failure occurs around the intrusion tip and above the intrusion. This leads to the development of characteristic fracture networks with tensile and/or shear fractures, observed in field and seismic data (Figure 2.3b; e.g., Senger et al., 2015; Wilson et al., 2016; Magee et al., 2017b). The occurrence of HTVCs typically match the occurrence of these fracture networks, suggesting that the enhanced fluid flow needed for HTVCs is often localized in these fractures (Figure 2.4; Agirrezabala, 2015; Magee et al., 2015). Note here, that heating of the host rock due to the intrusion and the associated fluid migration (potentially leading to HTVCs) may take far longer than the actual emplacement of the igneous intrusion (Figure 2.4; e.g., Iyer et al., 2017; Spacapan et al., 2018).
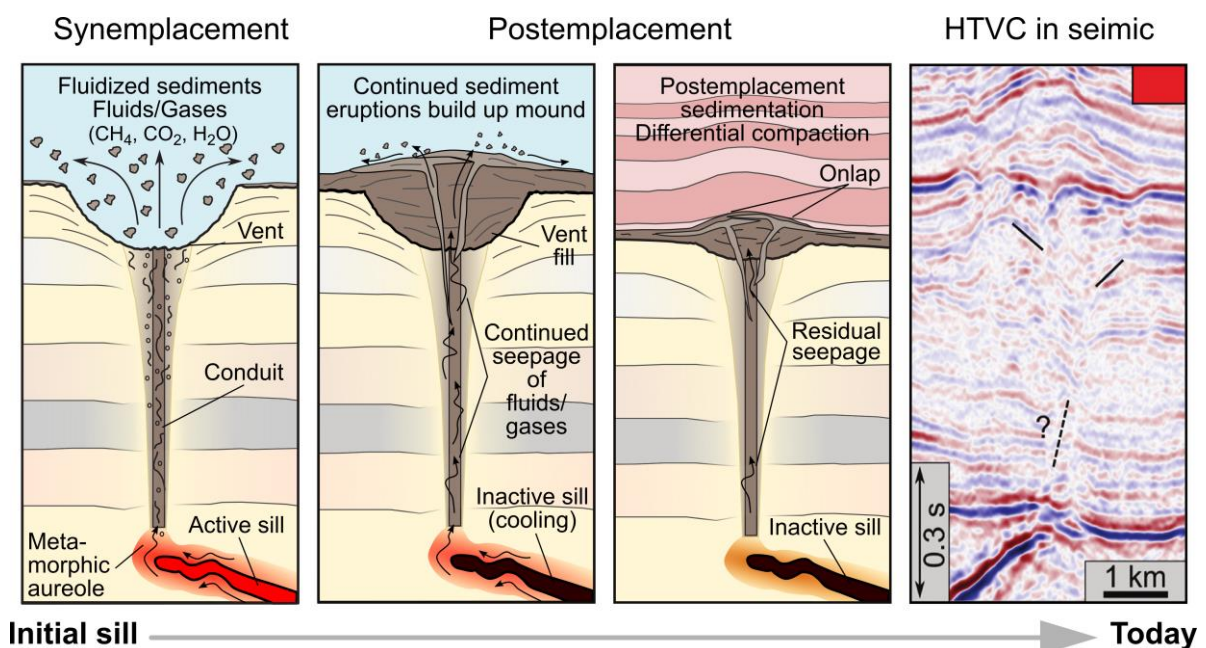

Figure 2.4: Schematics showing the evolution of a hydrothermal vent complex (HTVC) and its appearance in seismic data. Black lines in the last frame illustrate the dip of reflections displayed in the image towards the assumed conduit center. The dashed line highlights the increased uncertainty towards steeper dipping reflections in the lower part of the conduit. (Graphic modified after Kjoberg et al., 2017).

Even so elastic bending promotes uplift of the overburden; other mechanisms may affect the evolution and geometry of the dome as well (Figure 2.3c and 2.3d), i.e., (1) locally enhanced compaction (e.g., Cosgrove and Hillier, 1999; Hansen and Cartwright, 2006), or (2) fluidization of the host rock (e.g., Schofield et al., 2012; Schofield et al., 2014). The expulsion of pore fluids close to the intrusion may lead to a decreased porosity within

the thermal and/or structural aureole, resulting in a substantial reduction of the host rock volume (Einsele et al., 1980; Hansen and Cartwright, 2006; Jackson et al., 2013). This may ultimately reduce the amplitude of the active mechanical doming induced by the emplacement of the underlying intrusion (e.g., Magee et al., 2013; Magee et al., 2017b).

Some of these mechanisms (i.e., fluidisation, enhanced fluid flow, etc.) may be initiated by the thermo-mechanical effect of the emplacing intrusion. However, due to their temperature-driven nature these effects can be active much longer than only the time of magma emplacement (Figure 2.4; Table 2.2). Note that the analyses of the thermal effects of magma emplacement on the host rock are outside the scope of this study. These effects have been documented and modelled for sill intrusions in sedimentary basins (e.g., Spacapan et al., 2018; Iyer et al., 2017; Table 2.2), as well as for large, deep plutonic complexes (e.g., Karlstrom et al., 2017)

2.2.2   Postemplacement mechanism

Another mechanism to produce dome structures (folds) above igneous intrusions is differential compaction (Figure 2.3; Cosgrove and Hillier, 1999; Jackson et al., 2013; Magee et al., 2017b). Differential compaction involves the variable subsidence of the overburden due to the load of the postemplacement sedimentation (Cosgrove and Hillier, 1999). This variable subsidence originates from the virtual incompressibility of an igneous intrusion with respect to the surrounding sedimentary host rock, therefore a dome structure may develop post-intrusion (e.g., Cosgrove and Hillier, 1999; Hansen and Cartwright, 2006; Magee et al., 2017b). In addition to the generation of a new dome, differential compaction may enhance the amplitude of a preexisting dome structure (forced fold) above an intrusion.
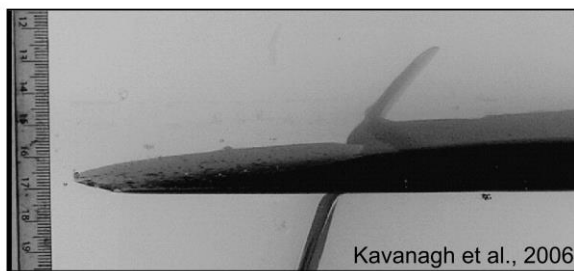
2.3 Models of magma emplacement

The individual mechanisms causing the intrusion-induced deformation and failure of the surrounding host rock are difficult to assess in nature (Galland et al., 2018a) since active magmatic systems are inaccessible due to extreme conditions (i.e., temperature, pressure, depth, etc.). Moreover, ancient magmatic systems are a combination of past and current geological processes (i.e., emplacement, tectonic, weathering). Therefore, to explain the impact on the host rock specifically due to the emplacement of igneous intrusions, a range of different model approaches have been proposed, all aimed at explaining field observations and seismic data. These include laboratory/analogue, numerical, and theoretical modelling (see Section 2.3.1-2.3.3). Traditionally, two end-member type models of magma emplacement exist: (1) models for sheet intrusions, considering a purely elastic host rock with low (often neglected) viscosity (Section 2.3.1), or (2) models for massive intrusions, usually consisting of a plastic model host rock intruded by highly viscous model
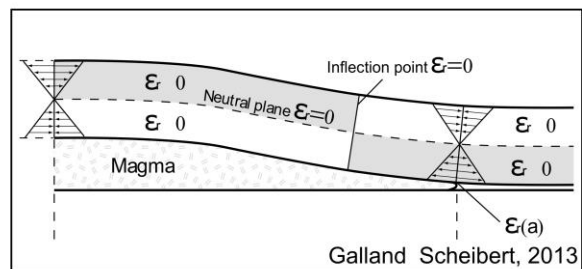
magma (Section 2.3.2). Thus, both end-member type models assume it is the significant contrast in magma and host rock rheology that controls the emplacement of igneous intrusions. In particular, these models for magma emplacement try to understand the mechanisms of overburden deformation (i.e., elastic bending, shear failure, etc.), leading to dome-shaped structures and associated fracture patterns in the host rock.
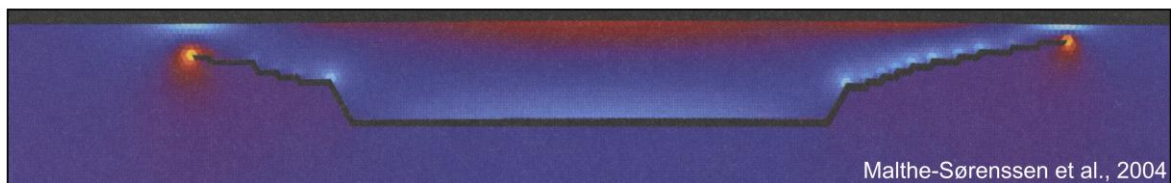
2.3.1 Elastic models

Figure 2.5: Elastic models. (a) Laboratory model: injecting dyed water in gelatin. **(b)** Analytical model: intrusions emplacement between a rigid plate and a thin elastic plate. **(c)** Numerical model: intrusion emplacement simulated with discrete element model (DEM).
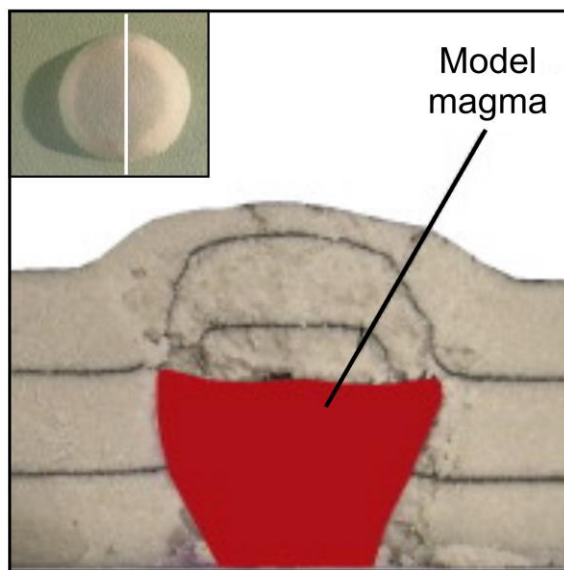
The first attempts to explain the accommodation of magma due to bending and failure of overburden layers above horizontal intrusions started with Gilbert (1877) and his "Report on the geology of the Henry Mountains". Since then classic models of magma-induced deformation involve doming, i.e., the overburden uplift in response to elastic bending above an intruding sill or laccolith (Table 2.6; Pollard and Johnson, 1973). Note that the magma viscosity in many of these elastic models is considered to be negligible or low-viscous effectively simulating the strong natural contrast between magma and host rock viscosity. In general, theoretical and numerical elastic models use the mathematical formulation of a bending plate (Figure 2.5; Timoshenko and Woinowsky-Krieger, 1959; Ventsel and Krauthammer, 2001) for the overburden behaviour caused by the emplacement of a tabular intrusion (Table 2.6). To be able to apply the thin plate theory these models have to consider the following assumptions: (1) the radius of the intrusion should be at least 5 times larger than the thickness of the overburden (Timoshenko and Woinowsky-Krieger, 1959) or 2-3 times larger in case of an overburden comprised of a number of thin layers (Pollard and Johnson, 1973), (2) the intrusion radius should be 50 times larger than the thickness of the intrusion (Ventsel and Krauthammer, 2001), and (3) the vertical deformation of the

overburden induced by the intrusion is small and caused solely by elastic bending of the overburden (Kerr and Pollard, 1998; Turcotte and Schubert, 2014). In nature these assumptions are valid for thin tabular intrusions such as sills; nevertheless they fail to describe the occurrence of massive, high aspect ratio, intrusions, e.g., laccoliths.

Although most of the theoretical and numerical elastic models for magma emplacement provide a quasi-static solution, the emplacement of magma is a dynamic process. Therefore, dynamic analogue/laboratory models are commonly used to simulate the propagation of magma forming intrusions in the Earth's crust (Galland et al., 2018a; Kavanagh et al., 2018 and references therein). These elastic laboratory models do not require the same geometric assumptions as the theoretical and numerical elastic models. However, also these rely on a linearly elastically deforming host, e.g. gelatine (Figure 2.5; Table 2.6).
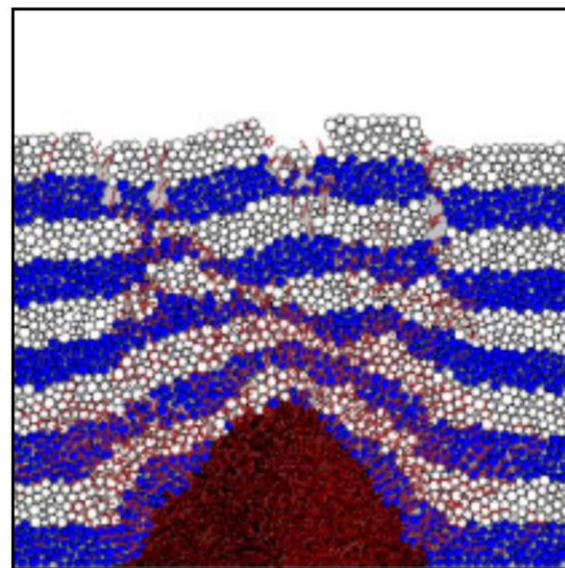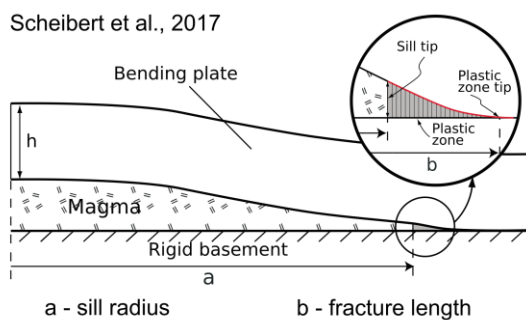
2.3.2 Inelastic models

Figure 2.6: Inelastic (plastic) models. (a) Analogue models: injecting high-viscous silicone into a box of sand. Small inlay shows the top view on the model surface and the white line indicated the location of the cross-section. **(b)** Numerical model approach: discrete element model (DEM) simulates a plastic host rock of various strengths. Red markers indicate (shear) failure in the model rock.

The large deformation (large strain) associated with the emplacement of thick, massive intrusions would lead to unrealistically high stresses in a purely elastic host rock (Brothelande et al., 2016). Thus, large deformation observed around natural intrusions in nature occurs mostly as plastic deformation (i.e. compaction etc.) and/or overburden failure (i.e. fractures, shear failure; e.g., MacCarthy, 1925; Delpino et al., 2014; Wilson et al.,

2016). In addition, a strong rheology contrast between magma and host rock controlling the emplacement of these massive intrusions of generally highly viscous magma (e.g., Galland et al., 2014) requires the host rock to be weak. Traditionally, the generation of space for the emplacing magma into a weak host rock with very low cohesion (to no cohesion) is based on plasticity, specifically on plastic behaviour and/or shear failure of the overburden (Davis and Selvadurai, 2005). To account for this particular host rock behaviour, various granular materials were tested (Klinkmüller et al., 2016; Ritter et al., 2016; Montanari et al., 2017a) for their use in laboratory models (Table 2.6). Moreover, particle-based numerical models are used to simulate inelastic host rock behaviour induced by an intrusion (Figure 2.6; Table 2.6). Although these inelastic models manage to simulate the emplacement of thick massive intrusions (high viscosity) equivalent to natural (punched) laccoliths (Table 2.6), they fail to simulate thin sheet intrusions (low viscosity) due to the occurrence of uncontrolled porous flow into the granular model rocks.
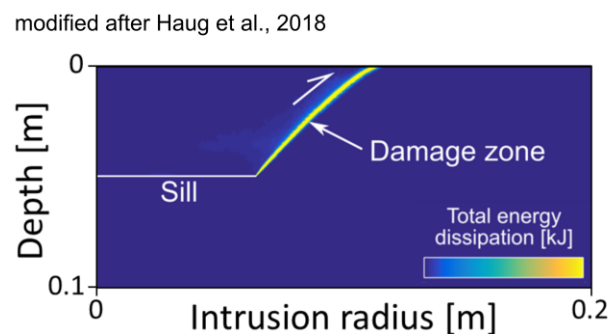
2.3.3   Elasto-plastic models

Figure 2.7: Elasto-plastic models. (a) Schematics for the analytical model for sill and laccolith emplacement in a dominantly elastic host rock. However, Scheibert et al. (2017) suggested the occurrence of inelastic (plastic) deformation at the intrusion tip. **(b)** Graphical result of the limit analysis approach after Haug et al. (2017) and Haug et al. (2018). The energy dissipation indicates the area (damage zone) most prone for the occurrence of shear failure.

The limitations of the end-member type models for magma emplacement into Earth's brittle upper crust are: (1) simplistic host rock behaviour, (2) the inability to reproduce the natural diversity of intrusion shapes, (3) the lack of shear failure associated with thin sheet intrusions. To overcome these limitations, recent model approaches use a more realistic elasto-plastic model rock with a Mohr-Coulomb failure criterion, similar to crustal rocks (Table 2.6). These current laboratory, numerical, and theoretical models (Table 2.6) show that the inelastic brittle behaviour of the Earth's crust may play a major role on the emplacement, growth and shape of tabular intrusions, both sheet and massive intrusions (Figure 2.7). Therefore, most of recent elasto-plastic models for magma emplacement simulate the host rock, i.e., the brittle upper crust, as a Mohr-Coulomb material which

accounts both for elastic tensile and plastic shear stresses (e.g., Brothelande et al., 2016; Gerbault et al., 2018; Haug et al., 2018). In addition, during the last years several novel Mohr-Coulomb granular materials were tested for the integration as model rock in analogue/laboratory experiments (e.g., Galland et al., 2006; Mourgues et al., 2012; Bureau et al., 2014; Abdelmalak et al., 2016a). The use of these Mohr-Coulomb granular materials allows the simulation of various intrusion shapes (sheet intrusions) such as (saucer-shaped) sills and cone sheets (Table 2.6). In particular, I should highlight here that the laboratory setup used in the experiments presented in this thesis was developed by Olivier Galland (see Table 2.6 for references). The novelty of this thesis lies in it being the first systematic test on the effect of host rock strength for the emplacement of horizontally emplaced (tabular) intrusions, using different Mohr-Coulomb granular materials. Finally, the numerical simulations of Haug et al. (2018), using a Mohr-Coulomb host rock, showed that shear failure needs to be taken into account for the emplacement of thin sheet intrusions (Figure 2.7).

Table 2.6: Selected list of magma emplacement models in the shallow Earth's crust.

Model type	Intrusion shape(s)	Reference
Elastic models		
Theoretical/numerical	Sill/laccolith	Pollard and Johnson (1973)
	Sill/(laccolith)	Goulty and Schofield (2008)
	(Sill)/laccolith	Michaut (2011)
	Sill/laccolith	Galland and Scheibert (2013)
	(Sill)/laccolith	Thorey and Michaut (2016)
	Laccolith	Dixon and Simpson (1987)
	Various	Bunger and Cruden (2011)
	Various	Cruden et al. (2018)
	Various	Kavanagh et al. (2018) and references therein
Laboratory	Sill	Pollard (1973)
	Sill	Kavanagh et al. (2006)
	Sill	Kavanagh et al. (2015)
	Sill	Kavanagh et al. (2017)
	Laccolith	Hyndman and Alt (1987)
	Laccolith	Corry (1988)
	Laccolith	Currier and Marsh (2015)
	Laccolith	Currier et al. (2017)
	Various	Kavanagh et al. (2018) and references therein
Inelastic models		
Theoretical/numerical	Laccolith	Zhao et al. (2008)
Laboratory	(Sill)/laccolith	Montanari et al. (2017b)
	Laccolith	Ramberg (1981)
	Laccolith	Montanari et al. (2010)
	Various	Galland et al. (2018a) and references therein

Table 2.6 (continued).

Model type	Intrusion shape(s)	Reference
Elasto-plastic models		
Theoretical/numerical	Sill/laccolith	Brothelande et al. (2016)
	Sill/laccolith	Scheibert et al. (2017)
	(Saucer-shaped) sill/cone sheet	Haug et al. (2017)
	(Saucer-shaped) sill/cone sheet	Haug et al. (2018)
	Various	Gerbault et al. (2012)
	Various	Gerbault et al. (2018)
Laboratory	Sill/laccolith	Brothelande and Merle (2015)
	Sill/laccolith	Brothelande et al. (2016)
	Saucer-shaped sill	Galerne et al. (2011)
	(Saucer-shaped) sill	Galland et al. (2009)
	(Saucer-shaped) sill/cone sheet	Mourgues et al. (2012)
	(Dyke)/cone sheet	Guldstrand et al. (2017)
	(Dyke)/cone sheet	Guldstrand et al. (2018)
	Various	Galland et al. (2003)
	Various	Galland et al. (2006)
	Various	Abdelmalak et al. (2012)
	Various	Galland (2012)
	Various	Galland et al. (2018a) and references therein
	Various	Rincón et al. (2018)

3 Motivation and Research questions

As mentioned in Chapter 2.2, field studies and seismic data interpretation highlight the importance of different magma and host rock rheologies on the magma emplacement and final intrusion geometry (see Table 2.3 and 2.4). However, these methods poorly constrain to which extent the interaction between syn- and postemplacement mechanisms control the final intrusion shape and the associated host rock deformation and failure (dome structure/forced fold, faults and fracture systems, etc.). Various mechanical models (laboratory/numerical/theoretical) for magma emplacement exist to simulate the physical mechanisms behind the emplacement of magma in the Earth's brittle crust (Chapter 2.3). So far, none of these models has been able to simulate the diversity of (sub-) horizontally emplaced tabular intrusion shapes observed in nature. The motivation for this study was derived from this mismatch between geological observations on tabular igneous intrusions and the assumptions of existing models for magma emplacement in the Earth's brittle crust. The two most common assumptions of these are a strong, elastic host rock (Figure 2.5) or a weak host rock without any cohesion (Figure 2.6). These end-member type models are unable to address to which extent elastic and inelastic deformation was the dominant deformation mechanism to accommodate the emplacement of igneous tabular intrusions. In addition, the rare fulfilment of these assumptions in nature questions the applicability of these simple models to simulate sills, cone sheets, and laccoliths. This shows that our knowledge about the mechanics of magma emplacement is still poor (Gudmundsson et al., 2014; Tibaldi, 2015). Thus, to understand the physical mechanisms of magma emplacement into Earth's brittle upper crust it is necessary to account for realistic elasto-plastic host rock behaviour. Therefore, in this study I present: (1) a multidisciplinary approach of quantitative laboratory models with integrated numerical simulations, and (2) the use of high quality 3D seismic data, to address the following research questions:

Question (1): *How does the surface and overburden deformation in the form of forced folds, faults and fractures correlate with the actual geometry of the intrusion?*

Question (2): *How do host rock cohesion and intrusion depth influence the geometry and the damage patterns associated with magmatic intrusions?*

This thesis concerns the link between the intrusion geometry with the associated overburden and surface deformation. To do that, I performed the laboratory experiments, systematically varying either the overburden thickness/emplacement depth or the strength of the overburden. The parameters generally used to represent the strength of the overburden are the cohesion of the overburden and the angle of internal friction. In my laboratory experiments I controlled the cohesion of the host rock, whereas the angle of internal friction was given by the nature of the granular material. Note that an independent

variation of both parameters cohesion and angle of internal friction, such as possible in numerical simulations (e.g., Haug et al. 2017; 2018) cannot be done in laboratory models since they are material properties and thus inherently linked. For further insights on the simultaneous observation of the time-dependent evolution of the intrusion geometry and the deformation of the overburden/surface, the reader is referred to the doctoral thesis of Frank Guldstrand (University of Oslo, 2018), which describes the results of 2D and 3D laboratory experiments.

In order to simulate the complex physical behaviour of magma-host rock systems in nature the laboratory models used in this thesis are based on the following assumptions and simplifications: (1) the intrusion emplacement occurs as one single event, (2) the effect of solidification does not play a role in the time scale of the emplacement, (3) there are no thermal effects on the surrounding host rock. Galland et al. (2014) showed that different injection velocities of the magma analogue would also affect the geometry of the intrusions. However, for the sake of simplicity, the injection speed in our experiments was kept constant. In addition, the viscosity of magmas in natur ranges across several orders of magnitude ($100–10^{18}$ Pa s; Dingwell et al., 1993; Scaillet et al., 1997), from low viscous mafic composition to high viscous felsic magma compositions. The viscosity of the oil ($\eta =$ 0.02 Pa s; Galland et al., 2006) used in my laboratory experiments does therefore only simulate magmas with a generally high viscosity, such as magmas of intermediate to felsic composition.

3.1 Summary of manuscripts: Seismic interpretation

To address the first research question: "*How does the surface and overburden deformation in the form of forced folds, faults and fractures correlate with the actual geometry of the intrusion?*" a 3D seismic case study from the Møre Basin in the mid-Norwegian margin was used.

The two research articles titled "*Mechanisms of overburden deformation associated with the emplacement of the Tulipan sill, mid-Norwegian margin*" (Appendix A.1) and "*3D structure and formation of hydrothermal vent complexes at the Paleocene-Eocene transition, the Møre Basin, mid-Norwegian margin*" (Appendix A.2) are based on a 3D seismic interpretation of an igneous sill complex (Statoil cube ST0105) situated below the Tulipan well for gas exploration (6302/6-1). While the Tulipan exploration well was economically unsuccessful, the produced data provides an exceptional case study for an igneous intrusion and the associated overburden deformation.

The first article (Appendix A.1) presents the structural and mechanical impact of the Tulipan sill on the sedimentary overburden during and after emplacement, by using various methods of 3D seismic interpretation (horizon/isochron maps, opacity rendering, etc.). The 3D seismic interpretation evidences a dome structure above the Tulipan sill (Figure 3.1) without the feature of onlap in the seismic reflection data, a key indicator for an elastically bended forced fold due to magma emplacement. The results show that the oversimplified elastic model of a forced fold is not sufficient to explain the observed dome structure in the 3D seismic data above the Tulipan sill with an estimated emplacement depth of 1.5-2 km (Figure 3.1). Therefore, a different formation history for the dome structure above the Tulipan sill was developed, which takes into account more realistic elasto-plastic behaviour of natural sedimentary overburden. It involves a combination of different syn- and postemplacement mechanisms of overburden deformation: (1) elastic bending, (2) plastic shear failure, and (3) differential compaction, to explain the formation of the dome structure induced by the emplacement of the Tulipan sill.

The second article (Appendix A.2) investigates the time of emplacement of the Tulipan sill and the occurrence of hydrothermal vent complexes (HTVCs). The 3D seismic interpretation suggests that HTVCs are a direct consequence of the sill emplacement, due to the close spatial relation of thirteen HTVCs with the outer edges of the Tulipan sill (Figure 3.1). Laboratory experiments, involving the injection of overpressurized fluid into a granular host, were used to investigate the characteristic shape of the HTVCs and the physical mechanisms leading to their formation. The modelled seismic response of the experiments showed similar seismic reflection patterns as the observed HTVCs in the 3D seismic data above the Tulipan sill (see Figure 2.4). Thus, the formation of HTVCs may be explained by local fluid overpressure and fluid migration caused by sill-induced contact metamorphism of the host sediments. In addition, a biostratigraphic analysis of the well (6302/6-1) and well-tie correlations with the 3D seismic cube (ST0105) allowed dating of the HTVCs, and thus dating the emplacement age of the Tulipan sill within the range of 54.9-55.8 Ma. This novel data of the timed HTVC formation/Tulipan sill emplacement

matches the Paleocene-Eocene Thermal Maximum (PETM), indicating a link between intrusion-induced release of greenhouse gases with implications for global paleoclimatic changes.
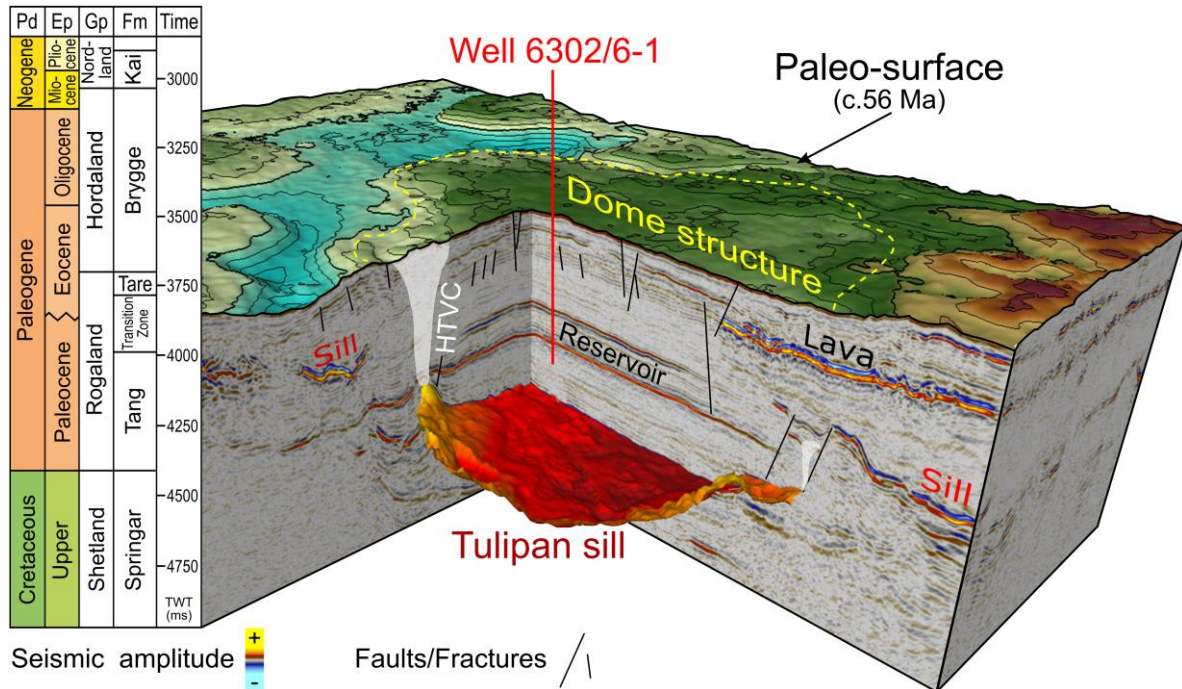

Figure 3.1: 3D seismic visualization of the Tulipan sill and the host sediments at the time of emplacement. (HTVC – Hydrothermal Vent Complex, Pd – Period, Ep – Epoch, Gp – Group, Fm – Formation, TWT – Two Way Travel time in milliseconds).

3.2 Summary of manuscripts: Laboratory modelling

To solve the second research question: *"How do host rock cohesion and intrusion depth influence the geometry and the damage patterns associated with magmatic intrusions?"*, I performed a series of laboratory experiments in the Physics of Volcanic Processes Laboratory (PVP Lab) at the University of Oslo.

Articles three and four are based on laboratory experiments using dry, granular Mohr-Coulomb materials of variable cohesion to model an elasto-plastic host rock into which Végétaline oil as model magma was injected (Figure 3.2; Appendix A.3 and A.4). The homogeneous model host possesses a horizontal flexible net right above the inlet to simulate a pre-existing stratigraphic weakness (e.g. sedimentary layering). The surface of the experiment was monitored during the oil-injection by a photogrammetry system consisting of four digital cameras. After each experiment, the solidified Végétaline oil was carefully excavated to expose the intrusion shape. Then the same photogrammetry system was used to compute the 3D model of the excavated intrusion.
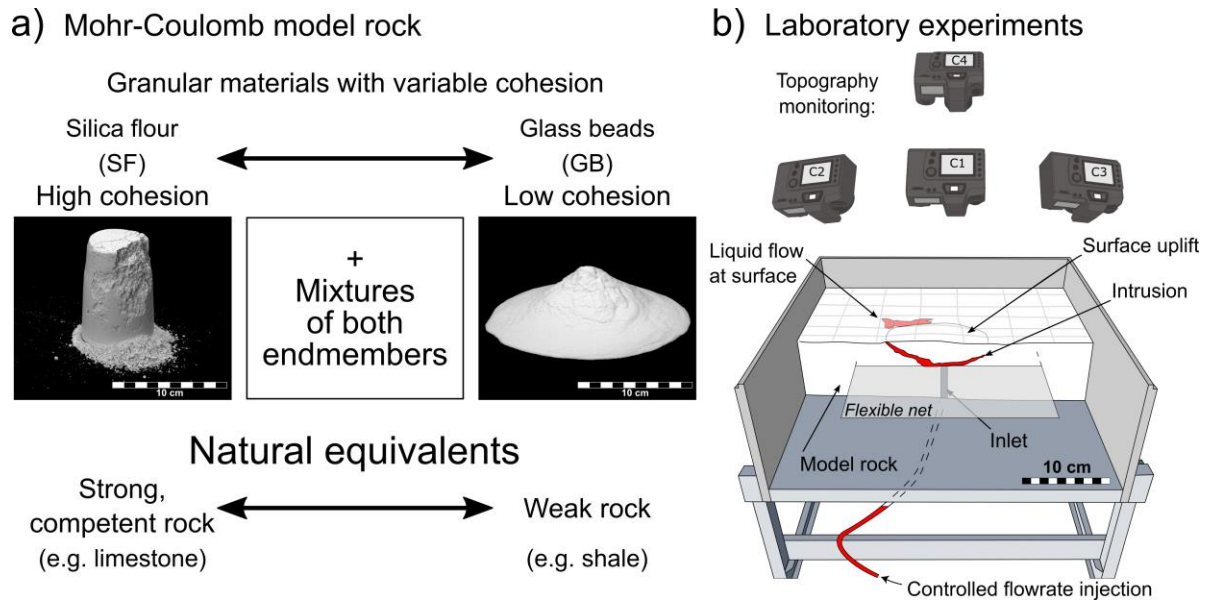
Figure 3.2: Schematics of laboratory materials and experimental setup. (a) Overview of the dry, granular Mohr-Coulomb materials used as model rock in the laboratory experiments and their equivalents in nature. **(b)** Drawing of the experimental setup modified and redrawn after Galland et al. (2009) and Schmiedel et al. (2017a).

The article titled "*Dynamics of Sill and Laccolith Emplacement in the Brittle Crust: Role of Host Rock Strength and Deformation Mode*" (Appendix A.3) investigates the effects of variable elasto-plastic properties of the host rock (Figure 3.2) on intrusion shapes and associated surface deformation. These laboratory experiments are the first to spontaneously produce various intrusion shapes with equivalents in nature. The experimental results show (Figure 3.3): (1) high-cohesion host materials dominantly deform by elastic bending and lead to thin sheet intrusions (e.g. sills); (2) low-cohesion host materials deform by inelastic deformation, i.e., shear failure, and lead to massive intrusions (e.g. punched laccoliths); whereas (3) host materials that deform as a combination of both elastic bending and shear failure are likely to form cone sheets. Thus, the use of models with variable elasto-plastic properties bridges the gap between the existing elastic and plastic end-member type models for magma emplacement, thereby increasing our understanding of the dynamics of magma emplacement in the Earth's brittle upper crust.
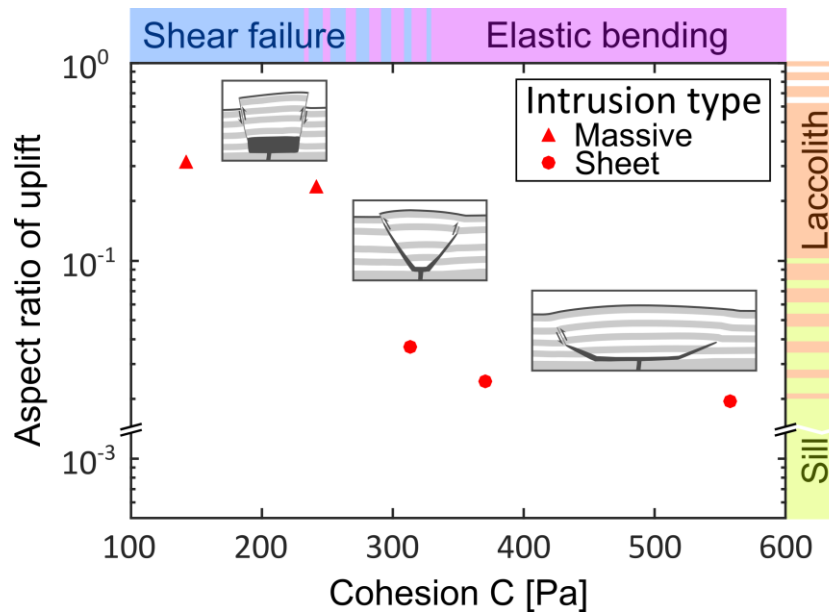
Figure 3.3: Diagram showing the aspect ratio of the surface uplift as a function of the cohesion. The aspect ratio of the surface uplift (dome structure) is calculated as maximum uplift divided by the uplift diameter, and used as a proxy for the aspect ratio of the underlying intrusion. The triangles correspond to massive intrusions, i.e., (punched) laccoliths, whereas the circles correspond to thin sheet intrusions (saucer-shaped sills and cone sheets). The values for the natural ranges of sills and laccoliths on the right side of the plot was estimated from field observations and seismic interpretations (Hansen and Cartwright, 2006; Bunger and Cruden, 2011 and references therein; Schmiedel et al., 2017b)

The last article is a submitted manuscript, which is currently under review (by Earth and Planetary Science Letters) with the title: "*Coulomb failure of Earth's brittle crust controls growth, emplacement and shapes of igneous sills, saucer-shaped sills and laccoliths*" (Appendix A.4). This study integrates additional laboratory experiments (Figure 3.2) with limit analysis numerical models to investigate the role of a host rock's Mohr-Coulomb properties on the emplacement and shape of igneous intrusions. It shows that shear failure along an inward-dipping reverse shear damage zone in the overburden caused by an initial sill is valid for both thin sheet and massive intrusions. This shear failure occurs when the radius of the sill reaches a critical value, which scales linearly with the cohesion of the overburden.

The results show that there are two possible scenarios (Figure 3.4). In the first scenario, inclined sheets are formed due to a cohesive (strong) host rock. The cohesive host rock only allows for tensile opening along a weakened reverse shear zone (inward-dipping), which then accommodates the viscous magma flow forming the inclined sheets. In the second scenario, thick massive intrusions are caused by a sufficiently incohesive (weak) host rock, which allows for the initial sill to inflate and lift up the overburden along a reverse shear zone, similar to scenario one. However, the weak host rock will develop secondary normal faults (outward-dipping), which will then limit the final massive intrusion shape. In addition, we derived a theoretical scaling law for the thickness-to-radius aspect ratios valid for the sheet intrusions of our laboratory experiments. This demonstrates the

physical relevance of the mechanical equilibrium between the viscous magma flow and the Mohr-Coulomb shear failure of the overburden for the emplacement of saucer-shaped intrusions. The presented study conclusively shows that sheet and massive intrusions are both end-members of a mechanical continuum, where the Mohr-Coulomb behaviour (elasto-plastic properties) of the Earth's brittle upper crust plays a crucial role, thus providing a potential solution for a long-standing controversy between current models and geological reality.
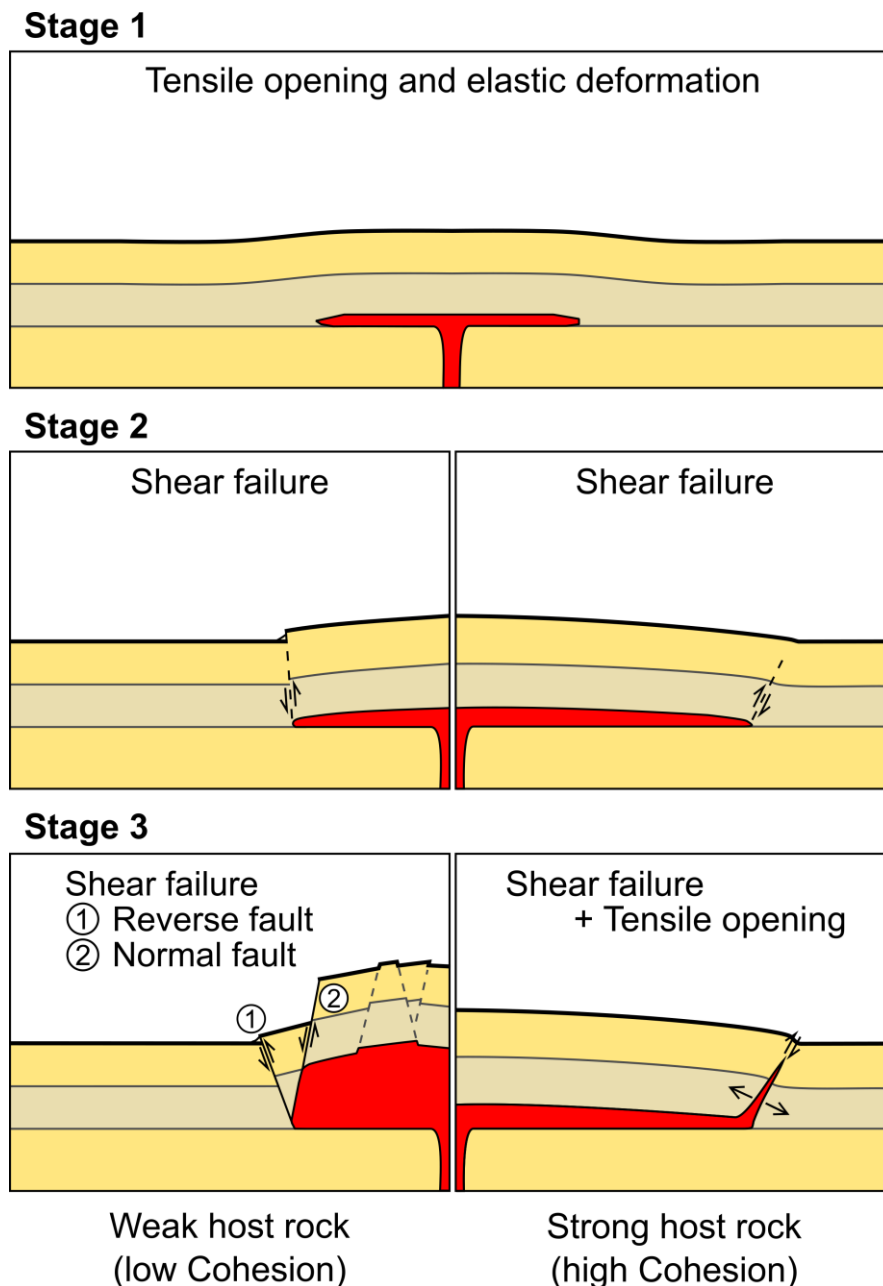

Figure 3.4: Schematic drawing of the three stage evolution for horizontal igneous intrusions controlled by the failure mode of the overburden. Left scenario: two main structures accommodate the intrusion: initial inward-dipping reverse shear fault(s) and final outward-dipping normal fault(s). Right scenario: one main structure accommodates the intrusion: initial inward-dipping reverse shear fault(s), which is opened in a tensile mode.

4 Outlook

The results of this thesis successfully showed: (1) a 3D seismic case study of the saucer-shaped Tulipan sill and an associated dome structure with HTVCs, and (2) the spontaneous formation of different intrusion shapes in laboratory experiments controlled by the host rock strength (cohesion). The success of the laboratory experiments provide a solid foundation for future studies to continue testing the effects of different host rock properties and the implementation of different magma rheology on the intrusion shape.

There are multiple improvements possible for future works. A next step for the laboratory models could be to integrate a model rock with multiple layers, to better understand the effect of sedimentary strata during the evolution of a magmatic intrusion after initial emplacement. Moreover, a wider range of magma viscosities is needed to address the behaviour of the low viscous, mafic magmas in nature. This will need testing of new fluid materials. A better control on the effect of solidification of the injected fluid, e.g. oil (this study) or paraffin wax (Currier and Marsh, 2015), may help to address the aspect of magma cooling. In addition, this would be the first step towards the implementation of pulsed injections, simulating the incremental growth of magmatic intrusions. Finally, the use of different colours for the injected fluid may help to better understand the temporal evolution within the intrusion itself.

In this thesis the pressure evolution in the injected fluid was not recorded, however, the dimensional analysis for our laboratory experiments (Publications III and IV) may be significantly improved by knowing the values of this parameter. Therefore, independent of their model type, future laboratory models should always perform pressure measurements of the injected fluid.

In the long run, these improved laboratory models and their integration with 3D seismic data should make it possible to better constrain the thickness of igneous intrusions in seismic data. A higher precision on the sill thickness-to-dome amplitude aspect ratio is an important parameter to differentiate the contribution of the igneous intrusion from other geological features (tectonics, sedimentary compaction, etc.). To accomplish that, it could prove useful to integrate 3D seismic data with seismic models of field outcrops as recently presented by Eide et al. (2017) and Rabbel et al. (2018).

Beneficial for future studies will also be the improved integration of laboratory experiments and numerical simulations (such as the OptumG2 software used by Haug et al., 2018). Despite the improvements in laboratory experiments to become more quantitative during the last years, there is still a big scale difference between the laboratory and nature. As demonstrated in Paper 4, the laboratory experiments provide excellent benchmarks for the numerical simulations, which then can be used to (1) quantify the elastic versus inelastic deformation of the laboratory models and (2) to simulate directly geological-scale mechanisms. In short, modern day laboratory models in geosciences are a versatile approach to reveal the dynamics of magma emplacement and other physical processes in

nature. However, they benefit and contribute even more when integrated in a multidisciplinary approach with field and seismic data, and numerical simulations.

Bibliography

Aarnes, I., Planke, S., Trulsvik, M., Svensen, H., 2015. Contact metamorphism and thermogenic gas generation in the Vøring and Møre basins, offshore Norway, during the Paleocene–Eocene thermal maximum. Journal of the Geological Society South Africa 172, 588-598. doi: 10.1144/jgs2014-098

Abdelmalak, M.M., Mourgues, R., Galland, O., Bureau, D., 2012. Fracture mode analysis and related surface deformation during dyke intrusion: Results from 2D experimental modelling. Earth and Planetary Science Letters 359–360, 93-105. doi: 10.1016/j.epsl.2012.10.008

Abdelmalak, M.M., Andersen, T.B., Planke, S., Faleide, J.I., Corfu, F., Tegner, C., Shephard, G.E., Zastrozhnov, D., Myklebust, R., 2015. The ocean-continent transition in the mid-Norwegian margin: Insight from seismic data and an onshore Caledonian field analogue. Geology 43, 1011-1014. doi: 10.1130/g37086.1

Abdelmalak, M.M., Bulois, C., Mourgues, R., Galland, O., Legland, J.B., Gruber, C., 2016a. Description of new dry granular materials of variable cohesion and friction coefficient: Implications for laboratory modelling of the brittle crust. Tectonophysics 684, 39-51. doi: 10.1016/j.tecto.2016.03.003

Abdelmalak, M.M., Planke, S., Faleide, J.I., Jerram, D.A., Zastrozhnov, D., Eide, S., Myklebust, R., 2016b. The development of volcanic sequences at rifted margins: New insights from the structure and morphology of the Vøring Escarpment, mid-Norwegian Margin. Journal of Geophysical Research: Solid Earth 121, 5212-5236. doi: 10.1002/2015JB012788

Agirrezabala, L.M., 2015. Syndepositional forced folding and related fluid plumbing above a magmatic laccolith: Insights from outcrop (Lower Cretaceous, Basque-Cantabrian Basin, western Pyrenees). Geological Society of America Bulletin 127, 982-1000. doi: 10.1130/b31192.1

Airoldi, G.M., Muirhead, J.D., Long, S.M., Zanella, E., White, J.D.L., 2016. Flow dynamics in mid-Jurassic dikes and sills of the Ferrar large igneous province and implications for long-distance magma transport. Tectonophysics 683, 182-199. doi: 10.1016/j.tecto.2016.06.029

Anderson, E., 1937. Cone-sheets and ring-dykes: The dynamical explanation. Bull Volcanol 1, 35-40

Anderson, E.M., 1936. IX.—The Dynamics of the Formation of Cone-sheets, Ring-dykes, and Caldron-subsidences. Proceedings of the Royal Society of Edinburgh 56, 128-157. doi: 10.1017/S0370164600014954

Bell, B., Butcher, H., 2002. On the emplacement of sill complexes: evidence from the Faroe-Shetland Basin, in: Jolley, D.W., Bell, B.R. (Eds.), The North Atlantic Igneous Province: Stratigraphy, Tectonic, Volcanic and Magmatic Processes, Geological Society, London, Special Publications, 307-329. doi: 10.1144/gsl.sp.2002.197.01.12

Berndt, C., Skogly, O.P., Planke, S., Eldholm, O., Mjelde, R., 2000. High-velocity breakup-related sills in the Vøring Basin, off Norway. Journal of Geophysical Research: Solid Earth 105, 28443-28454. doi: 10.1029/2000JB900217

Berndt, C., Planke, S., Alvestad, E., Tsikalas, F., Rasmussen, T., 2001. Seismic volcanostratigraphy of the Norwegian Margin: constraints on tectonomagmatic break-up processes. Journal of the Geological Society 158, 413-426. doi: 10.1144/jgs.158.3.413

Berndt, C., Hensen, C., Mortera-Gutierrez, C., Sarkar, S., Geilert, S., Schmidt, M., Liebetrau, V., Kipfer, R., Scholz, F., Doll, M., Muff, S., Karstens, J., Planke, S., Petersen, S., Böttner, C., Chi, W.-C., Moser, M., Behrendt, R., Fiskal, A., Lever, M., Su, C.-C., Deng, L., Brennwald,

M., Lizarralde, D., 2016. Rifting under steam—How rift magmatism triggers methane venting from sedimentary basins. Geology 44, 767-770. doi: 10.1130/g38049.1

Breitkreuz, C., Petford, N., 2004. Physical geology of high-level magmatic systems, Geological Society London Special Publication, London. 262. doi: 10.1144/GSL.SP.2004.234.01.17

Breitkreuz, C., Ehling, B.-C., Sergeev, S., 2009. Chronological evolution of an intrusive/extrusive system: the Late Paleozoic Halle Volcanic Complex in the northeastern Saale Basin (Germany) [Geochronologische Entwicklung eines Intrusiv-/Extrusiv-Systems: der spätpaläozoische Halle-Vulkanit-Komplex im nordöstlichen Saale-Becken (Deutschland).]. Zeitschrift der Deutschen Gesellschaft für Geowissenschaften 160, 173-190. doi: 10.1127/1860-1804/2009/0160-0173

Breitkreuz, C., Ehling, B.-C., Pastrik, N., 2018. The Subvolcanic Units of the Late Paleozoic Halle Volcanic Complex, Germany: Geometry, Internal Textures and Emplacement Mode, in: Breitkreuz, C., Rocchi, S. (Eds.), Physical Geology of Shallow Magmatic Systems: Dykes, Sills and Laccoliths. Advances in Volcanology, Springer International Publishing, 295-307. doi: 10.1007/978-3-319-14084-1_2

Brothelande, E., Merle, O., 2015. Estimation of magma depth for resurgent domes: An experimental approach. Earth and Planetary Science Letters 412, 143-151. doi: 10.1016/j.epsl.2014.12.011

Brothelande, E., Peltier, A., Got, J.L., Merle, O., Lardy, M., Garaebiti, E., 2016. Constraints on the source of resurgent doming inferred from analogue and numerical modeling — Implications on the current feeding system of the Yenkahe dome–Yasur volcano complex (Vanuatu). Journal of Volcanology and Geothermal Research 322, 225-240. doi: 10.1016/j.jvolgeores.2015.11.023

Bryan, S.E., Peate, I.U., Peate, D.W., Self, S., Jerram, D.A., Mawby, M.R., Marsh, J.S., Miller, J.A., 2010. The largest volcanic eruptions on Earth. Earth-Science Reviews 102, 207-229. doi: 10.1016/j.earscirev.2010.07.001

Bunger, A.P., Cruden, A.R., 2011. Modeling the growth of laccoliths and large mafic sills: Role of magma body forces. Journal of Geophysical Research: Solid Earth 116, 1-18. doi: 10.1029/2010JB007648

Burchardt, S., Troll, V.R., Mathieu, L., Emeleus, H.C., Donaldson, C.H., 2013. Ardnamurchan 3D cone-sheet architecture explained by a single elongate magma chamber. Scientific Reports 3, 1-7. doi: 10.1038/srep02891

Burchardt, S., 2018. Volcanic and Igneous Plumbing Systems: Understanding Magma Transport, Storage, and Evolution in the Earth's Crust, Elsevier. 356

Bureau, D., Mourgues, R., Cartwright, J., 2014. Use of a new artificial cohesive material for physical modelling: Application to sandstone intrusions and associated fracture networks. Journal of Structural Geology 66, 223-236. doi: 10.1016/j.jsg.2014.05.024

Canales, J.P., Dunn, R.A., Arai, R., Sohn, R.A., 2017. Seismic imaging of magma sills beneath an ultramafic-hosted hydrothermal system. Geology 45, 451-454. doi: 10.1130/g38795.1

Cartwright, J., Hansen, D.M., 2006. Magma transport through the crust via interconnected sill complexes. Geology 34, 929-932. doi: 10.1130/g22758a.1

Cartwright, J., James, D., Huuse, M., Vetel, W., Hurst, A., 2008. The geometry and emplacement of conical sandstone intrusions. Journal of Structural Geology 30, 854-867. doi: 10.1016/j.jsg.2008.03.012

Castro, J.M., Cordonnier, B., Schipper, C.I., Tuffen, H., Baumann, T.S., Feisel, Y., 2016. Rapid laccolith intrusion driven by explosive volcanic eruption. Nature Communications 7, 1-7. doi: 10.1038/ncomms13585

Chevallier, L., Woodford, A., 1999. Morpho-tectonics and mechanism of emplacement of the dolerite rings and sills of the western Karoo, South Africa. South African Journal of Geology 102, 43-54

Chevallier, L.P., Goedhart, M.L., Woodford, A.C., 2001. Influence of Dolerite Sill and Ring Complexes on the Occurrence of Groundwater in Karoo Fractured Aquifers: A Morpho-tectonic Approach: Report to the Water Research Commission, Water Research Commission

Coetzee, A., Kisters, A.F.M., 2017. Dyke-sill relationships in Karoo dolerites as indicators of propagation and emplacement processes of mafic magmas in the shallow crust. Journal of Structural Geology 97, 172-188. doi: 10.1016/j.jsg.2017.03.002

Corry, C.E., 1988. Laccoliths; Mechanics of emplacement and growth, Geological Society of America Special Papers, Boulder, Colorado. 114. doi: 10.1130/SPE220-p1

Cosgrove, J.W., Hillier, R.D., 1999. Forced-fold development within Tertiary sediments of the Alba Field, UKCS: evidence of differential compaction and post-depositional sandstone remobilization, in: Cosgrove, J.W., Ameen, M.S. (Eds.), Forced Folds and Fractures, Geological Society, London, Special Publications, 61-71. doi: 10.1144/gsl.sp.2000.169.01.05

Cruden, A.R., McCaffrey, K.J.W., Bunger, A.P., 2018. Geometric Scaling of Tabular Igneous Intrusions: Implications for Emplacement and Growth, in: Breitkreuz, C., Rocchi, S. (Eds.), Physical Geology of Shallow Magmatic Systems: Dykes, Sills and Laccoliths, Springer International Publishing, 11-38. doi: 10.1007/978-3-319-14084-1_1000

Cukur, D., Horozal, S., Kim, D.C., Lee, G.H., Han, H.C., Kang, M.H., 2010. The distribution and characteristics of the igneous complexes in the northern East China Sea Shelf Basin and their implications for hydrocarbon potential. Marine Geophysical Researches 31, 299-313. doi: 10.1007/s11001-010-9112-y

Currier, R.M., Marsh, B.D., 2015. Mapping real time growth of experimental laccoliths: The effect of solidification on the mechanics of magmatic intrusion. Journal of Volcanology and Geothermal Research 302, 211-224. doi: 10.1016/j.jvolgeores.2015.07.009

Currier, R.M., Forsythe, P., Grossmeier, C., Laliberte, M., Yagle, B., 2017. Experiments on the evolution of laccolith morphology in plan-view. Journal of Volcanology and Geothermal Research, 1-13. doi: 10.1016/j.volgeores.2017.02.017

Daly, R.A., 1905. The Classification of Igneous Intrusive Bodies. The Journal of Geology 13, 485-508

Davis, R.O., Selvadurai, A.P., 2005. Plasticity and geomechanics, Cambridge University Press. 300. doi: 10.1017/CBO9780511614958

de Saint-Blanquat, M., Habert, G., Horsman, E., Morgan, S.S., Tikoff, B., Launeau, P., Gleizes, G., 2006. Mechanisms and duration of non-tectonically assisted magma emplacement in the upper crust: The Black Mesa pluton, Henry Mountains, Utah. Tectonophysics 428, 1-31. doi: 10.1016/j.tecto.2006.07.014

Delpino, D., Bermúdez, A., Vitulli, N., Loscerbo, C., 2014. Sistema de Petróleo no convencional relacionado con lacolitos Eocenos de intraplaca. Área altiplanicie del Payún, cuenca Neuquina, IX Congreso de Exploración y Desarrollo de Hidrocarburos. Instituto Argentino del Petróleo y el Gas, Mendoza, 223-242

Dingwell, D. B., Bagdassarov, N., Bussod, G., & Webb, S. L. (1993). Magma rheology. In R. W. Luth (Ed.), Experiments at high pressure and applications to the Earth's mantle—Short course handbook (Chapter 5), (pp. 131–196). Edmonton, Alberta: Mineralogical Association of Canada.

Dini, A., Innocenti, F., Rocchi, S., Tonarini, S., Westerman, D.S., 2002. The magmatic evolution of the late Miocene laccolith–pluton–dyke granitic complex of Elba Island, Italy. Geological Magazine 139, 257-279. doi: 10.1017/S0016756802006556

Dixon, J.M., Simpson, D.G., 1987. Centrifuge modelling of laccolith intrusion. Journal of Structural Geology 9, 87-103. doi: 10.1016/0191-8141(87)90046-0

du Toit, A., 1920. The Karoo dolerites of South Africa: a study in hypabyssal injection. Transactions of the Geological Society of South Africa 23, 1-42

Eide, C.H., Schofield, N., Jerram, D.A., Howell, J.A., 2016. Basin-scale architecture of deeply emplaced sill complexes: Jameson Land, East Greenland. Journal of the Geological Society, 1-18. doi: 10.1144/jgs2016-018

Eide, C.H., Schofield, N., Lecomte, I., Buckley, S.J., Howell, J.A., 2017. Seismic interpretation of sill complexes in sedimentary basins: implications for the sub-sill imaging problem. Journal of the Geological Society, 1-17. doi: 10.1144/jgs2017-096

Einsele, G., Gieskes, J.M., Curray, J., Moore, D.M., Aguayo, E., Aubry, M.-P., Fornari, D., Guerrero, J., Kastner, M., Kelts, K., Lyle, M., Matoba, Y., Molina-Cruz, A., Niemitz, J., Rueda, J., Saunders, A., Schrader, H., Simoneit, B., Vacquier, V., 1980. Intrusion of basaltic sills into highly porous sediments, and resulting hydrothermal activity. Nature 283, 441-445. doi: 10.1038/283441a0

Francis, E.H., 1982. Magma and sediment-I Emplacement mechanism of late Carboniferous tholeiite sills in northern Britain. President's anniversary address 1981 139, 1-20. doi: 10.1144/gsjgs.139.1.0001

Frieling, J., Svensen, H., Planke, S., Cramwinckel, M.J., Selnes, H., Sluijs, A., 2016. Thermogenic methane release as a cause for the long duration of the PETM. Proceedings of the National Academy of Sciences, 1-6. doi: 10.1073/pnas.1603348113

Galerne, C.Y., Neumann, E.-R., Planke, S., 2008. Emplacement mechanisms of sill complexes: Information from the geochemical architecture of the Golden Valley Sill Complex, South Africa. Journal of Volcanology and Geothermal Research 177, 425-440. doi: 10.1016/j.jvolgeores.2008.06.004

Galerne, C.Y., Galland, O., Neumann, E.-R., Planke, S., 2011. 3D relationships between sills and their feeders: evidence from the Golden Valley Sill Complex (Karoo Basin) and experimental modelling. Journal of Volcanology and Geothermal Research 202, 189-199. doi: 10.1016/j.jvolgeores.2011.02.006

Galland, O., De Bremond d'Ars, J., Cobbold, P.R., Hallot, E., 2003. Physical models of magmatic intrusion during thrusting. Terra Nova 15, 405-409. doi: 10.1046/j.1365-3121.2003.00512.x

Galland, O., Cobbold, P.R., Hallot, E., de Bremond d'Ars, J., Delavaud, G., 2006. Use of vegetable oil and silica powder for scale modelling of magmatic intrusion in a deforming brittle crust. Earth and Planetary Science Letters 243, 786-804. doi: 10.1016/j.epsl.2006.01.014

Galland, O., Planke, S., Neumann, E.-R., Malthe-Sørenssen, A., 2009. Experimental modelling of shallow magma emplacement: Application to saucer-shaped intrusions. Earth and Planetary Science Letters 277, 373-383. doi: 10.1016/j.epsl.2008.11.003

Galland, O., 2012. Experimental modelling of ground deformation associated with shallow magma intrusions. Earth and Planetary Science Letters 317, 145-156. doi: 10.1016/j.epsl.2011.10.017

Galland, O., Scheibert, J., 2013. Analytical model of surface uplift above axisymmetric flat-lying magma intrusions: Implications for sill emplacement and geodesy. Journal of Volcanology and Geothermal Research 253, 114-130. doi: 10.1016/j.jvolgeores.2012.12.006

Galland, O., Burchardt, S., Hallot, E., Mourgues, R., Bulois, C., 2014. Dynamics of dikes versus cone sheets in volcanic systems. Journal of Geophysical Research: Solid Earth 119, 6178-6192. doi: 10.1002/2014JB011059

Galland, O., Holohan, E., van Wyk de Vries, B., Burchardt, S., 2018a. Laboratory Modelling of Volcano Plumbing Systems: A Review, in: Breitkreuz, C., Rocchi, S. (Eds.), Physical Geology of Shallow Magmatic Systems: Dykes, Sills and Laccoliths. Advances in Volcanology, Springer International Publishing, 147-214. doi: 10.1007/978-3-319-14084-1_9

Galland, O., Schmiedel, T., Bertelsen, H., Guldstrand, F., Haug, Ø.T., Souche, A., 2018b. Geomechanical Modeling of Fracturing and Damage induced by Igneous Intrusions: Implications for Fluid Flow in Volcanic Basins, X Congreso de Exploración y Desarrollo de Hidrocarburos. Instituto Argentino del Petróleo y el Gas, Mendoza, 1-16

Galland, O., Bertelsen, H.S., Eide, C.H., Guldstrand, F., Haug, Ø.T., Leanza, H.A., Mair, K., Palma, O., Planke, S., Rabbel, O., Schmiedel, T., Souche, A., Spacapan, J.B., 2018. Storage and Transport of Magma in the Layered Crust-Formation of Sills and Related Flat-Lying Intrusions, in: Burchardt, S. (Ed.), Volcanic and Igneous Plumbing Systems, 1st ed, Elsevier, 111-136. doi: 10.1016/B978-0-12-809749-6.00005-4

Galley, A.G., Hannington, M., Jonasson, I., 2007. Volcanogenic massive sulphide deposits, in: Goodfellow, W.D. (Ed.), Mineral deposits of Canada: A synthesis of major deposit-types, district metallogeny, the evolution of geological provinces, and exploration methods, Geological Association of Canada, Mineral Deposits Division, Special Publication 5, 141-161

Gerbault, M., Cappa, F., Hassani, R., 2012. Elasto-plastic and hydromechanical models of failure around an infinitely long magma chamber. Geochemistry, Geophysics, Geosystems 13, 1-27. doi: 10.1029/2011GC003917

Gerbault, M., Hassani, R., Novoa Lizama, C., Souche, A., 2018. Three-Dimensional Failure Patterns Around an Inflating Magmatic Chamber. Geochemistry, Geophysics, Geosystems, 1-23. doi: 10.1002/2017GC007174

Gilbert, G.K., 1877. Report on the Geology of the Henry Mountains, U. S. Geographical Geological Survey of the Rocky Mountain, Region, Washington. 160

Glazner, A.F., Bartley, J.M., 2006. Is stoping a volumetrically significant pluton emplacement process? GSA Bulletin 118, 1185-1195. doi: 10.1130/B25738.1

Goulty, N.R., Schofield, N., 2008. Implications of simple flexure theory for the formation of saucer-shaped sills. Journal of Structural Geology 30, 812-817. doi: 10.1016/j.jsg.2008.04.002

Gudmundsson, A., Løtveit, I.F., 2014. Sills as fractured hydrocarbon reservoirs: examples and models. Geological Society, London, Special Publications 374, 251-271. doi: 10.1144/sp374.5

Gudmundsson, A., Pasquarè, F.A., Tibaldi, A., 2014. Dykes, Sills, Laccoliths, and Inclined Sheets in Iceland. Advances in Volcanology, Springer Berlin Heidelberg, 1-14. doi: 10.1007/11157_2014_1

Guldstrand, F., Burchardt, S., Hallot, E., Galland, O., 2017. Dynamics of Surface Deformation Induced by Dikes and Cone Sheets in a Cohesive Coulomb Brittle Crust. Journal of Geophysical Research: Solid Earth, 1-14. doi: 10.1002/2017JB014346

Guldstrand, F., Galland, O., Hallot, E., Burchardt, S., 2018. Experimental Constraints on Forecasting the Location of Volcanic Eruptions from Pre-eruptive Surface Deformation. Frontiers in Earth Science 6, 1-9. doi: 10.3389/feart.2018.00007

Habert, G., de Saint-Blanquat, M., 2004. Rate of construction of the Black Mesa bysmalith, Henry Mountains, Utah. Geological Society, London, Special Publications 234, 163-173. doi: 10.1144/gsl.sp.2004.234.01.10

Hall, J., 1815. II. On the Vertical Position and Convolutions of certain Strata, and their relation with Granite. Transactions of the Royal Society of Edinburgh 7, 79-108. doi: 10.1017/S0080456800019268

Hansen, D.M., Cartwright, J.A., Thomas, D., 2004. 3D Seismic Analysis of the Geometry of Igneous Sills and Sill Junction Relationships. Geological Society, London, Memoirs 29, 199-208. doi: 10.1144/gsl.mem.2004.029.01.19

Hansen, D.M., Cartwright, J., 2006. The three-dimensional geometry and growth of forced folds above saucer-shaped igneous sills. Journal of Structural Geology 28, 1520-1535. doi: 10.1016/j.jsg.2006.04.004

Haug, Ø.T., Galland, O., Souloumiac, P., Souche, A., Guldstrand, F., Schmiedel, T., 2017. Inelastic damage as a mechanical precursor for the emplacement of saucer-shaped intrusions. Geology 45, 1099-1102. doi: 10.1130/G39361.1

Haug, Ø.T., Galland, O., Souloumiac, P., Souche, A., Guldstrand, F., Schmiedel, T., Maillot, B., 2018. Shear versus tensile failure mechanisms induced by sill intrusions – Implications for emplacement of conical and saucer-shaped intrusions. Journal of Geophysical Research - Solid Earth 123, 1-20. doi: 10.1002/2017JB015196

Heimdal, T.H., Svensen, H.H., Ramezani, J., Iyer, K., Pereira, E., Rodrigues, R., Jones, M.T., Callegaro, S., 2018. Large-scale sill emplacement in Brazil as a trigger for the end-Triassic crisis. Scientific Reports 8, 1-12. doi: 10.1038/s41598-017-18629-8

Horsman, E., Morgan, S., de Saint-Blanquat, M., Habert, G., Nugent, A., Hunter, R.A., Tikoff, B., 2009. Emplacement and assembly of shallow intrusions from multiple magma pulses, Henry Mountains, Utah. Earth and Environmental Science Transactions of the Royal Society of Edinburgh 100, 117-132. doi: 10.1017/S1755691009016089

Hunt, C.B., Averitt, P., Miller, R.L., 1953. Geology and geography of the Henry Mountains region, Utah, Professional Paper, Washington, D.C., 244

Hurst, A., Vigorito, M., 2017. Saucer-shaped sandstone intrusions: An underplayed reservoir target. AAPG Bull 101, 625-633. doi: 10.1306/011817DIG17070

Hutton, D., 2009. Insights into magmatism in volcanic margins: bridge structures and a new mechanism of basic sill emplacement–Theron Mountains, Antarctica. Petroleum Geoscience 15, 269-278. doi: 10.1144/1354-079309-841

Huuse, M., Duranti, D., Steinsland, N., Guargena, C.G., Prat, P., Holm, K., Cartwright, J.A., Hurst, A., 2004. Seismic Characteristics of Large-Scale Sandstone Intrusions in the Paleogene of the South Viking Graben, UK and Norwegian North Sea. Geological Society, London, Memoirs 29, 263-278. doi: 10.1144/gsl.mem.2004.029.01.25

Hyndman, D., Alt, D., 1987. Radial dikes, laccoliths, and gelatin models. The Journal of Geology 95, 763-774. doi: 10.1086/629176

Iddings, J.P., 1898. Bysmaliths. The Journal of Geology 6, 704-710

Iyer, K., Rüpke, L., Galerne, C.Y., 2013. Modeling fluid flow in sedimentary basins with sill intrusions: Implications for hydrothermal venting and climate change. Geochemistry, Geophysics, Geosystems 14, 5244-5262. doi: 10.1002/2013GC005012

Iyer, K., Schmid, D.W., Planke, S., Millett, J., 2017. Modelling hydrothermal venting in volcanic sedimentary basins: Impact on hydrocarbon maturation and paleoclimate. Earth and Planetary Science Letters 467, 30-42. doi: 10.1016/j.epsl.2017.03.023

Jackson, C.A.-L., Schofield, N., Golenkov, B., 2013. Geometry and controls on the development of igneous sill–related forced folds: A 2-D seismic reflection case study from offshore southern Australia. Geological Society of America Bulletin 125, 1874-1890. doi: 10.1130/b30833.1

Jackson, M.D., Pollard, D.D., 1990. Flexure and faulting of sedimentary host rocks during growth of igneous domes, Henry Mountains, Utah. Journal of Structural Geology 12, 185-206. doi: 10.1016/0191-8141(90)90004-I

Jerram, D.A., Bryan, S.E., 2018. Plumbing Systems of Shallow Level Intrusive Complexes, in: Breitkreuz, C., Rocchi, S. (Eds.), Advances in Volcanology, Springer Berlin Heidelberg, 1-22. doi: 10.1007/11157_2015_8

Johnson, A.M., Pollard, D.D., 1973. Mechanics of growth of some laccolithic intrusions in the Henry mountains, Utah, I. Tectonophysics 18, 261-309. doi: 10.1016/0040-1951(73)90050-4

Karlstrom, L., Paterson, S.R., Jellinek, A.M., 2017. A reverse energy cascade for crustal magma transport. Nature Geosci 10, 604-608. doi: 10.1038/ngeo2982

Kavanagh, J.L., Menand, T., Sparks, R.S.J., 2006. An experimental investigation of sill formation and propagation in layered elastic media. Earth and Planetary Science Letters 245, 799-813. doi: 10.1016/j.epsl.2006.03.025

Kavanagh, J.L., Boutelier, D., Cruden, A.R., 2015. The mechanics of sill inception, propagation and growth: Experimental evidence for rapid reduction in magmatic overpressure. Earth and Planetary Science Letters 421, 117-128. doi: 10.1016/j.epsl.2015.03.038

Kavanagh, J.L., Rogers, B.D., Boutelier, D., Cruden, A.R., 2017. Controls on sill and dyke-sill hybrid geometry and propagation in the crust: The role of fracture toughness. Tectonophysics 698, 109-120. doi: 10.1016/j.tecto.2016.12.027

Kavanagh, J.L., Engwell, S., Martin, S., 2018. A review of laboratory and numerical modelling in volcanology. Solid Earth Discussions 9, 531–571. doi: 10.5194/se-2017-40

Kennedy, B.M., Holohan, E.P., Stix, J., Gravley, D.M., Davidson, J.R.J., Cole, J.W., 2018. Magma plumbing beneath collapse caldera volcanic systems. Earth-Science Reviews 177, 404-424. doi: 10.1016/j.earscirev.2017.12.002

Kerr, A.D., Pollard, D.D., 1998. Toward more realistic formulations for the analysis of laccoliths. Journal of Structural Geology 20, 1783-1793. doi: 10.1016/S0191-8141(98)00071-6

Kjoberg, S., Schmiedel, T., Planke, S., Svensen, H.H., Millett, J.M., Jerram, D.A., Galland, O., Lecomte, I., Schofield, N., Haug, Ø.T., Helsem, A., 2017. 3D structure and formation of hydrothermal vent complexes at the Paleocene-Eocene transition, the Møre Basin, mid-Norwegian margin. Interpretation 5, SK65-SK81. doi: 10.1190/int-2016-0159.1

Klarner, S., Klarner, O., 2012. Identification of Paleo-Volcanic Rocks on Seismic Data, in: Stoppa, F. (Ed.), Updates in Volcanology - A Comprehensive Approach to Volcanological Problems, InTech, 181-206. doi: 10.5772/24943

Klinkmüller, M., Schreurs, G., Rosenau, M., Kemnitz, H., 2016. Properties of granular analogue model materials: A community wide survey. Tectonophysics 684, 23-38. doi: 10.1016/j.tecto.2016.01.017

Kontorovich, A.E., Khomenko, A.V., Burshtein, L.M., Likhanov, I.I., Pavlov, A.L., Staroseltsev, V.S., Ten, A.A., 1997. Intense basic magmatism in the Tunguska petroleum basin, eastern Siberia, Russia. Petroleum Geoscience 3, 359-369. doi: 10.1144/petgeo.3.4.359

Kuenen, P.H., 1937. Intrusion of Cone-Sheets. Geological Magazine 74, 177-183. doi: 10.1017/S0016756800088713

Le Bas, M.J., 1971. Cone-sheets as a mechanism of uplift. Geological Magazine 108, 373-376. doi: 10.1017/S0016756800056399

Lorenz, V., Haneke, J., 2004. Relationship between diatremes, dykes, sills, laccoliths, intrusive-extrusive domes, lava flows, and tephra deposits with unconsolidated water-saturated

sediments in the late Variscan intermontane Saar-Nahe Basin, SW Germany. Geological Society, London, Special Publications 234, 75-124. doi: 10.1144/gsl.sp.2004.234.01.07

MacCarthy, G.R., 1925. Some Facts and Theories concerning Laccoliths. The Journal of Geology 33, 1-18

Magee, C., Briggs, F., Jackson, C.A.L., 2013. Lithological controls on igneous intrusion-induced ground deformation. Journal of the Geological Society 170, 853-856. doi: 10.1144/jgs2013-029

Magee, C., Jackson, C.A.-L., Schofield, N., 2014. Diachronous sub-volcanic intrusion along deep-water margins: insights from the Irish Rockall Basin. Basin Research 26, 85-105. doi: 10.1111/bre.12044

Magee, C., Duffy, O.B., Purnell, K., Bell, R.E., Jackson, C.A.L., Reeve, M.T., 2015. Fault-controlled fluid flow inferred from hydrothermal vents imaged in 3D seismic reflection data, offshore NW Australia. Basin Research, 1-20. doi: 10.1111/bre.12111

Magee, C., Muirhead, J.D., Karvelas, A., Holford, S.P., Jackson, C.A.L., Bastow, I.D., Schofield, N., Stevenson, C.T.E., McLean, C., McCarthy, W., 2016. Lateral magma flow in mafic sill complexes. Geosphere 12, 809-841. doi: 10.1130/GES01256.1

Magee, C., Bastow, I.D., van Wyk de Vries, B., Jackson, C.A.-L., Hetherington, R., Hagos, M., Hoggett, M., 2017a. Structure and dynamics of surface uplift induced by incremental sill emplacement. Geology 45, 431-434. doi: 10.1130/g38839.1

Magee, C., Jackson, C.A.-L., Hardman, J.P., Reeve, M.T., 2017b. Decoding sill emplacement and forced fold growth in the Exmouth Sub-basin, offshore northwest Australia: Implications for hydrocarbon exploration. Interpretation 5, SK11-SK22. doi: 10.1190/int-2016-0133.1

Malthe-Sørenssen, A., Planke, S., Svensen, H., Jamtveit, B., 2004. Formation of saucer-shaped sills, in: Breitkreuz, C., Petford, N. (Eds.), Physical Geology of High-Level Magmatic Systems, Geological Society, London, Special Publications, 215-227. doi: 10.1144/gsl.sp.2004.234.01.13

Mark, N.J., Schofield, N., Pugliese, S., Watson, D., Holford, S., Muirhead, D., Brown, R., Healy, D., 2017. Igneous intrusions in the Faroe Shetland basin and their implications for hydrocarbon exploration; new insights from well and seismic data. Marine and Petroleum Geology 92, 733-753. doi: 10.1016/j.marpetgeo.2017.12.005

Mattsson, T., Burchardt, S., Almqvist, B.S.G., Ronchin, E., 2018. Syn-Emplacement Fracturing in the Sandfell Laccolith, Eastern Iceland—Implications for Rhyolite Intrusion Growth and Volcanic Hazards. Frontiers in Earth Science 6, 1-22. doi: 10.3389/feart.2018.00005

McCaffrey, K.J.W., Petford, N., 1997. Are granitic intrusions scale invariant? Journal of the Geological Society 154, 1-4. doi: 10.1144/gsjgs.154.1.0001

Menand, T., 2008. The mechanics and dynamics of sills in layered elastic rocks and their implications for the growth of laccoliths and other igneous complexes. Earth and Planetary Science Letters 267, 93-99. doi: 10.1016/j.epsl.2007.11.043

Michaut, C., 2011. Dynamics of magmatic intrusions in the upper crust: Theory and applications to laccoliths on Earth and the Moon. Journal of Geophysical Research: Solid Earth 116, 1-19. doi: 10.1029/2010JB008108

Millett, J.M., Jerram, D.A., Planke, S., 2016. VMAPP CM5 – Volcanic Basin Petroleum Systems. VMAPP project report and PowerPoint file, VBPR/DougalEARTH/TGS (Confidential report), Oslo. 228

Montanari, D., Corti, G., Sani, F., Del Ventisette, C., Bonini, M., Moratti, G., 2010. Experimental investigation on granite emplacement during shortening. Tectonophysics 484, 147-155. doi: 10.1016/j.tecto.2009.09.010

Montanari, D., Agostini, A., Bonini, M., Corti, G., Ventisette, C.D., 2017a. The Use of Empirical Methods for Testing Granular Materials in Analogue Modelling. Materials 10, 1-18. doi: 10.3390/ma10060635

Montanari, D., Bonini, M., Corti, G., Agostini, A., Del Ventisette, C., 2017b. Forced folding above shallow magma intrusions: Insights on supercritical fluid flow from analogue modelling. Journal of Volcanology and Geothermal Research 345, 67-80. doi: 10.1016/j.jvolgeores.2017.07.022

Morgan, S., Stanik, A., Horsman, E., Tikoff, B., de Saint Blanquat, M., Habert, G., 2008. Emplacement of multiple magma sheets and wall rock deformation: Trachyte Mesa intrusion, Henry Mountains, Utah. Journal of Structural Geology 30, 491-512. doi: 10.1016/j.jsg.2008.01.005

Mourgues, R., Bureau, D., Bodet, L., Gay, A., Gressier, J.B., 2012. Formation of conical fractures in sedimentary basins: Experiments involving pore fluids and implications for sandstone intrusion mechanisms. Earth and Planetary Science Letters 313–314, 67-78. doi: 10.1016/j.epsl.2011.10.029

Muirhead, J.D., Airoldi, G., White, J.D.L., Rowland, J.V., 2014. Cracking the lid: Sill-fed dikes are the likely feeders of flood basalt eruptions. Earth and Planetary Science Letters 406, 187-197. doi: 10.1016/j.epsl.2014.08.036

Olive, J.-A., Crone, T.J., 2018. Smoke Without Fire: How Long Can Thermal Cracking Sustain Hydrothermal Circulation in the Absence of Magmatic Heat? Journal of Geophysical Research: Solid Earth 123, 4561-4581. doi: 10.1029/2017JB014900

Omosanya, K.O., Johansen, S.E., Eruteya, O.E., Waldmann, N., 2017. Forced folding and complex overburden deformation associated with magmatic intrusion in the Vøring Basin, offshore Norway. Tectonophysics 706-707, 14-34. doi: 10.1016/j.tecto.2017.03.026

Omosanya, K.O., Eruteya, O.E., Siregar, E.S.A., Zieba, K.J., Johansen, S.E., Alves, T.M., Waldmann, N.D., 2018. Three-dimensional (3-D) seismic imaging of conduits and radial faults associated with hydrothermal vent complexes (Vøring Basin, Offshore Norway). Marine Geology 399, 115-134. doi: 10.1016/j.margeo.2018.02.007

Peace, A., McCaffrey, K., Imber, J., Hobbs, R., van Hunen, J., Gerdes, K., 2017. Quantifying the influence of sill intrusion on the thermal evolution of organic-rich sedimentary rocks in nonvolcanic passive margins: an example from ODP 210-1276, offshore Newfoundland, Canada. Basin Research 29, 249-265. doi: 10.1111/bre.12131

Phillips, W.J., 1974. The dynamic emplacement of cone sheets. Tectonophysics 24, 69-84. doi: 10.1016/0040-1951(74)90130-9

Planke, S., Rasmussen, T., Rey, S.S., Myklebust, R., 2005. Seismic characteristics and distribution of volcanic intrusions and hydrothermal vent complexes in the Vøring and Møre basins. Geological Society, London, Petroleum Geology Conference series 6, 833-844. doi: 10.1144/0060833

Planke, S., Millett, J.M., Maharjan, D., Jerram, D.A., Abdelmalak, M.M., Groth, A., Hoffmann, J., Berndt, C., Myklebust, R., 2017. Igneous seismic geomorphology of buried lava fields and coastal escarpments on the Vøring volcanic rifted margin. Interpretation 5, SK161-SK177. doi: 10.1190/int-2016-0164.1

Planke, S., Svensen, H., Myklebust, R., Bannister, S., Manton, B., Lorenz, L., 2018. Geophysics and Remote Sensing, in: Breitkreuz, C., Rocchi, S. (Eds.), Advances in Volcanology, Springer Berlin Heidelberg, 1-16. doi: 10.1007/11157_2014_6

Pollard, D.D., 1973. Derivation and evaluation of a mechanical model for sheet intrusions. Tectonophysics 19, 233-269. doi: 10.1016/0040-1951(73)90021-8

Pollard, D.D., Johnson, A.M., 1973. Mechanics of growth of some laccolithic intrusions in the Henry mountains, Utah, II: Bending and failure of overburden layers and sill formation. Tectonophysics 18, 311-354. doi: 10.1016/0040-1951(73)90051-6

Polteau, S., Ferré, E.C., Planke, S., Neumann, E.R., Chevallier, L., 2008a. How are saucer-shaped sills emplaced? Constraints from the Golden Valley Sill, South Africa. Journal of Geophysical Research: Solid Earth 113. doi: 10.1029/2008JB005620

Polteau, S., Mazzini, A., Galland, O., Planke, S., Malthe-Sørenssen, A., 2008b. Saucer-shaped intrusions: Occurrences, emplacement and implications. Earth and Planetary Science Letters 266, 195-204. doi: 10.1016/j.epsl.2007.11.015

Polteau, S., Hendriks, B.W.H., Planke, S., Ganerød, M., Corfu, F., Faleide, J.I., Midtkandal, I., Svensen, H.S., Myklebust, R., 2016. The Early Cretaceous Barents Sea Sill Complex: Distribution, 40Ar/39Ar geochronology, and implications for carbon gas formation. Palaeogeography, Palaeoclimatology, Palaeoecology 441, 83-95. doi: 10.1016/j.palaeo.2015.07.007

Potter, J., Konnerup-Madsen, J., 2003. A review of the occurrence and origin of abiogenic hydrocarbons in igneous rocks. Geol Soc Spec Publ 214, 151-173. doi 10.1144/Gsl.Sp.2003.214.01.10

Rabbel, O., Galland, O., Mair, K., Lecomte, I., Senger, K., Spacapan, J.B., Manceda, R., 2018. From field analogues to realistic seismic modelling: a case study of an oil-producing andesitic sill complex in the Neuquén Basin, Argentina. Journal of the Geological Society. doi: 10.144/jgs2017-116

Ramberg, H., 1981. Gravity, deformation, and the earth's crust: In theory, experiments, and geological application, Academic press, New York. 425

Ramsay, J.G., 1967. Folding and fracturing of rocks, McGraw-Hill Companies. 568

Rateau, R., Schofield, N., Smith, M., 2013. The potential role of igneous intrusions on hydrocarbon migration, West of Shetland. Petroleum Geoscience 19, 259-272. doi: 10.1144/petgeo2012-035

Reynolds, P., Planke, S., Millett, J.M., Jerram, D.A., Trulsvik, M., Schofield, N., Myklebust, R., 2017. Hydrothermal vent complexes offshore Northeast Greenland: A potential role in driving the PETM. Earth and Planetary Science Letters 467, 72-78. doi: 10.1016/j.epsl.2017.03.031

Reynolds, P., Holford, S., Schofield, N., Ross, A., 2018. The importance of subsurface lithology in controlling magma storage v. eruption: an example from offshore southern Australia. Journal of the Geological Society. doi: 10.1144/jgs2017-109

Rincón, M., Márquez, A., Herrera, R., Alonso-Torres, A., Granja-Bruña, J.L., van Wyk de Vries, B., 2018. Contrasting catastrophic eruptions predicted by different intrusion and collapse scenarios. Scientific Reports 8, 6178. doi: 10.1038/s41598-018-24623-5

Ritter, M.C., Leever, K., Rosenau, M., Oncken, O., 2016. Scaling the sandbox—Mechanical (dis)similarities of granular materials and brittle rock. Journal of Geophysical Research: Solid Earth, 1-17. doi: 10.1002/2016JB012915

Rocchi, S., Westerman, D.S., Dini, A., Farina, F., 2010. Intrusive sheets and sheeted intrusions at Elba Island, Italy. Geosphere 6, 225-236. doi: 10.1130/GES00551.1

Rodriguez Monreal, F., Villar, H.J., Baudino, R., Delpino, D., Zencich, S., 2009. Modeling an atypical petroleum system: A case study of hydrocarbon generation, migration and accumulation related to igneous intrusions in the Neuquen Basin, Argentina. Marine and Petroleum Geology 26, 590-605. doi: 10.1016/j.marpetgeo.2009.01.005

Roman-Berdiel, T., Gapais, D., Brun, J.P., 1995. Analogue models of laccolith formation. Journal of Structural Geology 17, 1337-1346. doi: 10.1016/0191-8141(95)00012-3

Roni, E., Westerman, D.S., Dini, A., Stevenson, C., Rocchi, S., 2014. Feeding and growth of a dyke–laccolith system (Elba Island, Italy) from AMS and mineral fabric data. Journal of the Geological Society 171, 413-424. doi: 10.1144/jgs2013-019

Rui, G.U.O., Gongcheng, Z., Jinwei, Z., Xingbin, Z., Junbang, L.I.U., Dawei, Y., Shuang, S., 2013. Fingered Intrusion of Shallow Saucer-shaped Igneous Sills: Insights from the Jiaojiang Sag, East China Sea. Acta Geologica Sinica - English Edition 87, 1306-1318. doi: 10.1111/1755-6724.12130

Salmachi, A., Rajabi, M., Reynolds, P., Yarmohammadtooski, Z., Wainman, C., 2016. The effect of magmatic intrusions on coalbed methane reservoir characteristics: A case study from the Hoskissons coalbed, Gunnedah Basin, Australia. International Journal of Coal Geology 165, 278-289. doi: 10.1016/j.coal.2016.08.025

Sánchez-Guillamón, O., Fernández-Salas, L., Vázquez, J.-T., Palomino, D., Medialdea, T., López-González, N., Somoza, L., León, R., 2018. Shape and Size Complexity of Deep Seafloor Mounds on the Canary Basin (West to Canary Islands, Eastern Atlantic): A DEM-Based Geomorphometric Analysis of Domes and Volcanoes. Geosciences 8, 37. doi: 10.3390/geosciences8020037

Scaillet, B., Pêcher, A., Rochette, P., Champenois, M., 1995. The Gangotri granite (Garhwal Himalaya): Laccolithic emplacement in an extending collisional belt. Journal of Geophysical Research: Solid Earth 100, 585-607. doi: 10.1029/94JB01664

Scaillet, B., Holtz, F., & Pichavant, M. (1997). Rheological properties of granitic magmas in their crystallization range. In J. L. Bouchez, D. H. W. Hutton, & W. E. Stephens (Eds.), Granite: From segregation of melt to emplacement fabrics (pp. 11–29). Dordrecht, Netherlands: Springer. doi: 10.1007/978-94-017-1717-5_2

Scheibert, J., Galland, O., Hafver, A., 2017. Inelastic deformation during sill and laccolith emplacement: Insights from an analytic elastoplastic model. Journal of Geophysical Research: Solid Earth, 1-23. doi: 10.1002/2016JB013754

Schmiedel, T., Breitkreuz, C., Görz, I., Ehling, B.-C., 2015. Geometry of laccolith margins: 2D and 3D models of the Late Paleozoic Halle Volcanic Complex (Germany). International Journal of Earth Sciences 104, 323-333. doi: 10.1007/s00531-014-1085-7

Schmiedel, T., Galland, O., Breitkreuz, C., 2017a. Dynamics of sill and laccolith emplacement in the brittle crust: role of host rock strength and deformation mode. Journal of Geophysical Research: Solid Earth 122, 8860–8871. doi: 10.1002/2017JB014468

Schmiedel, T., Kjoberg, S., Planke, S., Magee, C., Galland, O., Schofield, N., Jackson, C.A.-L., Jerram, D.A., 2017b. Mechanisms of overburden deformation associated with the emplacement of the Tulipan sill, mid-Norwegian margin. Interpretation 5, SK23-SK38. doi: 10.1190/int-2016-0155.1

Schofield, N., Stevenson, C., Reston, T., 2010. Magma fingers and host rock fluidization in the emplacement of sills. Geology 38, 63-66. doi: 10.1130/g30142.1

Schofield, N., Brown, D.J., Magee, C., Stevenson, C.T., 2012. Sill morphology and comparison of brittle and non-brittle emplacement mechanisms. Journal of the Geological Society 169, 127-141. doi: 10.1144/0016-76492011-078

Schofield, N., Alsop, I., Warren, J., Underhill, J.R., Lehné, R., Beer, W., Lukas, V., 2014. Mobilizing salt: Magma-salt interactions. Geology 42, 599-602. doi: 10.1130/g35406.1

Schofield, N., Holford, S., Millett, J., Brown, D., Jolley, D., Passey, S.R., Muirhead, D., Grove, C., Magee, C., Murray, J., Hole, M., Jackson, C.A.L., Stevenson, C., 2017. Regional magma plumbing and emplacement mechanisms of the Faroe-Shetland Sill Complex: implications for magma transport and petroleum systems within sedimentary basins. Basin Research 29, 41-63. doi: 10.1111/bre.12164

Schutter, S.R., 2003a. Occurrences of hydrocarbons in and around igneous rocks, in: Petford, N., McCaffrey, K.J.W. (Eds.), Geol Soc Spec Publ, Geological Society, London, Special Publications, 35-68. doi 10.1144/Gsl.Sp.2003.214.01.03

Schutter, S.R., 2003b. Hydrocarbon occurrence and exploration in and around igneous rocks, in: Petford, N., McCaffrey, K.J.W. (Eds.), Geol Soc Spec Publ, Geological Society, London, Special Publications, 7-33. doi: 10.1144/Gsl.Sp.2003.214.01.02

Senger, K., Buckley, S.J., Chevallier, L., Fagereng, Å., Galland, O., Kurz, T.H., Ogata, K., Planke, S., Tveranger, J., 2015. Fracturing of doleritic intrusions and associated contact zones: Implications for fluid flow in volcanic basins. Journal of African Earth Sciences 102, 70-85. doi: 10.1016/j.jafrearsci.2014.10.019

Senger, K., Millett, J., Planke, S., Ogata, K., Eide, C., Festøy, M., Galland, O., Jerram, D.A., 2017. Effects of igneous intrusions on the petroleum system: a review. First Break, 1-10. doi: 10.3997/1365-2397.2017011

Shanks III, W.C.P., Thurston, R., 2012. Volcanogenic massive sulfide occurrence model. U.S. Geological Survey Scientific Investigations Report 2010–5070–C, 345

Shoulders, S.J., Cartwright, J., Huuse, M., 2007. Large-scale conical sandstone intrusions and polygonal fault systems in Tranche 6, Faroe-Shetland Basin. Marine and Petroleum Geology 24, 173-188. doi: 10.1016/j.marpetgeo.2006.12.001

Słodczyk, E., Pietranik, A., Breitkreuz, C., Pędziwiatr, A., Bokła, M., Schab, K., Grodzicka, M., 2015. Formation of a laccolith by magma pulses: Evidence from modal and chemical composition of the 500 m long borehole section through the Permo-Carboniferous Landsberg laccolith (Halle Volcanic Complex). Geochemical Journal 49, 523-537. doi: 10.2343/geochemj.2.0382

Smallwood, J.R., Maresh, J., 2002. The properties, morphology and distribution of igneous sills: modelling, borehole data and 3D seismic from the Faroe-Shetland area, in: Jolley, D.W., Bell, B.R. (Eds.), The North Atlantic Igneous Province: Stratigraphy, Tectonic, Volcanic and Magmatic Processes, Geological Society, London, Special Publications, 271-306. doi: 10.1144/gsl.sp.2002.197.01.11

Spacapan, J.B., Galland, O., Leanza, H.A., Planke, S., 2017. Igneous sill and finger emplacement mechanism in shale-dominated formations: a field study at Cuesta del Chihuido, Neuquén Basin, Argentina. Journal of the Geological Society, 1-12. doi: 10.1144/jgs2016-056

Spacapan, J.B., Palma, J.O., Galland, O., Manceda, R., Rocha, E., D'Odorico, A., Leanza, H.A., 2018. Thermal impact of igneous sill-complexes on organic-rich formations and implications for petroleum systems: A case study in the northern Neuquén Basin, Argentina. Marine and Petroleum Geology 91, 519-531. doi: 10.1016/j.marpetgeo.2018.01.018

Stearns, D.W., 1978. Faulting and forced folding in the Rocky Mountains foreland. Geological Society of America Memoirs 151, 1-38. doi: 10.1130/MEM151-p1

Stephens, T.L., Walker, R.J., Healy, D., Bubeck, A., England, R.W., McCaffrey, K.J.W., 2017. Igneous sills record far-field and near-field stress interactions during volcano construction:

Isle of Mull, Scotland. Earth and Planetary Science Letters 478, 159-174. doi: 10.1016/j.epsl.2017.09.003

Sun, Q., Wu, S., Cartwright, J., Wang, S., Lu, Y., Chen, D., Dong, D., 2014. Neogene igneous intrusions in the northern South China Sea: Evidence from high-resolution three dimensional seismic data. Marine and Petroleum Geology 54, 83-95. doi: 10.1016/j.marpetgeo.2014.02.014

Svensen, H., Planke, S., Malthe-Sørenssen, A., Jamtveit, B., Myklebust, R., Rasmussen Eidem, T., Rey, S.S., 2004. Release of methane from a volcanic basin as a mechanism for initial Eocene global warming. Nature 429, 542-545. doi: 10.1038/nature02566

Svensen, H., Corfu, F., Polteau, S., Hammer, Ø., Planke, S., 2012. Rapid magma emplacement in the Karoo Large Igneous Province. Earth and Planetary Science Letters 325–326, 1-9. doi: 10.1016/j.epsl.2012.01.015

Svensen, H.H., Planke, S., Neumann, E.-R., Aarnes, I., Marsh, J.S., Polteau, S., Harstad, C.H., Chevallier, L., 2018a. Sub-Volcanic Intrusions and the Link to Global Climatic and Environmental Changes, in: Breitkreuz, C., Rocchi, S. (Eds.), Physical Geology of Shallow Magmatic Systems: Dykes, Sills and Laccoliths, Springer International Publishing, 1-24. doi: 10.1007/11157_2015_10

Svensen, H.H., Polteau, S., Cawthorn, G., Planke, S., 2018b. Sub-volcanic Intrusions in the Karoo Basin, South Africa, in: Breitkreuz, C., Rocchi, S. (Eds.), Physical Geology of Shallow Magmatic Systems: Dykes, Sills and Laccoliths, Springer International Publishing, 1-14. doi: 10.1007/11157_2014_7

Sydnes, M., Fjeldskaar, W., Løtveit, I.F., Grunnaleite, I., Cardozo, N., 2018. The importance of sill thickness and timing of sill emplacement on hydrocarbon maturation. Marine and Petroleum Geology 89, 500-514. doi: 10.1016/j.marpetgeo.2017.10.017

Symonds, P.A., Planke, S., Frey, O., Skogseid, J., 1998. Volcanic evolution of the Western Australian continental margin and its implications for basin development, in: Prucell, P.G., Prucell, R.R. (Eds.), West Australian Basin Symposium. Perth: Petroleum Exploration Society of Australia, Perth Convention Centre, Western Australia, 33-54

Thorey, C., Michaut, C., 2016. Elastic-plated gravity currents with a temperature-dependent viscosity. Journal of Fluid Mechanics 805, 88-117. doi: 10.1017/jfm.2016.538

Tibaldi, A., 2015. Structure of volcano plumbing systems: A review of multi-parametric effects. Journal of Volcanology and Geothermal Research 298, 85-135. doi: 10.1016/j.jvolgeores.2015.03.023

Timoshenko, S.P., Woinowsky-Krieger, S., 1959. Theory of plates and shells, McGraw-hill Book Company. 594

Trude, J., Cartwright, J., Davies, R.J., Smallwood, J.R., 2003. New technique for dating igneous sills. Geology 31, 813-816. doi: 10.1130/g19559.1

Turcotte, D.L., Schubert, G., 2014. Geodynamics, 3rd ed, Cambridge University Press. 636. doi: 10.2138/am-2015-659

Tweto, O., 1951. Form and Structure of Sills near Pando, Colorado. GSA Bulletin 62, 507-532. doi: 10.1130/0016-7606(1951)62[507:FASOSN]2.0.CO;2

Ventsel, E., Krauthammer, T., 2001. Thin plates and shells: theory: analysis, and applications, CRC press. 688

Vétel, W., Cartwright, J., 2010. Emplacement mechanics of sandstone intrusions: insights from the Panoche Giant Injection Complex, California. Basin Research 22, 783-807. doi: 10.1111/j.1365-2117.2009.00439.x

Villinger, H.W., Pichler, T., Kaul, N., Stephan, S., Pälike, H., Stephan, F., 2017. Formation of hydrothermal pits and the role of seamounts in the Guatemala Basin (Equatorial East Pacific) from heat flow, seismic, and core studies. Geochemistry, Geophysics, Geosystems 18, 369-383. doi: 10.1002/2016GC006665

Wilson, P.I.R., McCaffrey, K.J.W., Wilson, R.W., Jarvis, I., Holdsworth, R.E., 2016. Deformation structures associated with the Trachyte Mesa intrusion, Henry Mountains, Utah: Implications for sill and laccolith emplacement mechanisms. Journal of Structural Geology 87, 30-46. doi: 10.1016/j.jsg.2016.04.001

Witte, J., Bonora, M., Carbone, C., Oncken, O., 2012. Fracture evolution in oil-producing sills of the Rio Grande Valley, northern Neuquen Basin, Argentina. AAPG Bull 96, 1253-1277. doi: 10.1306/10181110152

Zhang, W., Wang, Q., Ye, J., Zhou, J., 2017. Fracture development and fluid pathways in shales during granite intrusion. International Journal of Coal Geology 183, 25-37. doi: 10.1016/j.coal.2017.09.011

Zhao, C., Hobbs, B.E., Ord, A., Peng, S., 2008. Particle simulation of spontaneous crack generation associated with the laccolithic type of magma intrusion processes. International Journal for Numerical Methods in Engineering 75, 1172-1193. doi: 10.1002/nme.2287

Zhao, F., Wu, S., Sun, Q., Huuse, M., Li, W., Wang, Z., 2014. Submarine volcanic mounds in the Pearl River Mouth Basin, northern South China Sea. Marine Geology 355, 162-172. doi: 10.1016/j.margeo.2014.05.018

Appendices

Content

A.1 Publication I

I

Schmiedel, T., Kjoberg, S., Planke, S., Magee, C., Galland, O., Schofield, N., Jackson, C.A.-L., Jerram, D.A., (2017). *Mechanisms of overburden deformation associated with the emplacement of the Tulipan sill, mid-Norwegian margin*. Interpretation 5, SK23-SK38. doi: 10.1190/int-2016-0155.1

Mechanisms of overburden deformation associated with the emplacement of the Tulipan sill, mid-Norwegian margin

Tobias Schmiedel[1], Sigurd Kjoberg[2], Sverre Planke[3], Craig Magee[4], Olivier Galland[1], Nick Schofield[5], Christopher A.-L. Jackson[4], and Dougal A. Jerram[6]

Abstract

The emplacement of igneous intrusions into sedimentary basins mechanically deforms the host rocks and causes hydrocarbon maturation. Existing models of host-rock deformation are investigated using high-quality 3D seismic and industry well data in the western Møre Basin offshore mid-Norway. The models include synemplacement (e.g., elastic bending-related active uplift and volume reduction of metamorphic aureoles) and postemplacement (e.g., differential compaction) mechanisms. We use the seismic interpretations of five horizons in the Cretaceous-Paleogene sequence (Springar, Tang, and Tare Formations) to analyze the host rock deformation induced by the emplacement of the underlying saucer-shaped Tulipan sill. The results show that the sill, emplaced between 55.8 and 54.9 Ma, is responsible for the overlying dome structure observed in the seismic data. Isochron maps of the deformed sediments, as well as deformation of the younger postemplacement sediments, document a good match between the spatial distribution of the dome and the periphery of the sill. The thickness t of the Tulipan is less than 100 m, whereas the amplitude f of the overlying dome ranges between 30 and 70 m. Spectral decomposition maps highlight the distribution of fractures in the upper part of the dome. These fractures are observed in between hydrothermal vent complexes in the outer parts of the dome structure. The 3D seismic horizon interpretation and volume rendering visualization of the Tulipan sill reveal fingers and an overall saucer-shaped geometry. We conclude that a combination of different mechanisms of overburden deformation, including (1) elastic bending, (2) shear failure, and (3) differential compaction, is responsible for the synemplacement formation and the postemplacement modification of the observed dome structure in the Tulipan area.

Introduction

Volcanic basins contain significant volumes of igneous rocks (Planke et al., 2015; Jerram and Bryan, 2017), e.g., the Karoo Basin (Svensen et al., 2012) and mid-Norwegian margin (Planke et al., 2005). In addition, they are explored for hydrocarbons all over the world (e.g., Senger et al., forthcoming), onshore and offshore, e.g., the Rockall Basin (e.g., Magee et al., 2014), the Faroe-Shetland Basin (e.g., Smallwood and Maresh, 2002), the Møre and Vøring Basins (e.g., Planke et al., 2005; Cartwright and Hansen, 2006), and the Neuquén Basin (e.g., Kay et al., 2006). The magma plumbing systems in these basins are primarily dominated by interconnected networks of sill intrusions, the emplacement of which can significantly deform the host rock and influence petroleum system development (Kontorovich et al., 1997; Thomson and Hutton, 2004; Cartwright and Hansen, 2006; de Saint-Blanquat et al., 2006; Morgan et al., 2008; Galerne et al., 2011; Schofield et al., 2015; Magee et al., 2016; Wilson et al., 2016). For example, numerous studies have demonstrated that sill intrusions may (1) locally heat and mature organic matter within the host rock, generating oil and/or gas (e.g., Rodriguez Monreal et al., 2009), (2) be associated with

[1]University of Oslo, Physics of Geological Processes (PGP), Department of Geosciences, Oslo, Norway. E-mail: tobias.schmiedel@geo.uio.no; olivier.galland@geo.uio.no.

[2]University of Oslo, Centre for Earth Evolution and Dynamics (CEED), Department of Geosciences, Oslo, Norway. E-mail: sigurd.kjoberg@geo.uio.no.

[3]University of Oslo, Centre for Earth Evolution and Dynamics (CEED), Department of Geosciences, Oslo, Norway and Volcanic Basin Petroleum Research AS (VBPR), Oslo, Norway. E-mail: planke@vbpr.no.

[4]Imperial College London, Basins Research Group, Department of Earth Science and Engineering, London, UK. E-mail: c.magee@imperial.ac.uk; c.jackson@imperial.ac.uk.

[5]University of Aberdeen, Department of Geology and Petroleum Geology, School of Geosciences, Aberdeen, UK. E-mail: n.schofield@abdn.ac.uk.

[6]University of Oslo, Centre for Earth Evolution and Dynamics (CEED), Department of Geosciences, Oslo, Norway and DougalEARTH Ltd., Solihull, UK. E-mail: dougal@dougalearth.com.

overlying dome structures that can be described as four-way dip closures (Hansen and Cartwright, 2006; Jackson et al., 2013; Magee et al., 2014, 2015), and (3) promote the development of local intense fracture networks that locally increase host rock permeability (Witte et al., 2012; Agirrezabala, 2015; Senger et al., 2015). A robust understanding of the mechanics of magma emplacement in volcanic basins is therefore required to derisk hydrocarbon exploration in volcanic basins (Potter and Konnerup-Madsen, 2003; Schutter, 2003a, 2003b).

In this study, we focus on the mechanisms that control the growth of domes, often called forced folds (e.g., Stearns, 1978; Magee et al., 2013), associated with igneous sills. These domes can represent structural traps (i.e., four-way dip closures) or create and deform stratigraphic traps (e.g., onlap of reservoir rocks and deflection of channels influencing the distribution of reservoir rocks for hydrocarbons; Schutter, 2003a; Delpino et al., 2014). In recent years, distinct mechanisms controlling the formation of sill-associated doming have been proposed. The most common mechanism involves synemplacement uplift accommodating sill intrusion (e.g., Pollard and Johnson, 1973; Roman-Berdiel et al., 1995; Malthe-Sørenssen et al., 2004; Hansen and Cartwright, 2006; Kavanagh et al., 2006; Menand, 2008; Bunger and Cruden, 2011; Galerne et al., 2011; Galland, 2012; Galland et al., 2014, 2015). These models typically assume that uplift occurs via elastic bending, and sometimes failure, of the overburden, causing forced folding and fracturing due to the intrusion. However, field observations, seismic studies, and recent 3D laboratory models show that substantial synemplacement inelastic (elastoplastic) deformation, such as local compaction and fluidization, can also affect the growth of these domes (e.g., Cosgrove and Hillier, 1999; Hansen and Cartwright, 2006; Schofield et al., 2010, 2012a, 2014; Magee et al., 2013). In addition to the synemplacement mechanisms, seismic data indicate that postemplacement differential compaction may also play a role in forming or modifying dome structures above sills (e.g., Einsele et al., 1980; Cosgrove and Hillier, 1999; Hansen and Cartwright, 2006; Agirrezabala, 2015).

However, the extent to which the interplay between syn- and postemplacement mechanisms controls the final shape and structure of domes associated with igneous intrusions remains poorly constrained. This uncertainty typically emanates from the methods applied to study these systems. For example, structural field observations can provide small, detailed snapshots of dome structures overlying intrusions and associated fault and fracture systems, but they cannot provide a complete spatial understanding due to incomplete outcropping conditions (e.g., Henry Mts; Wilson et al., 2016). The 2D seismic reflection profiles are also too incomplete to fully describe complex 3D structures (e.g., Planke et al., 2000; Berndt et al., 2001; Jackson et al., 2013; Zhao et al., 2014). Therefore, high-quality 3D seismic data are essential to study intrusion-induced over-

burden deformation in 3D (Bell and Butcher, 2002; Smallwood and Maresh, 2002; Trude et al., 2003; Polteau et al., 2008; Magee et al., 2015; Planke et al., 2015). In this paper, we show how the detailed analysis of high-quality 3D seismic data can be used to test and constrain the relevance of mechanical models of dome growth accommodating the emplacement of igneous sills. We highlight the contribution of syn- and postemplacement mechanisms of overburden deformation by using detailed mapped horizons from 3D seismic reflections, thickness maps, and the application of various seismic attributes.

Mechanisms of overburden deformation

A range of different models derived from field observations and seismic imaging have been proposed to explain overburden deformation above sills, particularly dome-shaped structures.

Synemplacement processes

Classic models of doming involve overburden uplift in response to elastic bending above an intruding sill or laccolith (Figure 1a) (Gilbert, 1877; Pollard and Johnson, 1973; Dixon and Simpson, 1987; Goulty and Schofield, 2008; Bunger and Cruden, 2011; Galland and Scheibert, 2013). In these models, doming occurs during the sill emplacement, and the dome geometry is directly controlled by that of the underlying intrusion (e.g., Gilbert, 1877; Pollard and Johnson, 1973; Corry, 1988; Goulty and Schofield, 2008; Galland and Scheibert, 2013). Therefore, the dome amplitude f equals the sill thickness t (Figure 1a) (Pollard and Johnson, 1973; Dixon and Simpson, 1987; Goulty and Schofield, 2008; Bunger and Cruden, 2011; Galland and Scheibert, 2013); f and t can be used as a proxy for the volume of the dome and intrusion, respectively. This active doming is often referred to as forced folding (e.g., du Toit, 1920; Stearns, 1978; Trude et al., 2003). Forced folding typically produces a positive topographic structure at the contemporaneous surface, such that sediments deposited during sill emplacement will onlap onto the topographic or bathymetric high (e.g., Trude et al., 2003; Schofield et al., 2015; Magee et al., 2016). The observation of these onlap features in seismic data provides a method of dating the intrusion emplacement if sufficient borehole data are available to constrain the age of sedimentary horizons (Trude et al., 2003).

Elastic bending produces complex stress distributions in the overburden, resulting in outer-arc stretching and inner-arc compression (Timoshenko and Woinowsky-Krieger, 1959; Ramsay, 1967; Pollard and Johnson, 1973). This outer-arc stretching can lead to thinning of the uppermost layers of the dome (Ramsay, 1967). When the stresses generated in response to elastic bending exceed the strength of the overburden rocks, failure occurs and characteristic fracture patterns develop. These fracture pattern can be classified into four main types depending on their location in the overburden (Figure 1b): (1) circumferential, tensile fractures at the surface coincident with the area of the largest convex

curvature above the sill edges (e.g., Pollard and Johnson, 1973; Bunger and Cruden, 2011; Galland et al., 2016), (2) radial tensile fractures (mode I) and/or normal faults (mode II) due to an extensional regime (i.e., outer-arc stretching) in the central part of the dome structure (Hansen and Cartwright, 2006; Magee et al., 2013; Galland et al., 2016), (3) dilational fractures near the peripheral hinge of the dome, close to the intrusion tips, which progress toward the surface (Pollard and Johnson, 1973; Menand, 2008; Thomson and Schofield, 2008; Galland and Scheibert, 2013; Agirrezabala, 2015), and (4) shear fractures resulting from differential uplift at the dome edge (de Saint-Blanquat et al., 2006; Hansen and Cartwright, 2006; Wilson et al., 2016).

Although elastic bending promotes roof uplift, other mechanisms can affect the overall geometry of the dome structure above the intrusion. For example, pore fluid expulsion within the thermal and/or structural aureole of the intrusion can lead to a significant volume reduction of the host rock (Figure 1c) (Einsele et al., 1980; Morgan et al., 2008; Schofield et al., 2010, 2012a, 2014; Jackson et al., 2013; Magee et al., 2013). This volume reduction resulting from a decreased porosity reduces the effect of active mechanical doming due to the emplacement of the intrusion. Therefore, the amplitude of the dome f is expected to be less than the sill thickness t, implying that the overlying host rock succession thins across the sill (Figure 1c).

Postemplacement process

Variations in the load of postemplacement sedimentation can induce a variable subsidence of the overburden due to differential compaction (Figure 1d) (e.g., Cosgrove and Hillier, 1999; Hansen and Cartwright, 2006). In particular, following sill intrusion, the load due to postemplacement sedimentation triggers compaction of the underlying rocks. Because intrusions are virtually incompressible with respect to the surrounding sedimentary rocks, and therefore do not compact, a dome structure may develop (Figure 1d) (e.g., Cosgrove and Hillier, 1999; Hansen and Cartwright, 2006). In addition to generating new folds, this differential compaction process can enhance the amplitude f of a preexisting dome due to the emplacement of the intrusion, such that f becomes larger than the sill thickness t (Figure 1d); i.e., the domed sequence is also expected to be thicker above the sill than outside the sill (Figure 1d).

To summarize, these models of syn- and postintrusion emplacement mechanisms are associated with distinct characteristic structures and features. To test the relevance of each model, we will test the occurrence, or not, of these structures and features in the Tulipan prospect case study, Møre Basin, mid-Norwegian continental margin.

Geologic framework

Over the past three decades, massive sill complexes with an extent of at least 80,000 km^2 have been imaged in the Møre and Vøring Basins, offshore Norway by 2D and 3D seismic reflection data (e.g., Berndt et al., 2001; Planke et al., 2005). Positioned on the mid-Norwegian margin, the Møre Basin represents an example of a rifted volcanic margin (Planke et al., 2005; Abdelmalak et al., 2015). The outline of the Møre Basin is defined by the base unconformity of the up to 6 km thick Cretaceous sedimentary basin infill (Figure 2a) (Brekke, 2000; Faleide et al., 2010). The development of the basin occurred during Late Jurassic-Early Cretaceous rifting of the Norwegian continental margin (Brekke, 2000). Late Paleocene-Early Eocene rifting associated with the opening of the North Atlantic led to the emplacement of a significant volume of igneous material (e.g., Abdelmalak et al., 2015); including the emplacement of the Tulipan saucer-shaped sill, which forms the focus of this study. The intrusion hosting sedimentary infill is composed of mainly claystone, with interbedded sand-
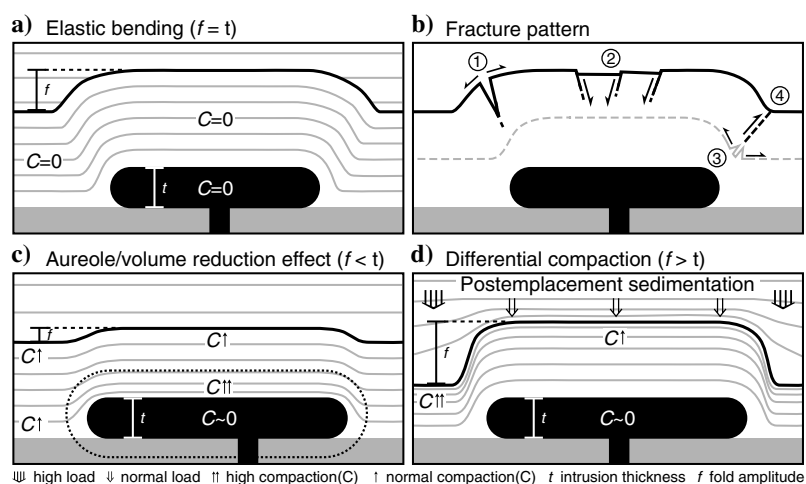

Figure 1. Schematic diagrams showing mechanisms of overburden deformation associated with intrusion emplacement. (a) The simple elastic model envisages the formation of a dome structure (forced fold) above an intrusion (e.g., Pollard and Johnson, 1973; Galland and Scheibert, 2013). (b) Four fracture types related to elastic overburden deformation: (1) circumferential, tensile fractures coincident with the area of the largest convex curvature of the dome (e.g., Pollard and Johnson, 1973; Bunger and Cruden, 2011; Galland et al., 2016), (2) radial tensile fractures (mode I) and/or normal faults (mode II) due to outer-arc stretching (Hansen and Cartwright, 2006; Magee et al., 2013; Galland et al., 2016), (3) dilational fractures progressing toward the surface (Pollard and Johnson, 1973; Menand, 2008; Thomson and Schofield, 2008; Galland and Scheibert, 2013; Agirrezabala, 2015), and (4) shear fractures resulting from differential uplift (de Saint-Blanquat et al., 2006; Hansen and Cartwright, 2006; Wilson et al., 2016). (c) Model of volume reduction, i.e., porosity decrease, affected by the aureole of the intrusion (e.g., Hansen and Cartwright, 2006; Jackson et al., 2013). (d) Differential compaction model envisages the formation and/or enhancement of a dome structure associated with an intrusion under the load of postemplacement sedimentation (e.g., Cosgrove and Hillier, 1999; Hansen and Cartwright, 2006).

stone and sporadic carbonate intercalations (e.g., Dalland et al., 1988; Berndt et al., 2001; Planke et al., 2005).

The oldest stratigraphic unit in the area of interest is the Late Cretaceous Springar Formation, which consists mainly of claystone with carbonate intercalations. The uppermost sequence of the Springar Formation contains a prominent carbonate-cemented layer that corresponds to the lowermost horizon interpreted in this study (Figure 3). The base of this carbonate layer, subsequently referred to as Base Carbonate, corresponds to a high-amplitude positive reflection on the seismic data (Figures 3, 4, and 5). Other horizons interpreted in this study include the Top Danian and HV4 (HV nomenclature adopted from Kjoberg et al., 2017), which are both contained in the Early Paleogene Tang Formation (Figure 3). The lower Tang Formation (Top Danian to Base Carbonate) is composed of a sandstone succession, which proved to be a reservoir rock in the Tulipan prospect, as highlighted by a gas discovery well (6302/6-1; Figure 2). The rest of the Tang Formation consists of dark gray claystone successions (Figure 3) (Dalland et al., 1988). New highly resolved biostratigraphic results from Kjoberg et al. (2017) highlight the uncertainty of the HV3 and HV1 regarding their affiliation to the Tang or Tare Formation (Figure 3). Above the Tang Formation, we interpreted the top of the Eocene Tare Formation (Top Tare; Figure 3) and the top of the Neogene Kai Formation (Top Kai; Figure 3). The complete stratigraphic description of the Tulipan prospect can be found in Kjoberg et al. (2017). The area of interest is located beyond the eastern limit of Paleogene basalts that cover the northwestern border of the Møre Basin (Figure 2) (e.g., Brekke, 2000; Berndt et al., 2001).

Data and methods

This study uses a full-stack, time-migrated, zero-phase 3D seismic data set (Statoil 3D cube ST0105) that was processed in 2001 and covers the Tulipan prospect in the western part of the Møre Basin (Figure 2). The complete 3D survey covers an area of 1610 km², has a line spacing of 12.5 m, and was recorded to a depth of 7 s two-way traveltime (TWT). We focus on the northern approximately 450 km² of the seismic cube containing the well 6302/6-1 (Figure 2). The 3D seismic data are displayed with a reverse polarity (i.e., a downward increase in acoustic impedance correlates to negative or blue reflections). In the time interval of interest (4.6–4.8 s TWT), the seismic data have a dominant frequency of 15–20 Hz. The range for the thickness of the sill was calculated using the dominant frequency in the area of the sill intrusion (15 Hz) and velocity V_P 5500 m/s, with an assumed error of ±10% (Planke et al., 2005; Jackson et al., 2013; Magee et al., 2015). This suggests that sills with thicknesses below the resolution limit of $\lambda/4$ (approximately 92 m ± 10%) will appear as tuned reflection packages, whereas those below the detection limit $\lambda/30$ (approximately 12 m ± 10%) will not be identified (Planke et al., 2005; Jackson et al., 2013).

Data from borehole 6302/6-1 were used to constrain the lithology, geophysical properties, and age of the strata in the interval of interest (see also Kjoberg et al., 2017). The well extends to a depth of 4234 m (below rotary kelly bushing), a total length of 15.7 m was cored between 3903 and 3942 m in the Danian sandstones (Tang Formation), and cutting samples were taken in the interval of 1975–4230 m. Conventional borehole wireline logs and a check-shot vertical seismic profile (VSP) time-depth curve, in combination with the core/cutting samples, were used to develop a simple layered velocity model based on the interval velocities $V_{P_{int}}$ to convert the key horizons from time to depth (Figure 3). The continuity of the reflection strength and their (sub-) horizontal appearance in our 3D seismic data show little evidence of lateral variations in the geology that would produce velocity anomalies. Therefore, we consider the effects of horizontal velocity variations in the data to be minimal in the study area, and we use the velocity model constrained from the well data as the basis for this study (Figure 3). This information combined with the 3D seismic data were used to interpret five key horizons (5–15 line interval inline/crossline) in the sedimentary strata above the intrusion (Figures 3 and 4). The 3D volume visualization techniques (e.g., opacity rendering; Supplemental Figures 1, 2, and 3 can be accessed through the following links: s1.eps, s2.eps, and s3.eps) and different surface and volume attributes (e.g., root-mean-square amplitude, coherence, and spectral decomposition) were used to extract additional characteristics of the interpreted reflections in the sedimentary overburden of the Tulipan sill (Planke et al., 2015).
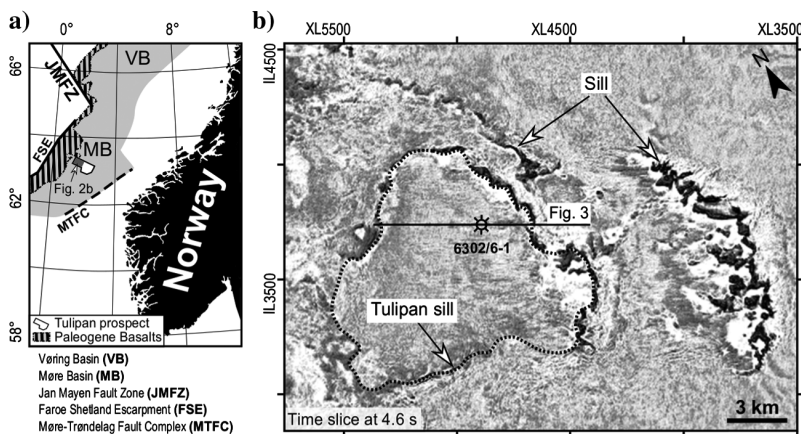

Figure 2. Location maps. (a) Position of the 3D seismic survey containing the Tulipan prospect in the Møre Basin on the Norwegian continental shelf with respect to the Norwegian mainland. Outline of the Paleogene basalts after Berndt et al. (2001). (b) Seismic reflection time slice showing the main igneous complexes identified in the study area. The Tulipan sill is indicated (dashed line) in addition to the location of well 6302/6-1.

The interpretation of sills in the seismic data was performed according to their reflection properties, with laterally discontinuous, strata-discordant, high-amplitude anomalies considered to represent intrusions (Smallwood and Maresh, 2002; Polteau et al., 2008; Thomson and Schofield, 2008; Jackson et al., 2013; Magee et al., 2014; Planke et al., 2015). At the location of the Tulipan sill, constrained by Polteau et al. (2008), the seismic data display a high-amplitude reflection (Figures 5 and 4). We define the top of the Tulipan sill as
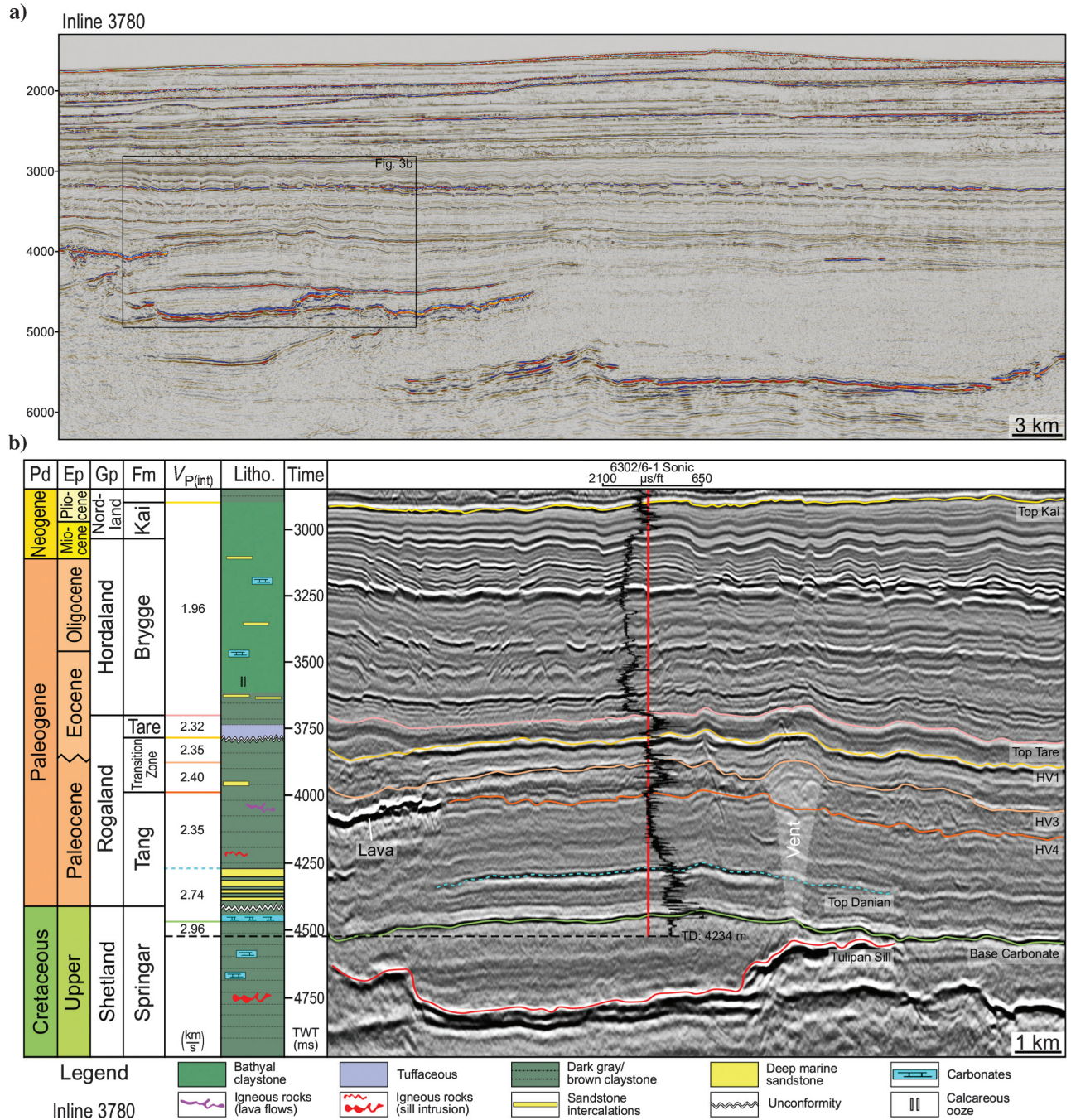
Figure 3. (a) Example of a representative northwest−southeast seismic section. (b) Simplified stratigraphic column of the study area with the principal lithologies encountered in well 6302/6-1. The period (Pd), epoch (Ep), group (Gp), and formation (Fm) are based on the biostratigraphy from cutting samples of well 6302/6-1 (e.g., Kjoberg et al., 2017). Interval velocities $V_{P(int)}$ used in the study derived from the VSP checkshot data. The lithologic column (litho) is based on that of, and described in detail in, Kjoberg et al. (2017). The lithology below the total depth (TD) of the well is an extrapolation.

the uppermost trough of this reflection package (Figures 5 and 4). We interpreted the top of the sill using guided 2D autotracking, with two-line interval inline/crossline spacing. The subsequent deeper peak reflection (Figure 5) was roughly picked (16 line interval inline/crossline) as an estimate for the base of the Tulipan sill.

Results

Structure of the sill

Figure 4 shows the 3D expression of the picked high-amplitude reflection of the top Tulipan sill, which consists of (1) a flat, strata-concordant inner base with an approximately 10–12 km diameter and (2) flanking in-clined outer sheets that transgress upward and outward (approximately 200–400 ms TWT). Thus, the Tulipan sill displays a typical saucer-shaped geometry. The inclined sheets are laterally segmented radially, with the vertical offset between the segments increasing toward the outer rim (Figure 4).

The base of the Tulipan sill was not clearly observable in the tuned reflection package. The picked base shows lateral thickening of the reflection associated with a reduction in amplitude strength and the interruption of the continuous reflection in the central part of the sill (Figures 5 and 4b). However, because we cannot clearly separate the two reflections for the top and the bottom of the sill, we can only consider the sill thick-

	Seismic reflection	Seismic sequences (above/below)
	HV1 - Continuous - Strong amplitude reflection - Trough (positive acoustic impedance) *(Arrows indicate the downlap structures)*	*Above* Continuous succession of low to intermediate amplitude reflections and downlap patterns above the interpreted vents *Below* (Sub-)horizontal low to intermediate amplitudes, with continious negative reflections and segmented, positive reflections
	HV3 - Prominent positive amplitude reflection - Discontinuous - General character bedding parallel (small scale - hummocky reflection) - Peak (negative acoustic impedance)	*Above* Succession of continious negative low to intermediate amplitude reflections and positive, low amplitude reflections (segmented) *Below* Complex seismic character with generally low amplitude reflections
	HV4 - Segmented (tilted, with offset) - Intermediate (to low) amplitude reflection - Peak (negative acoustic impedance)	*Above* Continuous, partly hummocky succession of low to intermediate amplitude reflections *Below* Weak to intermediate amplitudes with an overall complex and diffuse character (segmented reflections)
	Top Danian - Distinct spatial distribution - High amplitude reflection (top gas reservoir) - Peak (negative acoustic impedance) - Bedding parallel	*Above* Succession of weak seismic reflections, that are parallel and mainly continuous *Below* Same as above, but slightly higher amplitudes (probaly due to higher contrast in acoustic impedance induced by the hydrocarbons)
	Base Carbonate - Continuous, unless where truncated from below - Very high positive amplitude reflection - Peak (negative acoustic impedance) - Bedding parallel	*Above* A continuous, wide, negative low to intermediate amplitude reflection with a parallel character *Below* Continuous, wide, negative low amplitude reflection; more prominent parallel seismic character of narrow, alternating reflections toward the depth
	Tulipan Sill (Top and Base) - Continuous - Very high amplitude reflection - Top - trough (positive acoustic impedance) - Base - peak (negative acoustic impedance) - Bedding parallel and bedding truncation	*Above* Stack of alternating, weak, parallel seismic reflections *Below* Succession of very strong alternating reflections; pinching out of stack-central reflections; after approximately 0.3 s sudden change to low amplitude reflections

Figure 4. Seismic stratigraphic framework, including a description of the mapped seismic reflections and the seismic sequences they define.

ness to be between the limit of detection (i.e., 12 m $\pm$ 10%) and resolution (i.e., 92 m $\pm$ 10%). This estimate is in agreement with observations of other sills in the Møre and Vøring Basins (e.g., Berndt et al., 2000), as well as those found in outcrop analogs (Eide et al., 2016; Jerram and Bryan, 2017). Using this estimate of thickness and the aerial distribution of the Tulipan sill, its volume is between 1.4 and 13.2 km^3. This volume is in the same order as historic flood basalt eruptions; e.g., the Laki eruption with a volume of 14 km^3 is one of the largest volume modern eruptions (Bryan et al., 2010).

Structure of the overburden
Time-structure maps

In this study, five key horizons were interpreted in the sedimentary overburden (Figure 5). From the top to the bottom, these are (1) HV1, which describes the top of the deformed overburden locally downlapped by overlying reflections, (2) HV3, a prominent reflection above lavas in the Tang Formation, (3) HV4, a stratigraphic surface that displays a prominent polygonal fault pattern, (4) the Top Danian, which corresponds to the top of the sandstone unit representing the reservoir rock in the area, and (5) the Base Carbonate, a prominent Mesozoic carbonate layer (in the Late Springar Formation; Figures 3 and 5).

HV1 shows a central dome structure that correlates with the periphery of the underlying Tulipan sill (Figure 6a). The maximum amplitude f of this dome structure was calculated, using a best-fitting plane for the estimation of the dome base, to be approximately $f \approx 50 \pm 20$ m (Figure 6b) from the depth-converted time-structure map. Figure 6a shows four additional dome structures surrounding the central dome: (1) one overprinting the outline of the central dome in the northwest and (2) three separate ones in the south and east. A north–south-trending depression separates these three domes from the large central dome above the Tulipan. The underlying time-structure maps of the HV3, HV4, Danian, and Base Carbonate horizons similarly display a large central dome as in HV1 (Figure 6c; Supplemental Figures 1, 2, and 3 can be accessed through the following links: s1.eps, s2.eps, and s3.eps). Note that for the HV3, Top Danian, and Base Carbonate, the data coverage is limited, such that the smaller peripheral domes are not imaged. In addition, the time-structure maps of the different horizons show that the well 6302/6-1 was drilled in the crest of the dome above the Tulipan sill.

Spectral decomposition attribute maps on sedimentary horizons

Spectral decomposition attribute maps were produced on the interpreted horizons in the sedimentary overburden to visualize possible host rock deformations (Figure 7; e.g., fractures, faults, etc.) as well as changes in the lithology.

The attribute map of the uppermost interpreted horizon, HV1, shows 19 dark, subcircular features (white circles; Figure 7a), i.e., structures associated with hydrothermal vent complexes that overlie the lateral termination of the underlying Tulipan sill (e.g., Planke et al., 2005; Berndt et al., 2016). These features correspond to the hydrothermal vent structures mapped by Kjoberg et al. (2017). In plan view on the attribute map, most of these vents can be seen to be connected by thin, linear features (Figure 7a). Similar circular and linear features were observed on HV3 (dashed yellow line; Figure 7b), but they were too faint to be confidently described. A possible spatial correlation of those linear features between the different horizon maps cannot be documented with confidence (Figure 7a and 7b).
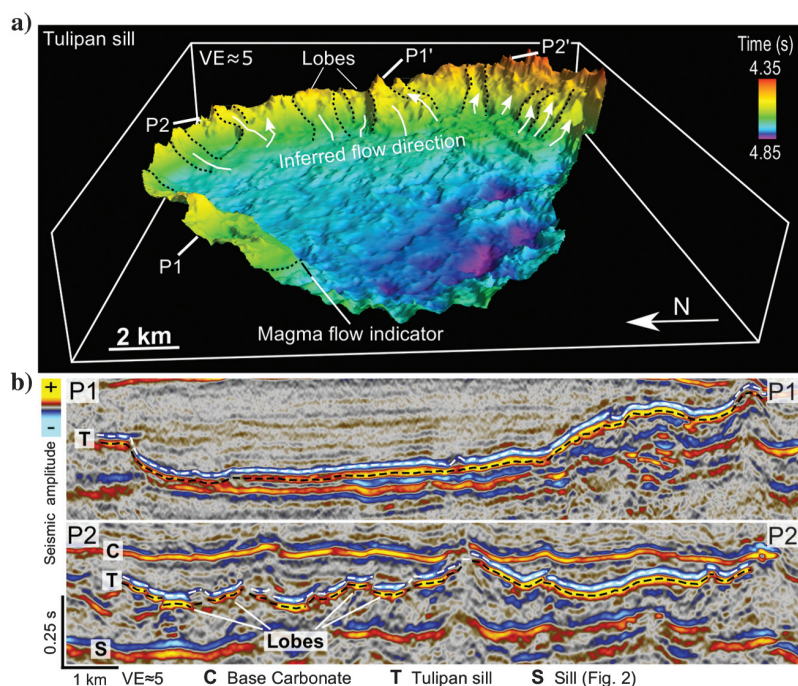
Figure 5. Seismic expression of the Tulipan sill. (a) The 3D visualization of the saucer-shaped geometry of the top Tulipan sill horizon. Radial magma flow indicators mark edges of reflection segments representing upward, outward transgressing, igneous inclined sheets (Schofield et al., 2012b; Magee et al., 2014), examples of these are highlighted as lobes and cross referenced to profile P2-P2′ in (b). (b) Seismic profiles show the cross-sectional expressions of the Tulipan sill (see [a] for the location). P1-P1′ highlights the picked Tulipan sill top and base, whereas P2-P2′ visualizes the segmented character of the Tulipan sill reflection and indicates an underlying sill (S) below the Tulipan sill (Tulipan top — dashed white line; dashed black line tentatively interpreted as the sill base; lobes highlighted in [a] are also indicated).
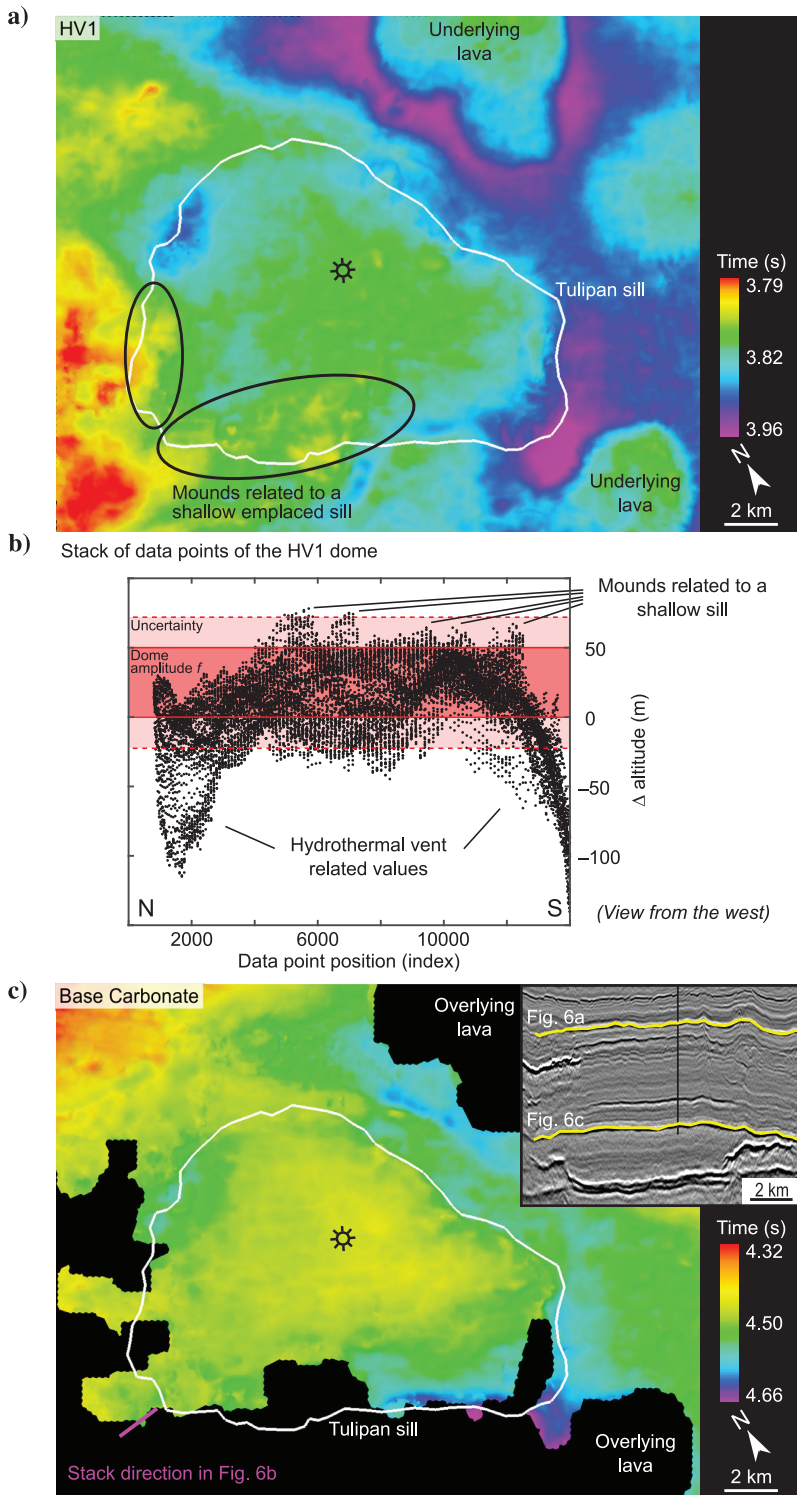
Figure 6. Time-structure maps (TWT) and dome amplitude f. (a) The HV1 time-structure map shows the paleo-surface and top of the domed overburden during the emplacement of the Tulipan sill. (b) The stack of altitude data points within the Tulipan periphery highlights the plateau in the domed overburden. A best-fit plane was used to estimate the base of the dome and calculate the amplitude f (red area). (c) Base carbonate time-structure map of the lowermost interpreted horizon above the Tulipan sill shows a good confined dome structure inside the Tulipan sill periphery. Subset shows the stratigraphic location of (a and c).

On the HV3 map (Figure 7b), dark circular features similar to, and at the same locations as those observed in the HV4 map (black ovals; Figure 7c), are present. Note, however, that they are overall larger. They are mainly located along the edge of Tulipan sill, and they correspond to vertical zones characterized by complex and weak seismic reflections crosscutting the horizon (Figure 3). Such features are characteristic of hydrothermal vent complexes (e.g., Svensen et al., 2004; Planke et al., 2005), and they correlate to those identified by Kjoberg et al. (2017). Inside the Tulipan sill periphery, two separate areas can be distinguished: (1) a southern area (dashed yellow line; Figure 7b), which displays dark colors and a complex but faint occurrence of circular features and linear features, and (2) a northern area characterized by bright colors with no observable features (Figure 7b). Outside the Tulipan sill periphery, two comprehensive dark areas in the northwest and northeast are visible (Figure 7b). We interpret these latter as the extruded Paleogene basalts (Berndt et al., 2001) according to their seismic character (Figures 2 and 3), the emplacement of which was not related to the emplacement of the Tulipan sill and associated doming. Therefore, we will not consider them in the following sections.

The HV4 map highlights an overall coverage with linear features (Figure 7c), which correlate with discontinuities in the seismic reflection data (Figure 5). This polygonal pattern does not display a change in its characteristics inside or outside of the Tulipan periphery (Figure 7c). Other observable features are the dark circular patches with diameters up to approximately 1 km (e.g., black circles; Figure 7c).

The Top Danian horizon attribute map has a very limited spatial distribution inside the periphery of the Tulipan sill (Figures 3 and 7d). The central part of the horizon map is represented by an area of significantly bright colors, again highlighting lateral variations in rock properties (Figure 7d). No significant feature is visible.

The Base Carbonate horizon (Figure 7e) images the lowermost interpreted reflection in the sedimentary sequence above the Tulipan sill (Figure 3). The
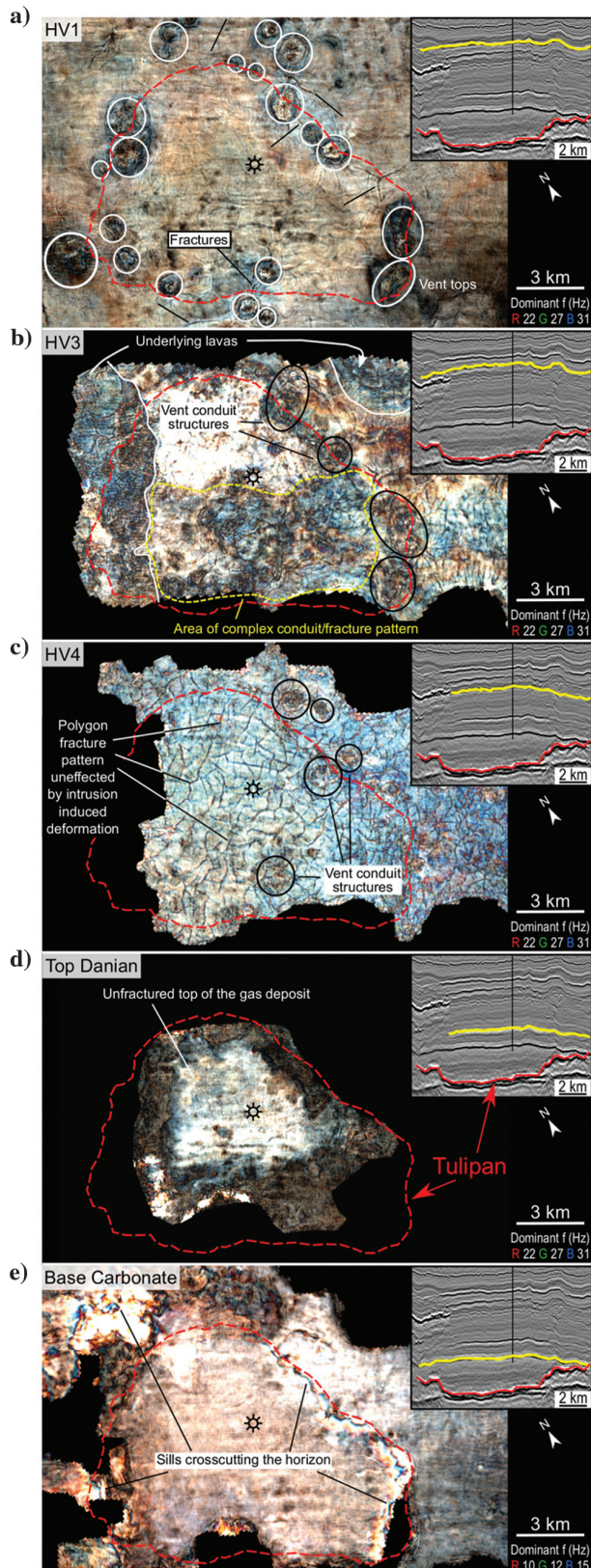
Figure 7. Spectral decomposition attributes maps of key horizons. Subsets display the same seismic section of Figure 3 (for the location, see Figure 2). The periphery of the Tulipan sill (dashed red line) corresponds to the map contour at the level of approximately 4400 ms (TWT). (a) HV1 (Top Tang Formation) defines the top of the dome structure, and it highlights hydrothermal vent complexes (HTVCs, white circles) and fractures in between (black/white arrows). (b) The HTVCs on HV3 are obscured by the lava flow pattern (outside the white lines). (c) HV4 envisages a regional polygonal fault system, and deeper parts of the HTVCs (black circles) identified in (a). (d) Top Danian shows no fractures in the top of the reservoir sandstones of the Tulipan prospect. (e) The Base Carbonate shows no evidence for central fractures, but highlights the crosscut of the underlying Tulipan sill (the crosscut itself is not visible in the seismic subset).

spectral decomposition map shows a distinct dark line-feature corresponding to the crossing of the Tulipan sill though the horizon (Figure 7e). No other prominent feature is visible. Within the Tulipan sill periphery and adjacent to it, an overall bright color scheme is observed, highlighting lateral variations in rock properties.

Isochron maps

Isochron maps between different horizons were produced to quantify lateral thickness variations of the intervals through the dome above the Tulipan sill (Figures 3 and 8). This information is crucial for testing the different models listed in Figure 1. The 3D seismic data of the Tulipan prospect image a regional thickening of the sedimentary strata toward the west-northwest (Figure 8).

The isochron map of the postemplaced sediments (Top Kai-HV1) in Figure 8a shows that the thickness of younger sediments outside of the Tulipan periphery is larger compared with above the Tulipan sill.

Figure 8b displays the isochron map of an interval (Top Tare-HV1). The interpretation of the Top Tare horizon used to produce this isochron map originates from the work of Kjoberg et al. (2017). This interval shows distinct, thick circular mound structures that typically overlie the periphery of the underlying Tulipan sill at the same location as the hydrothermal vent complexes observed before (Figure 7a–7c). The Top Tare-HV1 interval displays a thinning within the Tulipan periphery compared with the areas in the close vicinity of the underlying sill outline. In addition, we observe fracture pattern between the mound structures and in the surrounding of the sill (Figure 8b) coinciding with the dark linear features observed in Figure 7a.

The HV1-Base Carbonate interval, i.e., the overall sequence analyzed in this study shows a relatively constant thickness, except for localized thinner areas that are parallel to the outline of the underlying sill (Figure 8c). These areas are likely related to hydrothermal vent complexes. However, each subinterval displays more complex patterns.

The preemplacement shallower HV1-HV4 interval exhibits a ring feature, aligned along the periphery of the underlying sill, which presents local subcircular areas with the greatest thickness (Figure 8d). The spatial positions of these local thick areas correspond to the observed dark circular patches in the spectral decomposition attribute maps (Figure 7). These features are likely related to hydrothermal vent complexes (Kjoberg et al., 2017). The thickness of this interval is similar at the center of the underlying sill and outside the sill (Figure 8d).

In contrast to the HV1-HV4 interval, the deeper HV4-Base Carbonate interval exhibits a thickening constrained inside the outline of the Tulipan sill (Figure 8e). Note the prominent thin elongated features parallel to the periphery of the Tulipan sill. These features are not visible on the HV1-HV4 interval (Figure 8d), but they affect the whole studied interval, i.e., HV1-Base Carbonate (Figure 8c). Similarly to the HV4-Base Carbonate interval, the Top Danian-Base Carbonate subinterval also

exhibits a thickening (Supplemental Figures 1, 2, and 3 can be accessed through the following links: s1.eps, s2.eps, and s3.eps). The location of this thickening roughly correlates with that of the observed bright colors of the Top Danian spectral decomposition map (Figure 7d).

Interpretation
Sill structure and relation with dome

Our 3D reconstruction of the top Tulipan sill exhibits a characteristic saucer shape, with a flat inner sill, which connects to transgressive inclined sheets ("lobes") that radially increase in vertical offsets (Figure 4). Such a structure is in good agreement with the two-stage model of shallow magma emplacement, whereby an initial flat sill intrudes along a stratigraphic weakness followed by an upward, outward transgressive emplacement of inclined sheets (e.g., Malthe-Sørenssen et al., 2004; Hansen and Cartwright, 2006; Polteau et al., 2008; Thomson and Schofield, 2008; Galland, 2012). The radial offsets visible along the inclined sheets are interpreted as radial flow indicators, i.e., intrusive step and bridge structures indicating upward and outward magma flow during the emplacement into a brittle host rock (e.g., Thomson and Schofield, 2008; Hutton, 2009; Schofield et al., 2010; Magee et al., 2016), also in agreement with the two-stage model of saucer-shaped sill emplacement.

The Tulipan sill exhibits an overall spatial correlation with the overlying dome structure (Figure 6). The well data do not evidence any other sill emplaced in the sill overburden. The seismic data only display a small, shallower sill in the western edge of the dome, resulting only in a local, shallow positive topographic feature (Figure 6; Supplemental Figures 1, 2, and 3 can be accessed through the following links: s1.eps, s2.eps, and s3.eps). Thus, we conclude that the dome displayed in our data is solely related to the underlying Tulipan sill.

The HV1 horizon has been identified as being the paleo-surface at the time of emplacement of the Tulipan sill, based on the detailed interpretation of downlap observed in the 3D seismic associated with the top of the hydrothermal vent complexes related to the edges of the Tulipan sill (Kjoberg et al., 2017). This implies that the Tulipan sill was emplaced between 55.8 and 54.9 Ma (Kjoberg et al., 2017), consistent with the age of the North Atlantic Large Igneous Province emplaced at the Paleocene-Eocene transition (Berndt et al., 2001; Svensen et al., 2004; Faleide et al., 2010). Thus, the depth of emplacement is estimated to be not deeper than 1.5–2 km. The saucer-shaped geometry of the Tulipan sill is a consequence of such a shallow emplacement depth (e.g., Planke et al., 2005; Galland et al., 2009; Eide et al., 2016). This corroborates the observation of other studies (e.g., Hansen et al., 2011; Magee et al., 2014; Eide et al., 2016) and modeling (Galland et al., 2009), in which sills show a more planar geometry with increasing depth of emplacement.
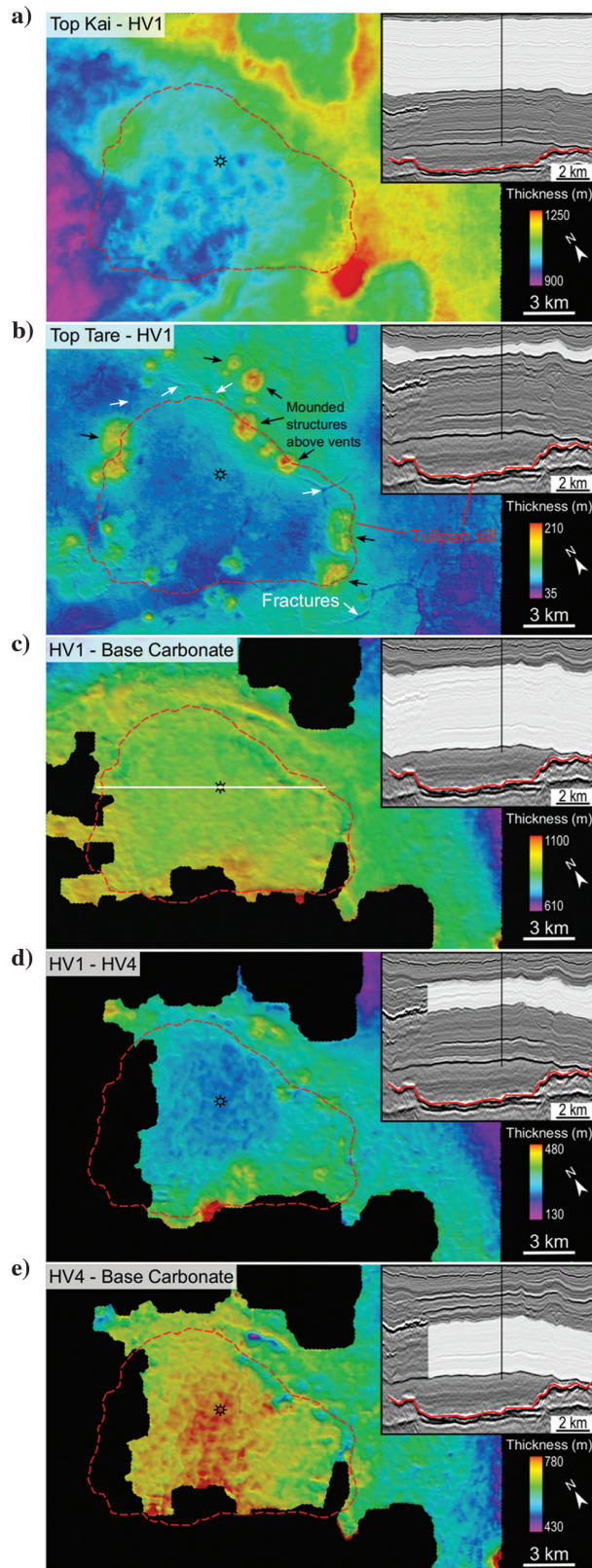
Figure 8. Thickness maps of the sedimentary sequences above the Tulipan sill. (a) Top Kai-HV1 displays the thinner postemplacement sediments above the Tulipan sill compared with the area outside of the Tulipan periphery, resulting from differential compaction. The thin, anomaly in the northwest is caused by several underlying igneous intrusions and the Paleogene Basalts. (b) Top Tare-HV1 isochron map shows the thickness anomalies (i.e., hydrothermal vent complex-related mounds) in sedimentary strata right above the dome structure. (c) Isochron map of the complete strata interpreted (HV1-Base Carbonate). The white line shows the position of the seismic subset. (d) The upper dome structure, i.e., the HV1-HV4 isochron map, shows patchy thickness anomalies (thicker) in the close vicinity of the Tulipan sill periphery, whereas the central area is thin. (e) Isochron map of HV4 to Base Carbonate displays a contrasting thickness variation compared with (d) within the Tulipan sill periphery.

Dome growth mechanisms

Our detailed analyses of the borehole and 3D seismic data allow us to test the relevance of the distinct mechanisms of dome growth above igneous sills. Our results highlight the occurrence of post- and synemplacement processes.

Postemplacement differential compaction

The isochron map of Figure 8a shows that the post-emplacement sediments in the Top Kai-HV1 interval are thinner above the Tulipan sill than outside the sill. Post-emplacement sediments typically show this greater thickness outside the intrusion periphery than inside when a magmatic intrusion causes folding of the overburden and differential compaction occurs in the sediments above (Hansen and Cartwright, 2006; Jackson et al., 2013). We interpret the occurrence of thicker post-emplacement sediments solely on the southeastern side of the Tulipan sill as being related to the other strong reflection events in the 3D seismic data, i.e., sills and Paleogene basalts (Figures 2, 3, 7, and 8). In addition, isochron maps of Figure 8c and 8e, i.e., the HV1-Base Carbonate interval and the HV4-Base Carbonate subinterval, display similar trends. This thickening is in good agreement with the differential compaction mechanism (Figure 1d). Thus, we conclude that differential compaction must have, at least partly, contributed to the formation of the dome structure above the Tulipan sill. Thus, a key question is whether parts of the dome have resulted from synemplacement mechanisms or not.

Synemplacement mechanisms

The direct evidence of synemplacement mechanisms of dome growth above the Tulipan sill is limited. We observe fracture patterns located in the vicinity of, and parallel to, the Tulipan sill periphery and dome edge, affecting the paleo-surface horizon HV1 (Figures 7 and 8a). These surficial peripheral concentric tensile/extensional fractures are in good agreement with the laboratory experiments of dome growth of Galland (2012). These experiments show that when a dome associated with an intruding saucer-shaped sill exhibits a plateau shape, like that of the Tulipan dome, the largest convex curvature of the paleo-surface occurs near the upper, monoclinal hinges of the dome (see Figure 1). Thus, the resulting fractures are concentric, parallel, and close to the dome edge (see also Galland et al., 2016). The close relation between these tensile fractures and the hydrothermal vent complexes (Figures 7a and 8a) suggests that the former might have channeled the over-pressurized fluids, and so controlled partly the locations of the vents. Furthermore, the observed central thinning of the shallow interval (HV1-HV4) of the domed sedimentary sequence above the Tulipan sill (Figure 8c) are in good agreement with the observations of Ramsay (1967), who suggests that such thinning might result from outer-arc stretching of the apex of a growing forced fold. The presence of concentric fractures and superficial thinning are the only

evidence of forced folding associated with the emplacement of the Tulipan sill.

Other indicators of synemplacement dome growth are not visible. The significant thickness variations of the sedimentary intervals affected by the doming do not solely support the application of the elastic bending model, which assumes constant thickness of the domed formations (e.g., Pollard and Johnson, 1973; Goulty and Schofield, 2008; Galland and Scheibert, 2013). In addition, we do not observe onlap structures on the domed morphology of the paleo-surface, which could confirm the short time scale of an intrusion-induced uplift of the overburden (Figure 1a) (e.g., Trude et al., 2003; Hansen and Cartwright, 2006; Magee et al., 2014). Finally, we do not observe tensile or extensional fractures at the apex of the dome, expected from brittle outer-arc stretching, as observed for instance by Magee et al. (2013). Nevertheless, we cannot rule out that such fractures, if present, are of subseismic scale and so are undetectable. In addition, the observed polygonal fault pattern observable in the whole area (Figure 7c), which formed 57.9 Ma ago prior to the emplacement of the sill of Kjoberg et al. (2017), do not show evidence of reactivation due to forced folding.

In our results, the range of the estimated thickness t of the Tulipan sill and the values of dome amplitude f show a significant overlap. However, due the uncertainties on the sill thickness, this dome amplitude/sill thickness ratio is not conclusive, such that it is not possible to confidently constrain the ratio of contribution of the possible mechanisms for overburden deformation, i.e., elastic bending, differential compaction, and aureole volume reduction.

Our data also highlight the occurrence of hydrothermal vent complexes (Figures 6–8) (see also Kjoberg et al., 2017), which result from local fluidization and gas generation within the host rock (Einsele et al., 1980; Svensen et al., 2004; Schofield et al., 2010, 2012a; Jackson et al., 2013; Aarnes et al., 2015). Nevertheless, these authors show that any fluidization occurs dominantly close to the intrusions, and the resulting structures are likely of subseismic scale and, so, invisible on our seismic data. In addition, the well within the study area is not deep enough to reach the sedimentary rocks near the Tulipan sill; therefore, it is not useful to constrain the thickness of the fluidized rock formations (Figures 3 and 4b). Therefore, our data cannot allow us to constrain to which extent fluidization has accommodated the sill emplacement, and so, the dome growth dynamics.

Conclusion

Our study uses analysis of 3D seismic and well data to test the occurrence of dome growth dynamics associated with the Tulipan sill. We highlight that a single mechanism cannot explain development of the dome, but rather we show that a combination of different mechanisms controlled the emplacement of the Tulipan sill and its associated deformation of the sedimentary overburden in the Tulipan prospect. We conclude that

1) The dome displayed in our data is solely related to the underlying Tulipan sill.

2) Our data corroborate the contribution of differential compaction to the formation of the dome structure above the Tulipan sill.

3) Elastic bending had only a minor contribution to the accommodated deformation in the overburden of the Tulipan sill.

4) We infer the formation of dilational fractures in the vicinity and parallel to the Tulipan periphery connecting hydrothermal vent complexes. However, we cannot exclude the fact, that some of the features might be as follows: (1) circumferential tensile fractures at the surface or (2) shear fractures resulting from differential uplift at the dome edge.

5) We cannot confidently observe the process of outer-arc stretching, due to missing observations of associated fracture systems in the crest of the domed overburden.

6) Polygonal faults formed prior to the emplacement of the sill do not show evidence of reactivation due to the doming.

Future studies should concentrate on 3D seismic data in combination with well data directly pierced through sills. Where sills are directly intersected by boreholes, direct measurements of their thickness and contact effects can be examined. Such data sets will allow for a more accurate quantitative correlation on the amplitude of the domed overburden compared with the underlying intrusion thickness and will help to constrain the contribution of the different syn- and postemplacement mechanisms of overburden deformation.

References

Aarnes, I., S. Planke, M. Trulsvik, and H. Svensen, 2015, Contact metamorphism and thermogenic gas generation in the Vøring and Møre Basins, offshore Norway, during the Paleocene-Eocene thermal maximum: Journal of the Geological Society, **172**, 588–598, doi: 10.1144/jgs2014-098.

Abdelmalak, M. M., T. B. Andersen, S. Planke, J. I. Faleide, F. Corfu, C. Tegner, G. E. Shephard, D. Zastrozhnov, and R. Myklebust, 2015, The ocean-continent transition in the mid-Norwegian margin: Insight from seismic data and an onshore Caledonian field analogue: Geology, **43**, 1011–1014, doi: 10.1130/G37086.1.

Agirrezabala, L. M., 2015, Syndepositional forced folding and related fluid plumbing above a magmatic laccolith: Insights from outcrop (Lower Cretaceous, Basque-Cantabrian Basin, western Pyrenees): Geological Society of America Bulletin, **127**, 982–1000, doi: 10.1130/b31192.1.

Bell, B., and H. Butcher, 2002, On the emplacement of sill complexes: Evidence from the Faroe-Shetland Basin: Geological Society, London, Special Publications 197, 307–329.

Berndt, C., C. Hensen, C. Mortera-Gutierrez, S. Sarkar, S. Geilert, M. Schmidt, V. Liebetrau, R. Kipfer, F. Scholz, M. Doll, S. Muff, J. Karstens, S. Planke, S. Petersen, C. Böttner, W.-C. Chi, M. Moser, R. Behrendt, A. Fiskal, M. Lever, C.-C. Su, L. Deng, M. Brennwald, and D. Lizarralde, 2016, Rifting under steam — How rift magmatism triggers methane venting from sedimentary basins: Geology, **44**, 767–770, doi: 10.1130/g38049.1.

Berndt, C., S. Planke, E. Alvestad, F. Tsikalas, and T. Rasmussen, 2001, Seismic volcano stratigraphy of the Norwegian Margin: Constraints on tectonomagmatic break-up processes: Journal of the Geological Society, **158**, 413–426, doi: 10.1144/jgs.158.3.413.

Berndt, C., O. P. Skogly, S. Planke, O. Eldholm, and R. Mjelde, 2000, High-velocity breakup-related sills in the Vøring Basin, off Norway: Journal of Geophysical Research: Solid Earth, **105**, 28443–28454, doi: 10.1029/2000JB900217.

Brekke, H., 2000, The tectonic evolution of the Norwegian Sea continental margin with emphasis on the Vøring and Møre Basins: Geological Society, London, Special Publications 167, 327–378.

Bryan, S. E., I. U. Peate, D. W. Peate, S. Self, D. A. Jerram, M. R. Mawby, J. S. Marsh, and J. A. Miller, 2010, The largest volcanic eruptions on earth: Earth-Science Reviews, **102**, 207–229, doi: 10.1016/j.earscirev.2010.07.001.

Bunger, A. P., and A. R. Cruden, 2011, Modeling the growth of laccoliths and large mafic sills: Role of magma body forces: Journal of Geophysical Research: Solid Earth, **116**, B02203, doi: 10.1029/2010JB007648.

Cartwright, J., and D. M. Hansen, 2006, Magma transport through the crust via interconnected sill complexes: Geology, **34**, 929–932, doi: 10.1130/G22758A.1.

Corry, C. E., 1988, Laccoliths: Mechanics of emplacement and growth: Geological Society of America Special Paper, **220**, 1–110.

Cosgrove, J. W., and R. D. Hillier, 1999, Forced-fold development within Tertiary sediments of the Alba Field, UKCS: Evidence of differential compaction and post-depositional sandstone remobilization: Geological Society, London, Special Publications 169, 61–71.

Dalland, A., H. O. Augedahl, K. Bomstad, and K. Ofstad, 1988, The Post-Triassic succession of the mid-Norwegian shelf, in A. Dalland, D. Worsley, and K. Ofstad, eds., A lithostratigraphic scheme for the Mesozoic and Cenozoic

and succession offshore mid-and northern Norway: Norwegian Petroleum Directorate Starvanger, 1–65.

Delpino, D., A. Bermúdez, N. Vitulli, and C. Loscerbo, 2014, Sistema de Petróleo no convencional relacionado con lacolitos Eocenos de intraplaca. Área altiplanicie del Payún, cuenca Neuquina, in Proceedings IX Congreso de Exploración y Desarrollo de Hidrocarburos, Mendoza: Instituto Argentino del Petróleo y el Gas, 223–242.

de Saint-Blanquat, M., G. Habert, E. Horsman, S. S. Morgan, B. Tikoff, P. Launeau, and G. Gleizes, 2006, Mechanisms and duration of non-tectonically assisted magma emplacement in the upper crust: The Black Mesa pluton, Henry Mountains, Utah: Tectonophysics, **428**, 1–31, doi: 10.1016/j.tecto.2006.07.014.

Dixon, J. M., and D. G. Simpson, 1987, Centrifuge modeling of laccolith intrusion: Journal of Structural Geology, **9**, 87–103, doi: 10.1016/0191-8141(87)90046-0.

du Toit, A., 1920, The Karoo dolerites of South Africa: A study in hypabyssal injection: Transactions of the Geological Society of South Africa, **23**, 1–42.

Eide, C. H., N. Schofield, D. A. Jerram, and J. A. Howell, 2016, Basin-scale architecture of deeply emplaced sill complexes: Jameson Land, East Greenland: Journal of the Geological Society, **174**, 23–40, doi: 10.1144/jgs2016-018.

Einsele, G., J. M. Gieskes, J. Curray, D. M. Moore, E. Aguayo, M.-P. Aubry, D. Fornari, J. Guerrero, M. Kastner, K. Kelts, M. Lyle, Y. Matoba, A. Molina-Cruz, J. Niemitz, J. Rueda, A. Saunders, H. Schrader, B. Simoneit, and V. Vacquier, 1980, Intrusion of basaltic sills into highly porous sediments, and resulting hydrothermal activity: Nature, **283**, 441–445, doi: 10.1038/283441a0.

Faleide, J. I., K. Bjørlykke, and R. H. Gabrielsen, 2010, Geology of the Norwegian continental shelf, petroleum geoscience: Springer, 467–499.

Galerne, C. Y., O. Galland, E.-R. Neumann, and S. Planke, 2011, 3D relationships between sills and their feeders: Evidence from the Golden Valley Sill Complex (Karoo Basin) and experimental modeling: Journal of Volcanology and Geothermal Research, **202**, 189–199, doi: 10.1016/j.jvolgeores.2011.02.006.

Galland, O., 2012, Experimental modeling of ground deformation associated with shallow magma intrusions: Earth and Planetary Science Letters, **317–318**, 145–156, doi: 10.1016/j.epsl.2011.10.017.

Galland, O., H. S. Bertelsen, F. Guldstrand, L. Girod, R. F. Johannessen, F. Bjugger, S. Burchardt, and K. Mair, 2016, Application of open-source photogrammetric software MicMac for monitoring surface deformation in laboratory models: Journal of Geophysical Research: Solid Earth, **121**, 2852–2872, doi: 10.1002/2015JB012564.

Galland, O., S. Burchardt, E. Hallot, R. Mourgues, and C. Bulois, 2014, Dynamics of dikes versus cone sheets in volcanic systems: Journal of Geophysical Research: Solid Earth, **119**, 6178–6192, doi: 10.1002/2014JB011059.

Galland, O., E. Holohan, B. van Wyk de Vries, and S. Burchardt, 2015, Laboratory modeling of volcano plumbing systems: A review, in C. Breitkreuz and S. Rocchi, eds., Advances in volcanology: Springer, 1–68.

Galland, O., S. Planke, E.-R. Neumann, and A. Malthe-Sørenssen, 2009, Experimental modeling of shallow magma emplacement: Application to saucer-shaped intrusions: Earth and Planetary Science Letters, **277**, 373–383, doi: 10.1016/j.epsl.2008.11.003.

Galland, O., and J. Scheibert, 2013, Analytical model of surface uplift above axisymmetric flat-lying magma intrusions: Implications for sill emplacement and geodesy: Journal of Volcanology and Geothermal Research, **253**, 114–130, doi: 10.1016/j.jvolgeores.2012.12.006.

Gilbert, G. K., 1877, Report on the geology of the Henry Mountains, Washington: U. S. Geographical Geological Survey of the Rocky Mountain, Region.

Goulty, N. R., and N. Schofield, 2008, Implications of simple flexure theory for the formation of saucer-shaped sills: Journal of Structural Geology, **30**, 812–817, doi: 10.1016/j.jsg.2008.04.002.

Hansen, D. M., and J. Cartwright, 2006, The three-dimensional geometry and growth of forced folds above saucer-shaped igneous sills: Journal of Structural Geology, **28**, 1520–1535, doi: 10.1016/j.jsg.2006.04.004.

Hansen, J., D. A. Jerram, K. McCaffrey, and S. R. Passey, 2011, Early Cenozoic saucer-shaped sills of the Faroe Islands: An example of intrusive styles in basaltic lava piles: Journal of the Geological Society, **168**, 159–178, doi: 10.1144/0016-76492010-012.

Hutton, D., 2009, Insights into magmatism in volcanic margins: Bridge structures and a new mechanism of basic sill emplacement — Theron Mountains, Antarctica: Petroleum Geoscience, **15**, 269–278, doi: 10.1144/1354-079309-841.

Jackson, C. A.-L., N. Schofield, and B. Golenkov, 2013, Geometry and controls on the development of igneous sill-related forced folds: A 2-D seismic reflection case study from offshore southern Australia: Geological Society of America Bulletin, **125**, 1874–1890, doi: 10.1130/B30833.1.

Jerram, D. A., and S. E. Bryan, 2017, Plumbing systems of shallow level intrusive complexes, in C. Breitkreuz and S. Rocchi, eds., Advances in volcanology: Springer, 1–22.

Kavanagh, J. L., T. Menand, and R. S. J. Sparks, 2006, An experimental investigation of sill formation and propagation in layered elastic media: Earth and Planetary Science Letters, **245**, 799–813, doi: 10.1016/j.epsl.2006.03.025.

Kay, S. M., O. Mancilla, and P. Copeland, 2006, Evolution of the late Miocene Chachahuén volcanic complex at 37°S over a transient shallow subduction zone under the Neuquén Andes: Geological Society of America Special Papers, **407**, 215–246, doi: 10.1130/2006.2407(10).

Kjoberg, S., T. Schmiedel, S. Planke, H. Svensen, J. Millett, D. A. Jerram, O. Galland, I. Lecomte, N. Schofield, Ø. T. Haug, and A. Heslem, 2017, 3D structure and formation

of hydrothermal vent complexes at the Paleocene-Eocene transition, the Møre Basin, mid-Norwegian Margin: Interpretation, **5**, this issue, doi: 10.1190/int-2016-0159.1.

Kontorovich, A. E., A. V. Khomenko, L. M. Burshtein, I. I. Likhanov, A. L. Pavlov, V. S. Staroseltsev, and A. A. Ten, 1997, Intense basic magmatism in the Tunguska petroleum basin, eastern Siberia, Russia: Petroleum Geoscience, **3**, 359–369, doi: 10.1144/petgeo.3.4.359.

Magee, C., F. Briggs, and C. A. L. Jackson, 2013, Lithological controls on igneous intrusion-induced ground deformation: Journal of the Geological Society, **170**, 853–856, doi: 10.1144/jgs2013-029.

Magee, C., C. A.-L. Jackson, and N. Schofield, 2014, Diachronous sub-volcanic intrusion along deep-water margins: Insights from the Irish Rockall Basin: Basin Research, **26**, 85–105, doi: 10.1111/bre.2014.26.issue-1.

Magee, C., S. M. Maharaj, T. Wrona, and C. A.-L. Jackson, 2015, Controls on the expression of igneous intrusions in seismic reflection data: Geosphere, **11**, 1024–1041, doi: 10.1130/GES01150.1.

Magee, C., J. D. Muirhead, A. Karvelas, S. P. Holford, C. A. L. Jackson, I. D. Bastow, N. Schofield, C. T. E. Stevenson, C. McLean, and W. McCarthy, 2016, Lateral magma flow in mafic sill complexes: Geosphere, **12**, 809–841, doi: 10.1130/GES01256.1.

Malthe-Sørenssen, A., S. Planke, H. Svensen, and B. Jamtveit, 2004, Formation of saucer-shaped sills: Geological Society, London, Special Publications 234, 215–227.

Menand, T., 2008, The mechanics and dynamics of sills in layered elastic rocks and their implications for the growth of laccoliths and other igneous complexes: Earth and Planetary Science Letters, **267**, 93–99, doi: 10.1016/j.epsl.2007.11.043.

Morgan, S., A. Stanik, E. Horsman, B. Tikoff, M. de Saint Blanquat, and G. Habert, 2008, Emplacement of multiple magma sheets and wall rock deformation: Trachyte Mesa intrusion, Henry Mountains, Utah: Journal of Structural Geology, **30**, 491–512, doi: 10.1016/j.jsg.2008.01.005.

Planke, S., T. Rasmussen, S. S. Rey, and R. Myklebust, 2005, Seismic characteristics and distribution of volcanic intrusions and hydrothermal vent complexes in the Vøring and Møre Basins: Geological Society, London, Petroleum Geology Conference Series 6, 833–844.

Planke, S., H. Svensen, R. Myklebust, S. Bannister, B. Manton, and L. Lorenz, 2015, Geophysics and remote sensing, *in* C. Breitkreuz and S. Rocchi, eds., Advances in volcanology: Springer, 1–16.

Planke, S., P. A. Symonds, E. Alvestad, and J. Skogseid, 2000, Seismic volcanostratigraphy of large-volume basaltic extrusive complexes on rifted margins: Journal of Geophysical Research: Solid Earth, **105**, 19335–19351, doi: 10.1029/1999JB900005.

Pollard, D. D., and A. M. Johnson, 1973, Mechanics of growth of some laccolithic intrusions in the Henry mountains, Utah. II: Bending and failure of overburden

layers and sill formation: Tectonophysics, **18**, 311–354, doi: 10.1016/0040-1951(73)90051-6.

Polteau, S., A. Mazzini, O. Galland, S. Planke, and A. Malthe-Sørenssen, 2008, Saucer-shaped intrusions: Occurrences, emplacement, and implications: Earth and Planetary Science Letters, **266**, 195–204, doi: 10.1016/j.epsl.2007.11.015.

Potter, J., and J. Konnerup-Madsen, 2003, A review of the occurrence and origin of a biogenic hydrocarbons in igneous rocks: Hydrocarbons in Crystalline Rocks, **214**, 151–173, doi doi: 10.1144/GSL.SP.2003.214.01.10.

Ramsay, J. G., 1967, Folding and fracturing of rocks: McGraw-Hill Companies.

Rodriguez Monreal, F., H. J. Villar, R. Baudino, D. Delpino, and S. Zencich, 2009, Modeling an atypical petroleum system: A case study of hydrocarbon generation, migration and accumulation related to igneous intrusions in the Neuquen Basin, Argentina: Marine and Petroleum Geology, **26**, 590–605, doi: 10.1016/j.marpetgeo.2009.01.005.

Roman-Berdiel, T., D. Gapais, and J. P. Brun, 1995, Analogue models of laccolith formation: Journal of Structural Geology, **17**, 1337–1346, doi: 10.1016/0191-8141(95)00012-3.

Schofield, N., I. Alsop, J. Warren, J. R. Underhill, R. Lehné, W. Beer, and V. Lukas, 2014, Mobilizing salt: Magma-salt interactions: Geology, **42**, 599–602, doi: 10.1130/G35406.1.

Schofield, N., L. Heaton, S. P. Holford, S. G. Archer, C. A.-L. Jackson, and D. W. Jolley, 2012b, Seismic imaging of 'broken bridges': Linking seismic to outcrop-scale investigations of intrusive magma lobes: Journal of the Geological Society, **169**, 421–426, doi: 10.1144/0016-76492011-150.

Schofield, N., D. J. Brown, C. Magee, and C. T. Stevenson, 2012a, Sill morphology and comparison of brittle and non-brittle emplacement mechanisms: Journal of the Geological Society, **169**, 127–141, doi: 10.1144/0016-76492011-078.

Schofield, N., S. Holford, J. Millett, D. Brown, D. Jolley, S. R. Passey, D. Muirhead, C. Grove, C. Magee, J. Murray, M. Hole, C. A.-L. Jackson, and C. Stevenson, 2015, Regional magma plumbing and emplacement mechanisms of the Faroe-Shetland Sill Complex: implications for magma transport and petroleum systems within sedimentary basins: Basin Research, **29**, 41–63, doi: 10.1111/bre.12164.

Schofield, N., C. Stevenson, and T. Reston, 2010, Magma fingers and host rock fluidization in the emplacement of sills: Geology, **38**, 63–66, doi: 10.1130/G30142.1.

Schutter, S. R., 2003a, Hydrocarbon occurrence and exploration in and around igneous rocks: Geological Society, London, Special Publications 214, 7–33.

Schutter, S. R., 2003b, Occurrences of hydrocarbons in and around igneous rocks: Geological Society, London, Special Publications 214, 35–68.

Senger, K., S. J. Buckley, L. Chevallier, Å. Fagereng, O. Galland, T. H. Kurz, K. Ogata, S. Planke, and J. Tveranger, 2015, Fracturing of doleritic intrusions and associated contact zones: Implications for fluid flow in volcanic ba-

sins: Journal of African Earth Sciences, **102**, 70–85, doi: 10.1016/j.jafrearsci.2014.10.019.

Senger, K., J. Millett, S. Planke, K. Ogata, C. Eide, M. Festøy, O. Galland, and D. A. Jerram, forthcoming, Effects of igneous intrusions on the petroleum system: A review: First Break.

Smallwood, J. R., and J. Maresh, 2002, The properties, morphology and distribution of igneous sills: Modeling, borehole data and 3D seismic from the Faroe-Shetland area: Geological Society, London, Special Publications 197, 271–306.

Stearns, D. W., 1978, Faulting and forced folding in the Rocky Mountains foreland: Geological Society of America Memoirs, **151**, 1–38, doi: 10.1130/MEM151.

Svensen, H., F. Corfu, S. Polteau, Ø. Hammer, and S. Planke, 2012, Rapid magma emplacement in the Karoo Large Igneous Province: Earth and Planetary Science Letters, **325–326**, 1–9, doi: 10.1016/j.epsl.2012.01.015.

Svensen, H., S. Planke, A. Malthe-Sørenssen, B. Jamtveit, R. Myklebust, T. Rasmussen Eidem, and S. S. Rey, 2004, Release of methane from a volcanic basin as a mechanism for initial Eocene global warming: Nature, **429**, 542–545, doi: 10.1038/nature02566.

Thomson, K., and D. Hutton, 2004, Geometry and growth of sill complexes: Insights using 3D seismic from the North Rockall Trough: Bulletin of Volcanology, **66**, 364–375, doi: 10.1007/s00445-003-0320-z.

Thomson, K., and N. Schofield, 2008, Lithological and structural controls on the emplacement and morphology of sills in sedimentary basins: Geological Society, London, Special Publications 302, 31–44.

Timoshenko, S. P., and S. Woinowsky-Krieger, 1959, Theory of plates and shells: McGraw-Hill Book Company.

Trude, J., J. Cartwright, R. J. Davies, and J. R. Smallwood, 2003, New technique for dating igneous sills: Geology, **31**, 813–816, doi: 10.1130/G19559.1.

Wilson, P. I. R., K. J. W. McCaffrey, R. W. Wilson, I. Jarvis, and R. E. Holdsworth, 2016, Deformation structures associated with the Trachyte Mesa intrusion, Henry Mountains, Utah: Implications for sill and laccolith emplacement mechanisms: Journal of Structural Geology, **87**, 30–46, doi: 10.1016/j.jsg.2016.04.001.

Witte, J., M. Bonora, C. Carbone, and O. Oncken, 2012, Fracture evolution in oil-producing sills of the Rio Grande Valley, northern Neuquen Basin, Argentina: AAPG Bulletin, **96**, 1253–1277, doi: 10.1306/10181110152.

Zhao, F., S. Wu, Q. Sun, M. Huuse, W. Li, and Z. Wang, 2014, Submarine volcanic mounds in the Pearl River Mouth Basin, northern South China Sea: Marine Geology, **355**, 162–172, doi: 10.1016/j.margeo.2014.05.018.

Biographies and photographs of the authors are not available.

A.2 Publication II

II

Kjoberg, S., Schmiedel, T., Planke, S., Svensen, H.H., Millett, J.M., Jerram, D.A., Galland, O., Lecomte, I., Schofield, N., Haug, Ø.T., Helsem, A., (2017). *3D structure and formation of hydrothermal vent complexes at the Paleocene-Eocene transition, the Møre Basin, mid-Norwegian margin*. Interpretation 5, SK65-SK81. doi: 10.1190/int-2016-0159.1

3D structure and formation of hydrothermal vent complexes at the Paleocene-Eocene transition, the Møre Basin, mid-Norwegian margin

Sigurd Kjoberg[1], Tobias Schmiedel[2], Sverre Planke[3], Henrik H. Svensen[1], John M. Millett[4], Dougal A. Jerram[5], Olivier Galland[2], Isabelle Lecomte[6], Nick Schofield[7], Øystein T. Haug[2], and Andreas Helsem[8]

Abstract

The mid-Norwegian margin is regarded as an example of a volcanic-rifted margin formed prior to and during the Paleogene breakup of the northeast Atlantic. The area is characterized by the presence of voluminous basaltic complexes such as extrusive lava and lava delta sequences, intrusive sills and dikes, and hydrothermal vent complexes. We have developed a detailed 3D seismic analysis of fluid- and gas-induced hydrothermal vent complexes in a 310 km^2 area in the Møre Basin, offshore Norway. We find that formation of hydrothermal vent complexes is accommodated by deformation of the host rock when sills are emplaced. Fluids are generated by metamorphic reactions and pore-fluid expansion around sills and are focused around sill tips due to buoyancy. Hydrothermal vent complexes are associated with doming of the overlying strata, leading to the formation of draping mounds above the vent contemporary surface. The morphological characteristics of the upper part and the underlying feeder structure (conduit zone) are imaged and studied in 3D seismic data. Well data indicate that the complexes formed during the early Eocene, linking their formation to the time of the Paleocene-Eocene thermal maximum at c. 56 Ma. The well data further suggest that the hydrothermal vent complexes were active for a considerable time period, corresponding to a c. 100 m thick transition zone unit with primary *Apectodinium augustum* and redeposited very mature Cretaceous and Jurassic palynomorphs. The newly derived understanding of age, structure, and formation of hydrothermal vent complexes in the Møre Basin contributes to the general understanding of the igneous plumbing system in volcanic basins and their implications for the paleoclimate and petroleum systems.

Introduction

At the mid-Norwegian margin, the Paleocene-Eocene interval represents the time period of the early northeast Atlantic rifting and continental breakup (Gibb and Kanaris-Sotiriou, 1988; Bell and Butcher, 2002). Evidence for volcanic activity in sedimentary basins is found along the entire European northeast Atlantic margin (Doré et al., 1999). Volcanic processes and deposits may have significant impact on the structural and geodynamic development of the rifted margin and associated sedimentary basins, i.e., the Karoo Basin, the Rockall Basin, the Faroe-Shetland Basin, and the Neuquén Basin (Smallwood and Maresh, 2002; Svensen et al., 2012; Magee et al., 2014; Schofield et al., 2017). The Møre Basin study area is located beneath the outer shelf and slope region offshore mid-Norway, and it shows classic examples of how volcanic activity and igneous intrusions within sedimentary strata may impact the basin structure (Skogseid et al., 1992; Brekke, 2000). The short- and long-term impacts include deformation, differential compaction, uplift, heating of host rock and pore fluids, metamorphism, and the formation of hydrothermal vent complexes (HTVCs).

The distribution and nature of volcanic intrusions and associated hydrothermal vent complexes represent key elements in basin evolution, and therefore it is important to better constrain the age of the main volcanic

[1]The University of Oslo, The Centre for Earth Evolution and Dynamics (CEED), Oslo, Norway. E-mail: sigurdkj@geo.uio.no; hensven@geo.uio.no.

[2]The University of Oslo, Physics of Geological Processes (PGP), Oslo, Norway. E-mail: tobias.schmiedel@geo.uio.no; olivier.galland@geo.uio.no; o.t.haug@geo.uio.no.

[3]The University of Oslo, The Centre for Earth Evolution and Dynamics (CEED), Oslo, Norway, and Volcanic Basin Petroleum Research (VBPR), Oslo, Norway. E-mail: planke@vbpr.no.

[4]Volcanic Basin Petroleum Research (VBPR), Oslo, Norway and The University of Aberdeen, Aberdeen, UK. E-mail: john.millett@vbpr.no.

[5]The University of Oslo, The Centre for Earth Evolution and Dynamics (CEED), Oslo, Norway and DougalEarth, Solihull, UK. E-mail: dougal@dougalearth.com.

[6]NORSAR, Kjeller, Norway and The University of Bergen, Bergen, Norway. E-mail: isabelle.lecomte@uib.no.

[7]The University of Aberdeen, Aberdeen, UK. E-mail: n.schofield@abdn.ac.uk.

[8]Statoil, Stavanger, Norway. E-mail: anhell@statoil.com.

episode and the coherent venting processes. In addition, the venting process has been related to greenhouse gas expulsion to the atmosphere, thereby providing a link to the transient climatic shift during the Paleocene-Eocene Thermal Maximum (PETM) (Svensen et al., 2004; Berndt et al., 2016). The climatic records during this period are well documented from several sections worldwide (Zachos et al., 2001; Zachos et al., 2008), and recent results show that the only drilled HTVC in the Vøring Basin (borehole 6607/12-1) formed during the PETM plateau, thereby demonstrating a relationship between the long duration of the PETM and the gas venting (Frieling et al., 2016). Similar kilometer-scale hydrothermal vent structures have been described elsewhere in seismic data (Hansen et al., 2005; Planke et al., 2005; Grove, 2013; Berndt et al., 2016) and in outcrops (Svensen et al., 2006) in several basins. These vent structures all share structural similarities, including complete brecciation, fluidization, and inward-dipping reflections. However, the upper parts of these vents imaged on seismic data often exhibit distinct structural features (eye, crater, and dome shapes). The mechanisms leading to different structures are currently unknown. In addition, the structural features observed in seismic data differ from those described in field and outcrop studies. It is not clear whether the differences between seismic features and geologic observations are real structural differences or the result of artifacts in the seismic images.

The aim of this study is to increase our understanding of the formation and age of hydrothermal venting in volcanic basins. This study is based on structural imaging and detailed mapping of morphological features in a 3D seismic survey acquired in the Møre Basin, together with well-log data and analyses. We further apply a new workflow to better constrain the complex structures of hydrothermal vent complexes on seismic images, using a combination of qualitative laboratory models and advanced seismic modeling. These results may help identify potential artifacts related to fluid and sediment remobilization in seismic images.

Møre Basin geological setting

The mid-Norwegian margin developed through a series of post-Caledonian rift phases that culminated with the onset of seafloor spreading ca. 56 Ma in the Norwegian-Greenland Sea (Mosar et al., 2002). The Møre and Vøring margin segments, each between 400 and 500 km long, are separated by the Jan Mayen Fracture Zone (Figure 1; Faleide et al., 2008). The deep Møre and Vøring Basins formed during Late Jurassic-Early Cretaceous rifting episodes (Figure 1). The basins are characterized by thick Cretaceous sedimentary accumulations and can in places reach up to 13 km, of which 8–9 km comprises the Cretaceous succession (Gernigon et al., 2003). Continental breakup was accompanied by large-scale igneous activity, forming kilometer-thick basaltic complexes on both sides of the continent-ocean boundary (Brekke, 2000). At the same time, extensive igneous sheet intrusions were emplaced in the Møre Basin, and hundreds of hydrothermal vent complexes were
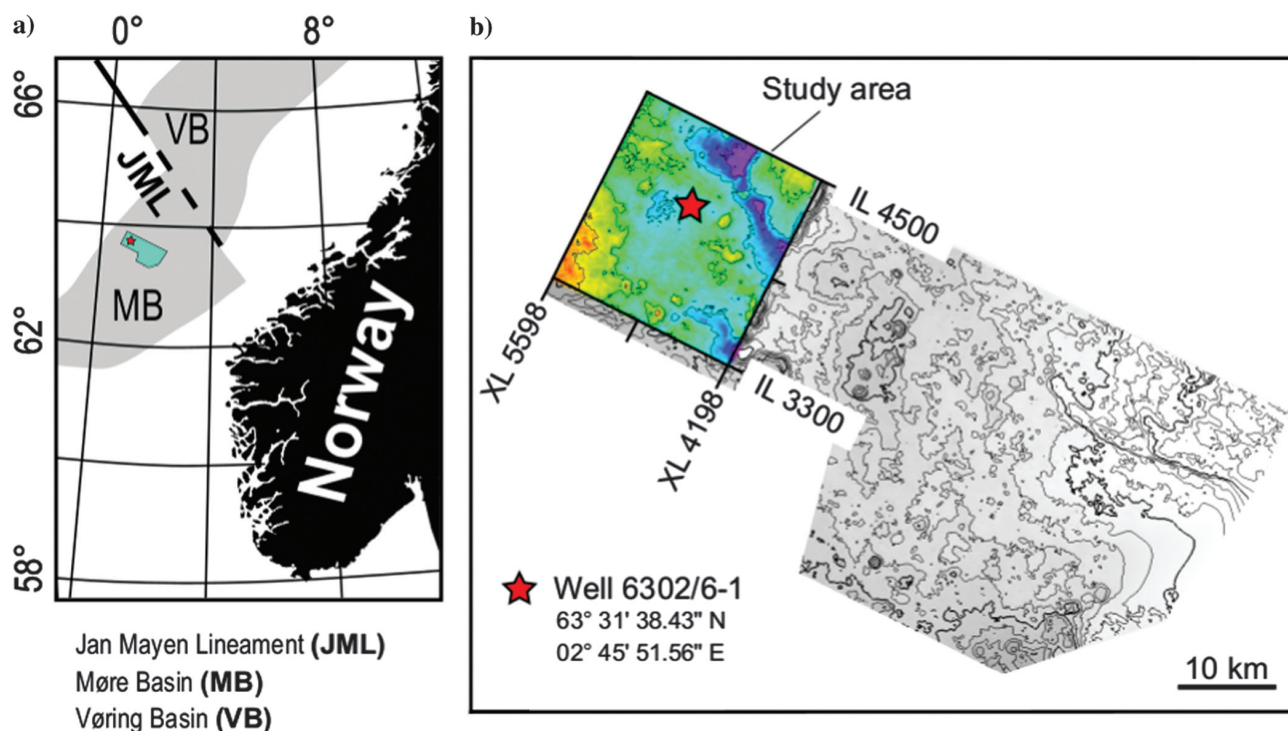

Figure 1. Location map showing the study area in the Møre Basin on the mid-Norwegian margin. The 3D survey is approximately 2100 km^2, and the interpreted study area is approximately 310 km^2.

formed by pressure increase and devolatilization in the contact aureoles around the sills (Planke et al., 2005, 2015; Svensen et al., 2004; Svensen and Jamtveit, 2010; Frieling et al., 2015). The Møre Basin subsequently subsided, leading to deposits of marine mud and ooze, and finally thick sequences of glacially derived sediments and slide material (Faleide et al., 2008).

Stratigraphy

The seismic well-tie in the Paleogene and Neogene (Cenozoic) successions is confident (Figure 2). However, the sequences less than 4.4 s two way traveltime (TWT) of late Cretaceous age are difficult to tie because of imaging problems and lack of well data. The stratigraphy includes five formations and is described from the oldest to youngest unit. In the study area, the lowermost interpreted formation is the Springar Formation. It consists of predominantly grayish-green claystones interbedded with stringers of carbonates and sandstone (Dalland et al., 1988). Limestone beds exceeding 10 m

in thickness interbedded with shale are encountered at an interval from 4076 to 4140 m (measured depth [MD]). The Springar Formation is overlain by the Paleogene Tang Formation, which is characterized by dark-gray to brown claystone with minor sandstone and limestone (Dalland et al., 1988). The lithology of the lowermost part and the transitional zone into the Springar Formation is interpreted as the Danian sandstone reservoir of the Tulipan discovery. These sandstone layers are typically 1–7 m thick and interbedded with siltstone and claystone in the depth range between 3901 and 4000 m (MD).

The Tare Formation is defined by dark-gray, green, or brown claystones with some thin sandstone stringers and a variable content of tuffaceous material. The tuff content is highest toward the basal section of the formation, with increasing volume in the lowermost Eocene sediments. The Tare Formation is overlain by the late Eocene to middle Miocene Brygge Formation, which is part of the Hordaland group (Deagan and Scull, 1977; Dalland et al., 1988). The Brygge Formation consists mainly of
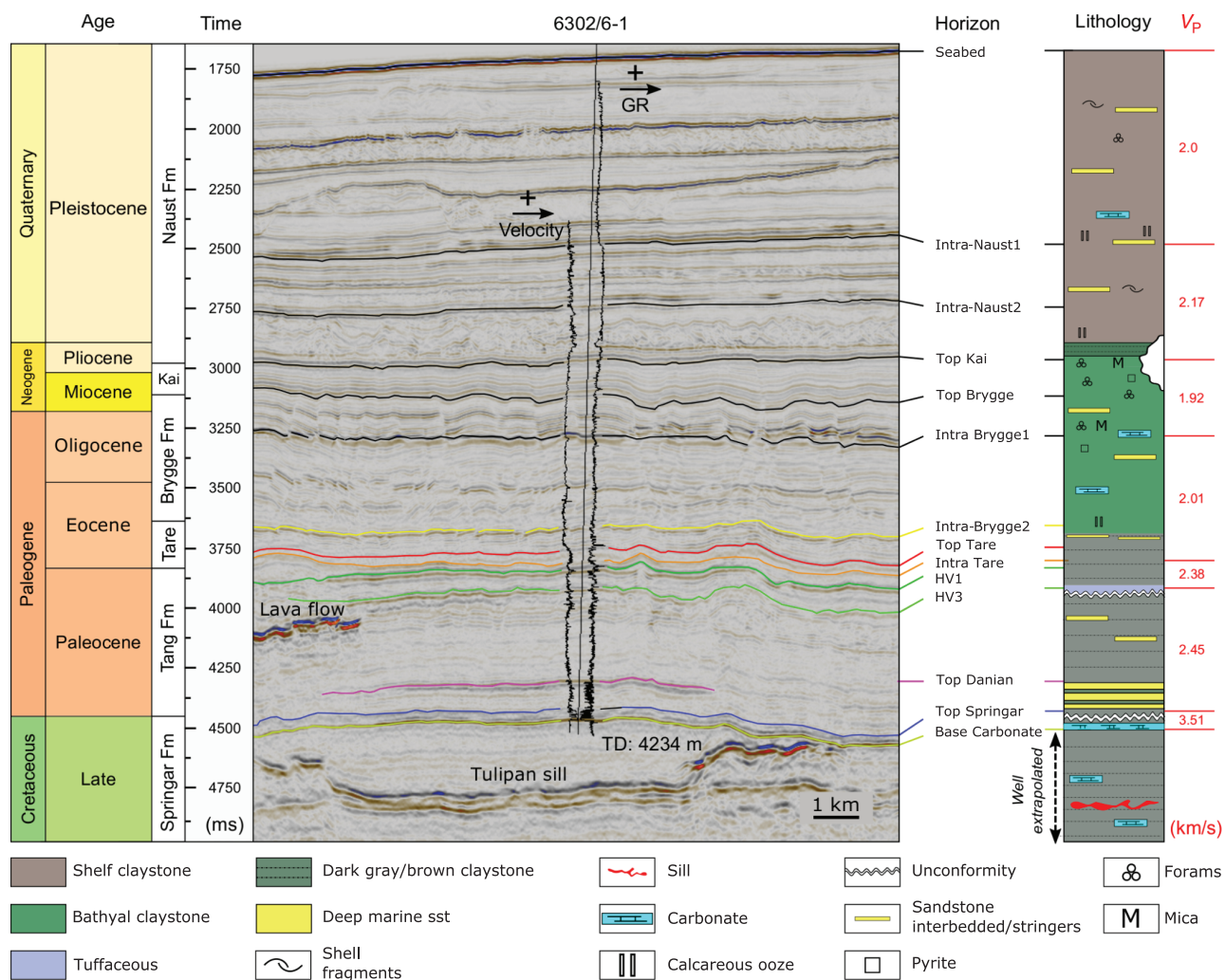
Figure 2. Summary diagram showing the key-interpreted horizons and synthesis of well 6302/6-1 lithostratigraphic data. See Figure 1 for the profile location.

claystone, interbeds of sandstone, and biosiliceous ooze (Hjelstuen et al., 1997). The two uppermost formations in the study area are the Lower Miocene to recent Nordland group that is subdivided into the Kai Formation and the upper Pliocene Naust Formation (Dalland et al., 1988). The Kai Formation consists of alternating claystone, silt-stone, and sandstone with interbedded limestone, and the Naust Formation mainly comprises claystone and siltstone.

Formation and source of hydrothermal vent complexes

The formation of hydrothermal complexes (HTVCs) requires that fluid pressure within contact aureoles overcomes the rock strength and the lithostatic pressure. Instantaneous overpressure release occurs if the pressure buildup is faster than the pressure release and seepage in the host rock. Jamtveit et al. (2004) and Nermoen et al. (2010) propose a model in which the venting mechanism is based on boiling and expansion of pore water as the cause for pressure buildup. If the fluids generated are greater than allowable through Darcy flow, a critical state is reached and venting can occur (Jamtveit et al., 2004; Nermoen et al., 2010). Lithologic information from the Møre Basin shows that the host rock consists of primarily mudstone, claystone, and sandstone at the HTVC interval. Mudstone heating can result in clay mineral dehydration and organic matter breakdown to CO_2 and CH_4, contributing to overpressure generation (see Svensen et al., 2004, 2007; Aarnes et al., 2010). The fluid generation is critically dependent on the heat transfer from the sill and is a function of host rock properties, sill thickness and temperature, and the geothermal gradient (Aarnes et al., 2010; Grapes, 2010).

Fluids generated in contact aureoles have low densities and greater buoyancy compared with the pore fluids in the sedimentary rocks. The presence of lighter components, such as methane, may dissolve in the fluids or migrate as a gas phase during the formation of HTVCs (Svensen and Jamtveit, 2010; Wang and Manga, 2015). The volume of these carbon-bearing gases depends on the total amount of organic carbon in the host rock (Whitaker, 1986).

Data and methods
Seismic and well data

The seismic data used in this paper consist of a subsection (310 km^2) of the ST0105 (Tulipan) 3D survey (2100 km), collected and processed in connection with the PL251 license in 2005. The survey is situated in the western part of the Møre Basin, offshore mid-Norway (Figure 1). The data are 3D time migrated, and the overall quality is regarded as very good. The main frequency spectrum of the data is approximately 20–40 Hz (3.7–4.5 s TWT). This implies a dominant wavelength of 30–50 m, corresponding to a vertical seismic resolution of approximately 10 m ($\delta h = \lambda/4$: one quarter of the dominant wavelet). The data are regarded as zero phase

and displayed so that white/blue (depending on color scheme) denotes an increase in acoustic impedance.

Borehole check-shot and conventional wireline log data from the Tulipan well (6302/6-1; Figure 2) show that velocities vary from approximately 2000 m/s at the seafloor to more than 3000 m/s at the base of the interpretation interval. Finally, 6302/6-1 borehole stratigraphy, petrography, and biostratigraphy reports were made available from Statoil. Results from these reports are summarized in Figure 2.

Seismic interpretation

In total, 14 seismic horizons were interpreted regionally in the study area based on the seismic well tie to 6302/6-1 (Figure 2). The interpretation focused on the Paleocene and Eocene sequences, in particular, the Intra Brygge 2, Top Tare, Intra Tare, HV1, and HV3 horizons. These horizons are well-defined, continuous events in the study area (Figure 2) and are used to define the upper part of the hydrothermal vent complexes. In addition, sills and lava flows were interpreted using the approach of Planke et al. (2015).

The upper part of each vent complex is defined as a domed region with down-lapping internal reflections on HV1. In 3D, the dome structures display an ellipsoidal geometry. Thus, the lengths of the minor and major axes could be determined. The conduit height is defined as the depth between the termination of the interpreted underlying feeder sill and the HV1 surface. The depth to the sill is not always clearly defined because a vent complex may have originated from deeper, poorly imaged sills.

Sandbox and seismic modeling

One of the main challenges regarding interpretation of seismic images and complex geologic structures is to avoid potential pitfalls and misinterpretations due to, e.g., seismic artifacts, illumination, and resolution issues. To overcome this challenge, new seismic modeling appears as a valuable tool to separate the real structure from a seismic artifact (Lecomte et al., 2015).

The principle of seismic modeling is to use geometric and attribute input parameters to produce a synthetic seismic image. The comparison between the input geometry and the resulting image is a key aspect of deciphering between the real structures and the artifacts on seismic data. As geometric input parameter for hydrothermal vent complexes, a laboratory experiment of fluid overpressure structures in granular and unconsolidated media has been undertaken. These experiments proved very useful to unravel the dynamics of venting, with applications to pockmarks, mud volcanoes, hydrothermal vent complexes, and kimberlite pipes (Nermoen et al., 2010; Haug et al., 2013; Galland et al., 2014). Importantly, the structures simulated in the laboratory are comparable in geometry with the structures observed in the field, although the laboratory models have to be upscaled.

The sandbox experiment setup consisted of a vertically orientated, air-filled Hele-Shaw cell measuring 60×60 cm (Nermoen et al., 2010; Haug et al., 2013).

The cell is sealed at the bottom and the vertical sides, whereas the top part of the cell remains open. Each experiment was prepared by slowly pouring alternating olivine sand and quartz sand through a funnel, from the top of the cell to a desired filling height. Overpressurized air from a constant supply was injected into the sand through an inlet placed within the bed. The flow velocities in the experiment were regarded as constant because the air supply was induced at a uniform pressure throughout the experiments. Digital images during the experiment were captured at seven frames per second using a high-resolution camera.

The most representative picture obtained during the sandbox experiment served as a target model for the synthetic seismic modeling. The target model was implemented into the modeling software (SeisRox) as a 2D layer model. The sand makes up the basic geometry of the model and it is defined by the different layers related to the sedimentary sequences and the coherent change in elastic values (V_P and V_S velocities). The following assumptions were further implemented:

1) The horizontal and vertical sizes of the background picture are defined as 1800 and 850 m, respectively, based on dimension analysis done during seismic interpretation.
2) Velocity data available from sonic logs at the HTVC ranges V_P from 2000 to 2500 m/s and V_S from 1100 to 1800 m/s, increasing with depth.
3) Two sets of velocities properties (V_P and V_S) were implemented to create the impedance/reflectivity model. These values range V_P between 2000 and 2300 m/s and V_S between 1200 and 1300 m/s.
4) Density in the model varies from 2.0 to 2.2 g/cm^3.
5) The seismic properties within each zone are homogeneous and identical throughout the sequence, with no internal reflections.
6) Seismic modeling of 20 Hz, corresponding to the HTVC interval.

Results
Distribution of sills and vent complexes

All HTVCs mapped in this study are related to underlying sills. Most of the vent complexes are associated with the saucer-shaped Tulipan sill located in the central part of the study area (Schmiedel et al., 2017). Due to the distinctive sill geometry, it is regarded as an important element in explaining the behavior, position, and structural development of the HTVCs. The extensive sill complex in the Tulipan 3D cube is interpreted based on the same method as the horizon interpretation (Planke et al., 2015). The sills are identified as high-amplitude reflections within the sedimentary strata and they

display local transgressive segments. Three sills have been mapped and picked as separate horizons. The lowermost sill is difficult to map with confidence, due to the acoustic masking of the overlying intrusions. The Tulipan sill is a saucer-shaped intrusion and it is easily recognized in the seismic section. Figure 2 shows that the Tulipan sill is forcing a dome-shaped morphology of the overlying Base Carbonate, Top Springar, and Top Danian horizons (Schmiedel et al., 2017). The Base Carbonate and Top Springar horizons are intersected and pierced by the transgressive segments of the sill, resulting in the most prominent HTVCs in the study area.

Figures 3 and 4 show the relationship between the underlying sills and the position of the different HTVCs. HV1 is the horizon of which the dome reflections are down-lapping. The spectral decomposition horizon in Figure 4 shows a clear relationship between the geometry of the underlying sills and the location of the vent complexes. Most of the vent complexes are seen along the outer margins of the Tulipan sill. The differences in rim elevation at the sill margin cause the conduit zones to shallow and deepen, depending on the sill position and elevation. Deeper situated vents are observed, in which the sills are less inclined.

Seismic characteristics of the HTVC

The recognition of the hydrothermal vent complexes is based primarily on interpretation of two horizons in the Paleogene sequence: HV1 and Top Tare (Figures 2 and 4). The reference horizon HV1 is defined by the seismic characteristics and well-defined geometry of the upper part of the vent complexes. In this study, 13 individual vent complexes have been identified and analyzed (Figures 4 and 5).

The upper part of the HTVC is seen in the seismic cross section as a dome down-lapping onto the HV1 paleosurface (Figures 5 and 6). The geometry and structural context display similarities to vent complexes described elsewhere on the Norwegian margin and in
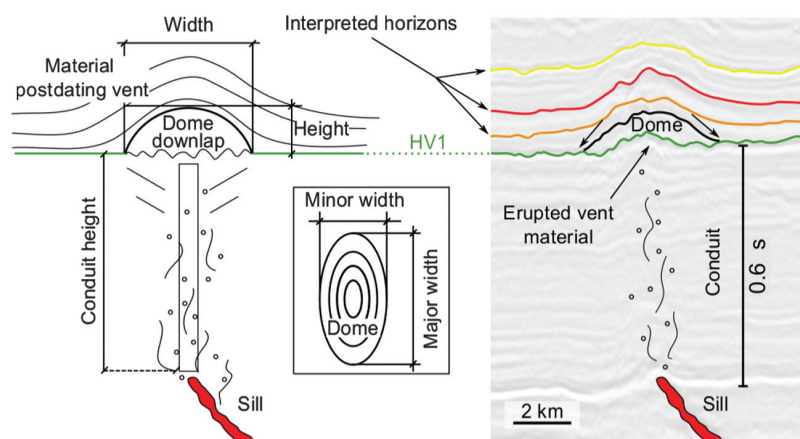

Figure 3. Schematic drawing together with seismic section showing the measurement criteria for the dome and conduit zone height and width of a hydrothermal vent complex.

the Faroe Shetland Basin (Planke et al., 2005; Schofield et al., 2015). However, only vent complexes with dome-shaped upper parts are present in the study area. Slight depressions are observed at the base of some structures, but the overall structure consists of a down-lapping dome, and no eye- or crater-shaped features are found as in the study of Planke et al. (2005). All of the vent complexes mapped in this study display a dome feature above HV1. Not all the domes down-lap onto HV1, but the majority do (11 out of 13), suggesting that this is a dominant behavior of the HTVCs in this part of the Møre Basin. Figure 6 illustrates domes on the HV1 horizon where the height of the structure is approximately 0.1 s (TWT), corresponding to 80–100 m. The domes are used to give a qualitative measurement of the geometries of the upper part of the vent complexes (Table 1; Figure 7).
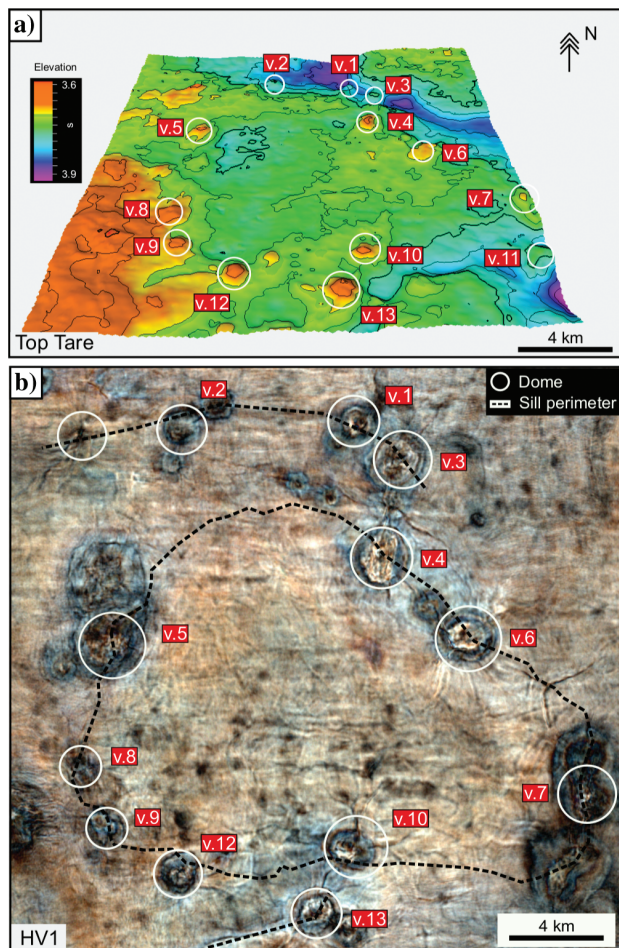
Figure 4. Dome geometry and morphology. (a) Time-structure map of the Top Tare (approximately intra-Eocene) horizon. White circles indicate the position of the dome structure of the HTVC, labeled v.1 to v.13. (b) Spectral decomposition of the HV1 paleosurface (red, 22 Hz;, green, 27 Hz; and blue, 31 Hz). The figure illustrates the relationship between the underlying Tulipan sill complex and the HTVCs seen on the HV1 surface.

The HTVC depth is essentially a measurement of the dome structural relief, made by defining a datum linked to the underlying HV1 horizon (Figure 3). Table 1 presents the sizes of the 13 individual HTVCs, showing sizes in the range of 70–120 m. The horizons above HV1 are characterized by a series of convex structures, which are described as draped mounded structures. The term "mounded structure" is used as a descriptive term in this paper to define the topographic relief of the dome above HV1 (Figure 5). To determinate the extent of these structures, the horizons were picked as a well-defined, high-amplitude, and continuous stratigraphic boundary, defined by the presence of the uppermost part of the convex-mounded reflections.

HTVCs are observed below mounding structures on the Top Tare horizon. They typically display sizes ranging from 600 to 2000 m in diameter and 70 to 120 m in height, with an elevated time ratio of 0.1 s (TWT). These mounded structures are exclusively observed in the Paleocene-Eocene transition zone and the lower part of the intra-Eocene interval. This interval is defined by a relatively abrupt decline in gamma and sonic response in well 6302/6-1 (Figure 2). In the stratigraphic completion log the interval is described as claystone with thin sandstone stringers with variable content of tuffaceous material. The sonic values in this interval could suggest a transition to more under-compacted and homogeneous clay-sandstone compositions beneath the tuff deposits.

Vent conduit zone

The vent conduit is interpreted as the disrupted, altered, or brecciated zone in which fluids and mobilized sediments migrated toward the paleosurface. The conduits are seen as disrupted reflections, resulting in a chaotic character of the originally stratified sedimentary host rocks. The 3D data show the conduits as vertical zones in the seismic data, where the amplitudes and reflections are distorted (Figures 3 and 5), consistent with earlier work in the basin and elsewhere (Heggland, 1998).

The conduit zones show variable morphologies. Some are conical and become thinner downwards toward the sill tip, whereas others display cylindrical morphologies. Not all the conduit zones display a traceable path from the dome down to their origin. In cases where the flow pattern is diverted by displaced fault blocks or magmatic bodies, the prediction of the sill and aureole origin is difficult. However, in general, the conduits do not appear to follow fault planes, and systematic fault cutting is not observed.

In the cases in which the conduit zones and the links to sills are uncertain, it might be a result of seismic imaging and detection problems. The overburden might also play a role in the interpretation. High-amplitude reflections may mask the underlying strata or create seismic artifacts by obscuring the underlying reflections (Schroot and Schüttenhelm, 2003). Reflections in the surrounding host strata are often seen to dip toward the conduit zone and the upper part of the HTVC. This feature is best observed in the seismic section crossing large HTVCs.

Sandbox modeling results

Each of the experiments started with similar lithostatic stress conditions for the granular bedding in the Hele-Shaw cell (Figure 8). Compressed air from a pressurized tank was gradually imposed through the inlet by manually increasing the air flux using a valve. The pressure was increased slowly until the predefined supply pressure was reached, and the fluid-induced deformation of the matrix was obtained.

In experiments in which the simulated overburdens exceeded 9 cm, a static bubble formed on top of the inlet (Figure 8). The bubble did not change size (width or height) through time, at a given (constant) pressure. The presence of the static bubble also induced lateral compaction of the matrix, together with a moderate uplift resulting in two steeply dipping reverse shear bands on each side of the inlet (Figure 8, t3 and t4). The dip angle and diameter of the conical reverse shear bands are influenced by the filling height, with increasing values for additional material filling. When further increasing the pressure to values beyond the equilibrium threshold, the bubble rapidly moved toward the surface initiating the fluidization.

Fluidization is characterized by rapid upward transport of the grains together with the ascending bubble. This transport enables convective movement aligned with the inlet and at the center of the structure. This convective flow generated inward dipping beds at both sides of the fluidization zone. The concentration of fluidized deformation was centralized within the reverse shear bands. At the surface above the fluidization zone, crater deposits formed as grains were erupted (Figure 9).

We have compared the results from the Hele-Shaw cell with those from the seismic interpretation. Although HTVCs are symmetrical 3D structures and the sandbox experiment resulted in 2D-confined structures, the cor-
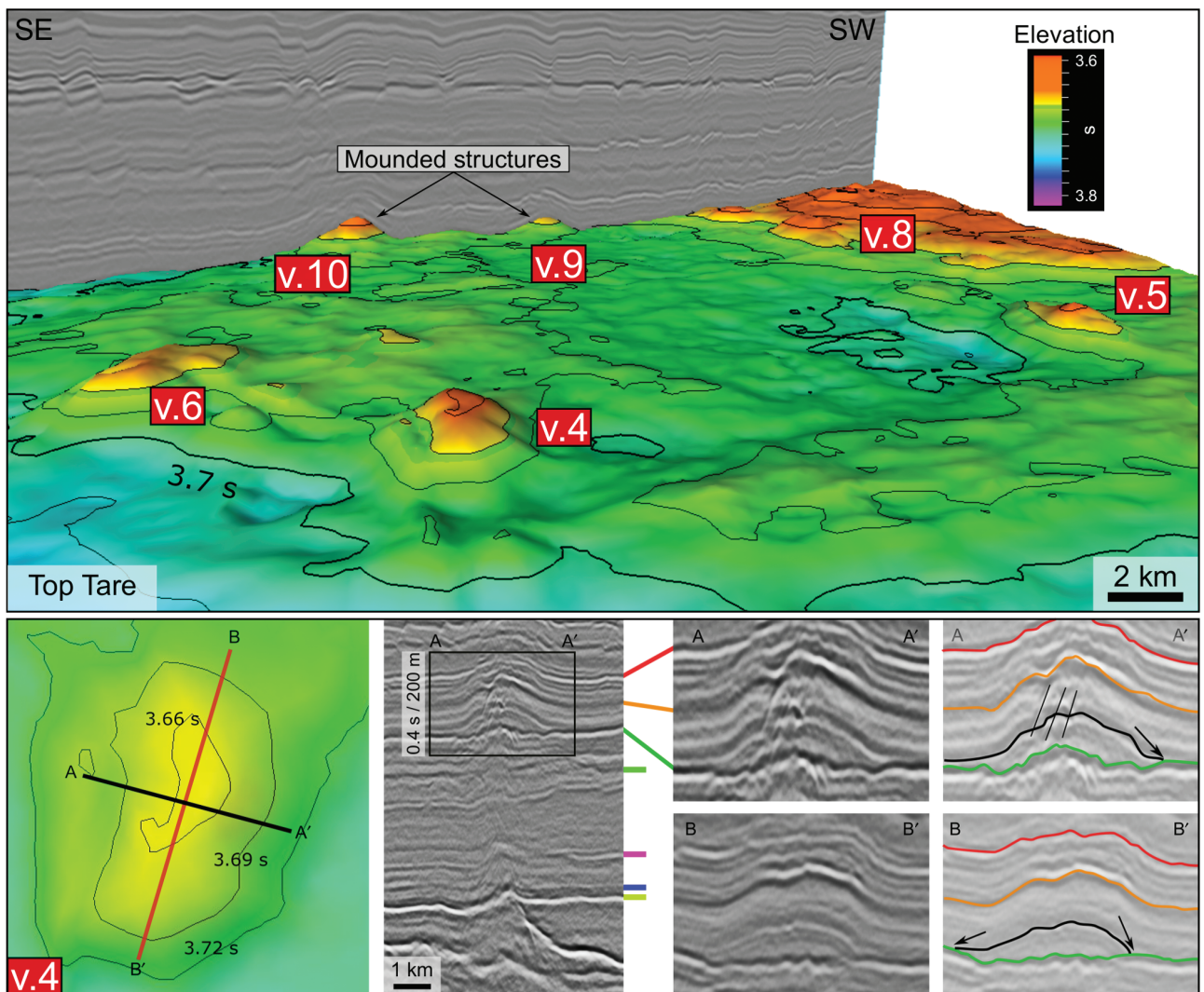
Figure 5. Perspective view of the intra-Eocene (lower) horizon Top Tare and a seismic crossline section of the representative mounded structures of the HTVCs. The seismic section below displays the HTVC v.4. Note that the structure is restricted between the intervals of the Paleocene-Eocene (between the sill tip at the Base Carbonate layer and the dome at Top Tare).
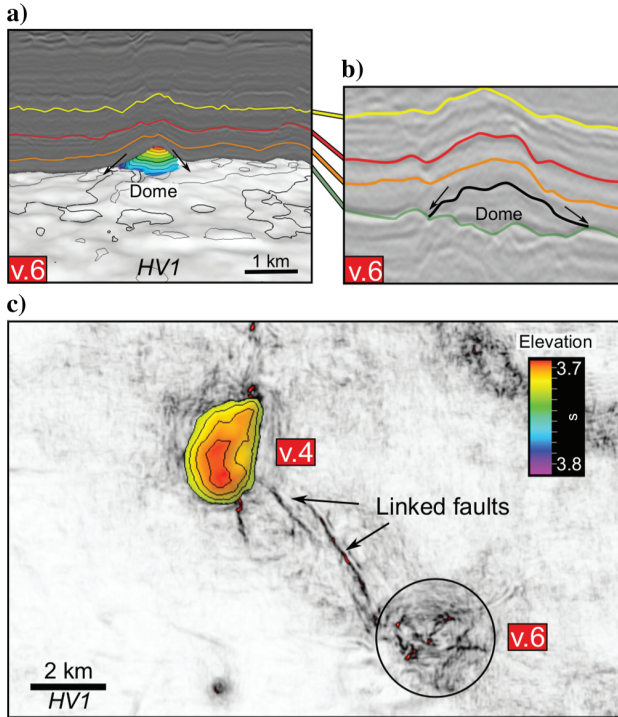
Figure 6. (a) 3D seismic interpretation of the v.6 dome structure, down-lapping onto the HV1 horizon. (b) Corresponding 2D projection of the v.6 dome structure. (c) "Variance cube" slice from the HV1 horizon seen from above. This figure illustrates the 3D mapped and time-slice variance representation of domes v.4 and v.6. The variance cube highlights lateral discontinuities such as faults. The fault pattern away from both vents suggests development simultaneous to the vents formation.

Table 1. List summarizing the measured parameters for the 13 HTVCs mapped in this study.

HTVC nr.	Major width (m)	Minor width (m)	Dome height (m)	Conduit height (m)
1	1400 ± 100	1200 ± 100	100 ± 20	400
2	950 ± 150	600 ± 100	70	200
3	1650 ± 100	1400 ± 100	90	320
4	2100 ± 50	1800 ± 100	100	640
5	2500 ± 100	N/A	120 ± 50	400
6	1850 ± 50	1350 ± 100	80	630
7	1600 ± 100	N/A	100 ± 30	630
8	1200	N/A	N/A	530
9	1200 ± 20	650 ± 20	85	500
10	1570	1150	90	450
11	300 ± 50	N/A	120	400
12	1000 ± 30	600 ± 30	80	500
13	1500 ± 50	1350 ± 50	85	650

Note: See Figure 4 for the location of the individual complexes in which the specific part of the HTVCs could not be measured with confidence, and N/A (not available) is entered in the table.

relation between basic parameters such as height, width, and length is still valid. Figure 10 shows similarities between the upper part of the HTVCs and the upper part of the sandbox structures. The plots indicate how crater/dome structures scale approximately linearly with the
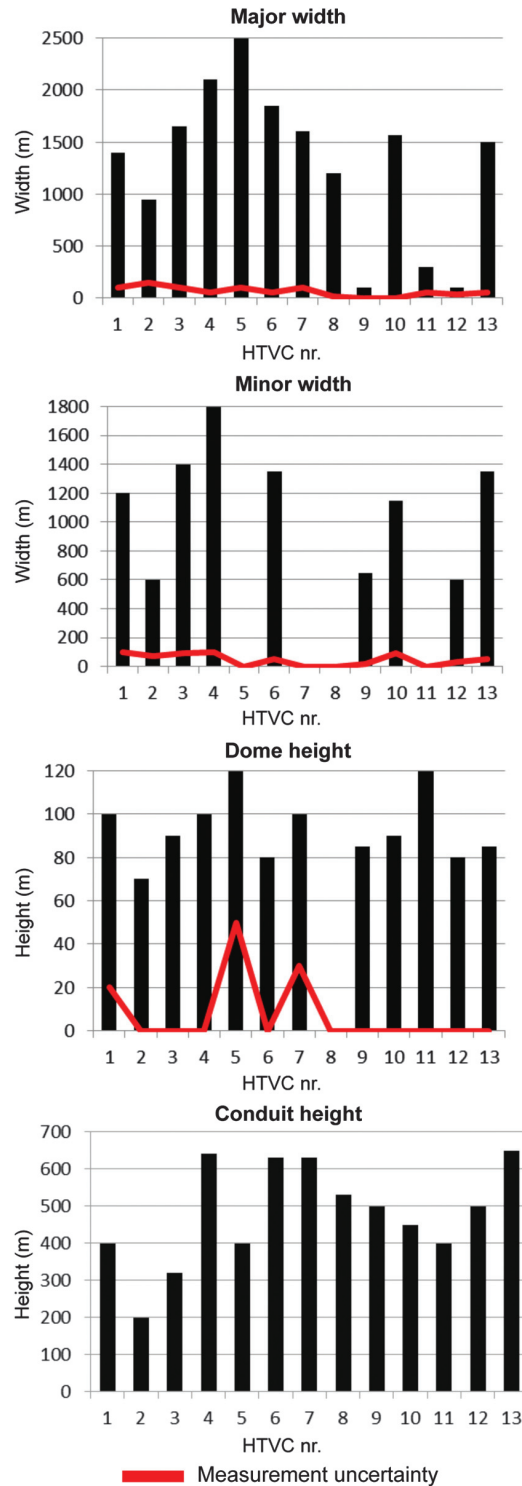
Figure 7. Bar diagram showing the dome sizes for the measured HTVCs in Table 1.

conduit/filling height ratio. This is a trend that is also obtained from the seismic data, in which taller conduit zones are associated with larger surface (Table 1). Although a linear correlation may not represent the best fit in terms of the actual HTVCs, the height/width dependency is significant. Therefore, the sandbox models capture first-order features of the natural HTVC.

Seismic modeling

By estimating a simple overburden model and taking into account the combination of survey/migration aperture, we can retrieve and highlight the illuminated reflections at a given depth interval and reference point (Lecomte et al., 2015). In practice, the illumination of the target depends on the survey geometry and the wave propagation in the overburden, and it will also vary according to the location of the target (lateral and depth). Our seismic modeling allowed for direct control of what would be the maximum dip illuminated at the target, i.e., all reflection dips between the horizontal dip and the maximum dip imaged (Lecomte et al., 2016). Therefore, three maximum illuminated dips were tested during the seismic modeling procedure (25°, 45°, and 90°), corresponding to limited, reasonable, and perfect (ideal) survey/migration apertures, respectively (Figure 11).

The synthetic model was able to capture complex features of the piercement structure and produce realistic geometries and deformation fields. Although the differences between 25° and perfect (90° max dip) illumination may be subtle, there are differences due to resolution and geometric effects. From the 25° max dip, features exceeding the 25° incline angle will disappear in the seismogram (black arrows in Figure 11). In addition, the disrupted conduit zone appears as blurry and transparent in the seismogram compared with the 45° and perfect illumination. This observation supports that a narrow survey aperture prohibits steeper reflections to be illuminated compared with a wide aperture. The 45° corresponds to symmetrical illumination of the modeling. Angles exceeding 45° max dip are not illuminated in the seismogram. Note that the steeper dipping reflections in the conduit zone seem to have a more lateral and continuous extension. When comparing the conduit interior between the 45° and the perfect illumination, the latter is slightly improved with respect to reflection strength.

Discussion

The hydrothermal vent complexes provide evidence for focused fluid and gas migration in the Møre Basin close to the Paleocene-Eocene transition. A few questions arise from our mapping, including aspects of the detailed interpretation of the seismic data and the age of the HTVCs. The key to these questions can be constrained by examination of the seismic and stratigraphic data, and the experimental and synthetic modeling. The discussion below focuses on the HTVCs as one complete system, including morphology, formation mechanisms, and age correlations.

Dome shape and differential compaction model

A characteristic feature associated with the explosive volcanism of hydrothermal venting is the formation of craters (Nermoen et al., 2010; Haug et al., 2013; Galland et al., 2014). The opposite is found regarding the HTVCs interpreted in the 3D cube, i.e., domes and not craters. The formation of HTVCs at the HV1 horizon shows a characteristic down-lapping dome structure on the paleosurface defining the upper part (Figure 6).
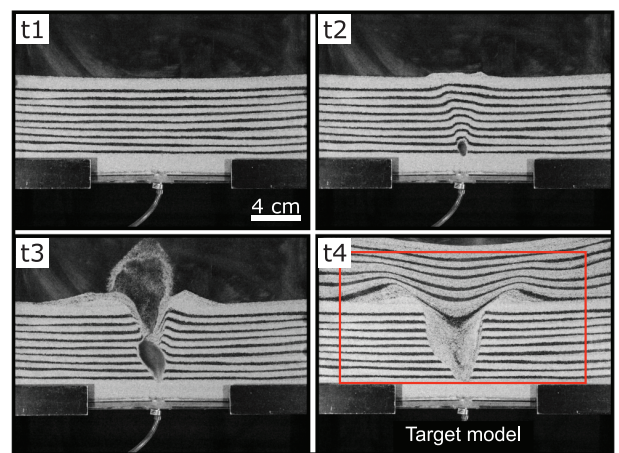

Figure 8. Time-lapse sequence of sandbox experiment. (t1): Initial configuration of the static bedding. (t2): Static bubble forming at the centered inlet, fluid-induced deformation of the matrix. (t3): The gas bubble grows to the surface, triggering the onset of fluidization and eruption of material at the structure rim and crater. (t4): Resedimentation of piercement structure, material funnel fed after experiment.
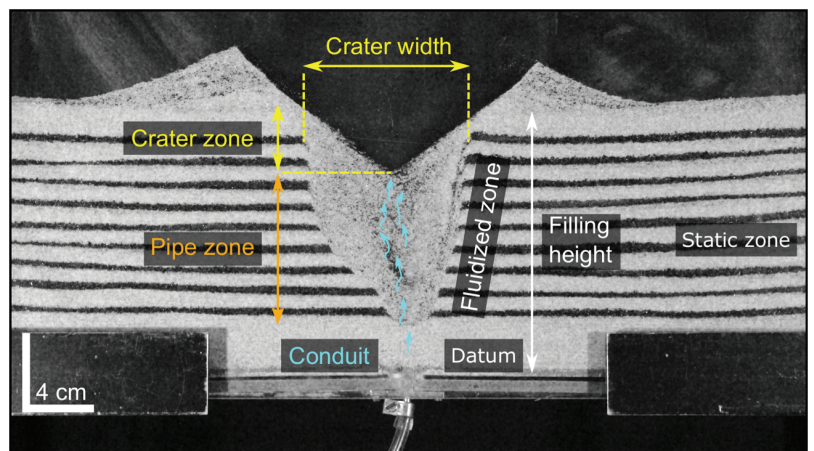

Figure 9. Morphological zones defined in the experiment, which enable a correlation to the natural occurring HTVCs.

Differential compaction is a mechanism that may explain the doming above the HTVCs.

All materials will compact due to gravitational stresses when loaded. Differential compaction develops, for instance, in inhomogeneous sedimentary deposits, in which the material properties vary (Miles and Cartwright, 2010; Jackson, 2012; Zhao et al., 2014). Variation in how the different materials behave during this process is dependent on their composition and porosity. The result can be seen as local areas compacting more than others, and that geologic structures may be affected geometrically during compaction stresses (Figure 12). This process has previously been described in terms of the upper vent geometry by Skogseid et al. (1992) and Planke et al. (2005), in which it was considered as a possibility for the vent-fill to compact less than the surrounding strata, thus, causing the characteristic dome morphology.

The presence of long-lived seepage through vents from underlying strata (Svensen et al., 2003; Iyer et al., 2013) could also have contributed to the reduced compaction of the vent structure. If these fluids migrated and were trapped in the upper vent structure by the deposition of overlying sealing sediments, overpressure could have developed, which in turn may have inhibited further compaction.
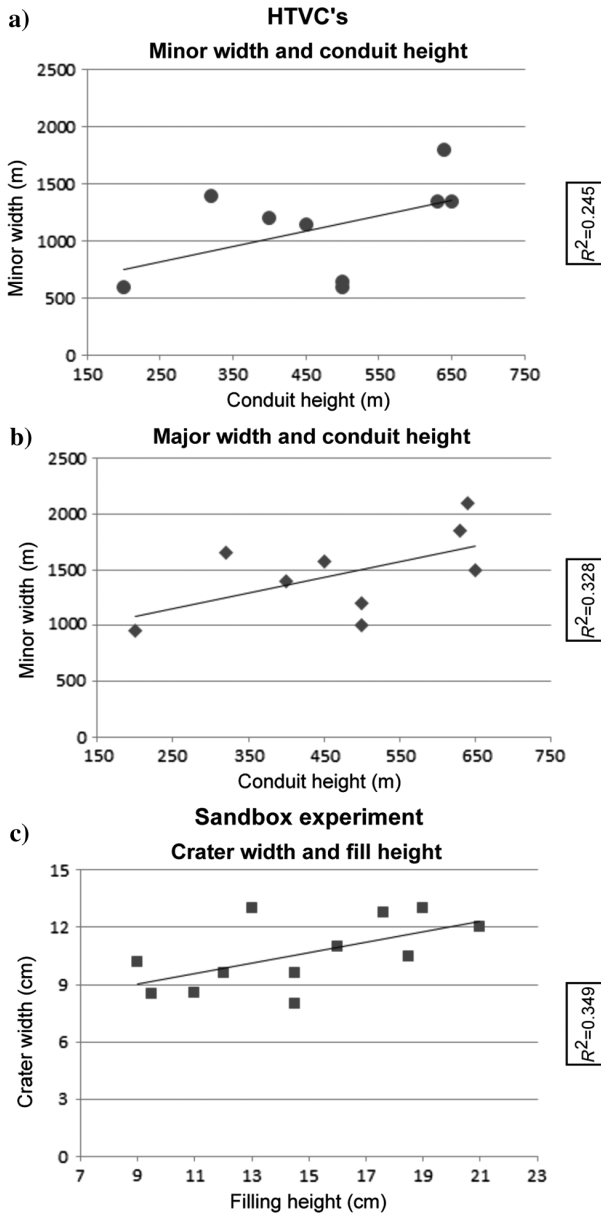
Figure 10. Comparison plot between HTVCs and piercement structures in the sandbox experiment: (a) Minor width plotted against the conduit height. (b) Major width plotted against the conduit height. (c) Crater width plotted against filling height (in a sandbox experiment).
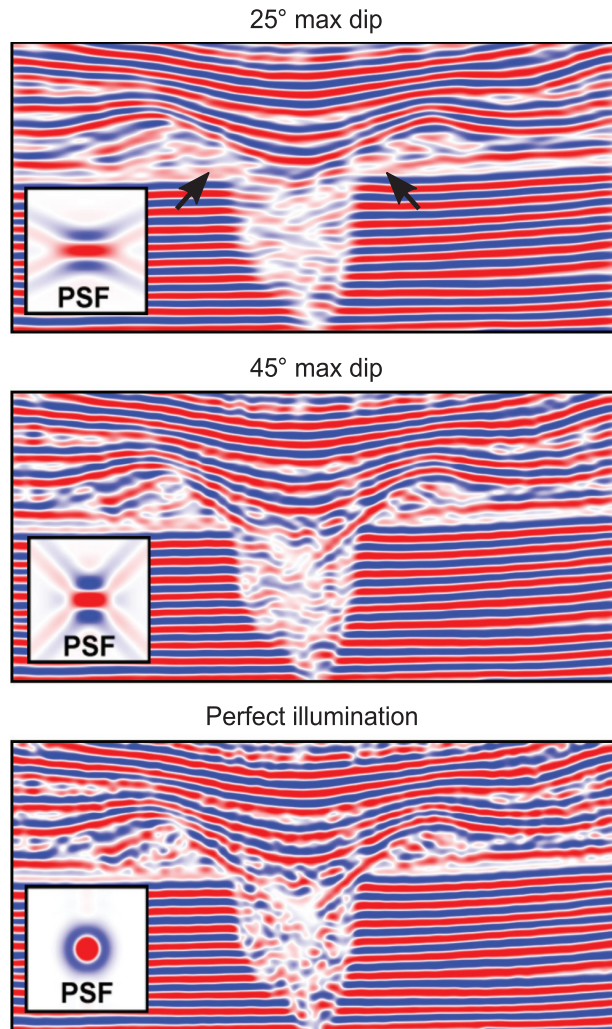
Figure 11. Synthetic seismic modeling of a model derived from the sandbox experiment. Elastic properties based on well 6302/6-1 at the HTVC interval. Arrows in the uppermost figure highlight how different reflection dips are affected by seismic imaging.

HTVC formation and the sandbox experiment

It is clear that the HTVCs result from focused fluid flow to generate the structural features seen in the seismic data. We have identified similarities when comparing seismic cross sections of HTVCs with the sandbox experiments (Figures 3 and 9). When fluid pressure was increased beyond the equilibrium threshold, fracturing and brecciating developed above the source. The fluidized zone in the sandbox experiment acted as the conduit zone in the natural setting, a pathway for fluids to reach the surface. The fluidization in the sandbox experiment developed two regions where the first consisted of a narrow conduit zone and the second an upper crater zone (Figure 9). These two morphological features can be correlated to the upper and lower parts of the HTVCs (see Jamtveit et al., 2004; Planke et al., 2005).

Field data show that the HTVCs contain brecciated sedimentary rocks with lithologic differences compared with the surrounding strata (Jamtveit et al., 2004; Svensen et al., 2006). Similar findings are evident from the conduit zone in the sandbox experiment. Moreover, the field observations, and seismic and experimental data show well-developed inward dipping strata toward the conduit zone (Planke et al., 2003; Svensen et al., 2006). The experiment time-lapse photographs of Figure 8 show convective flow during material transport, resulting in volume reduction followed by collapse and the generation of inward dipping beds.

The main difference between the sandbox models and the seismic data are the shallow structures: The sandbox exhibits well-developed crater morphology above the in-filled fluidized conduit zone, whereas HTVCs interpreted in the 3D cube exhibit domes. As mentioned earlier, we interpret these domes as a result of differential compaction, a process that cannot be modeled in the sandbox.

Synthetic seismic

Synthetic modeling emphasizes the importance of internal structures in generating seismic amplitude anomalies. Figure 11 shows a comparison between the different modeling runs. Even though the resulting seismic images
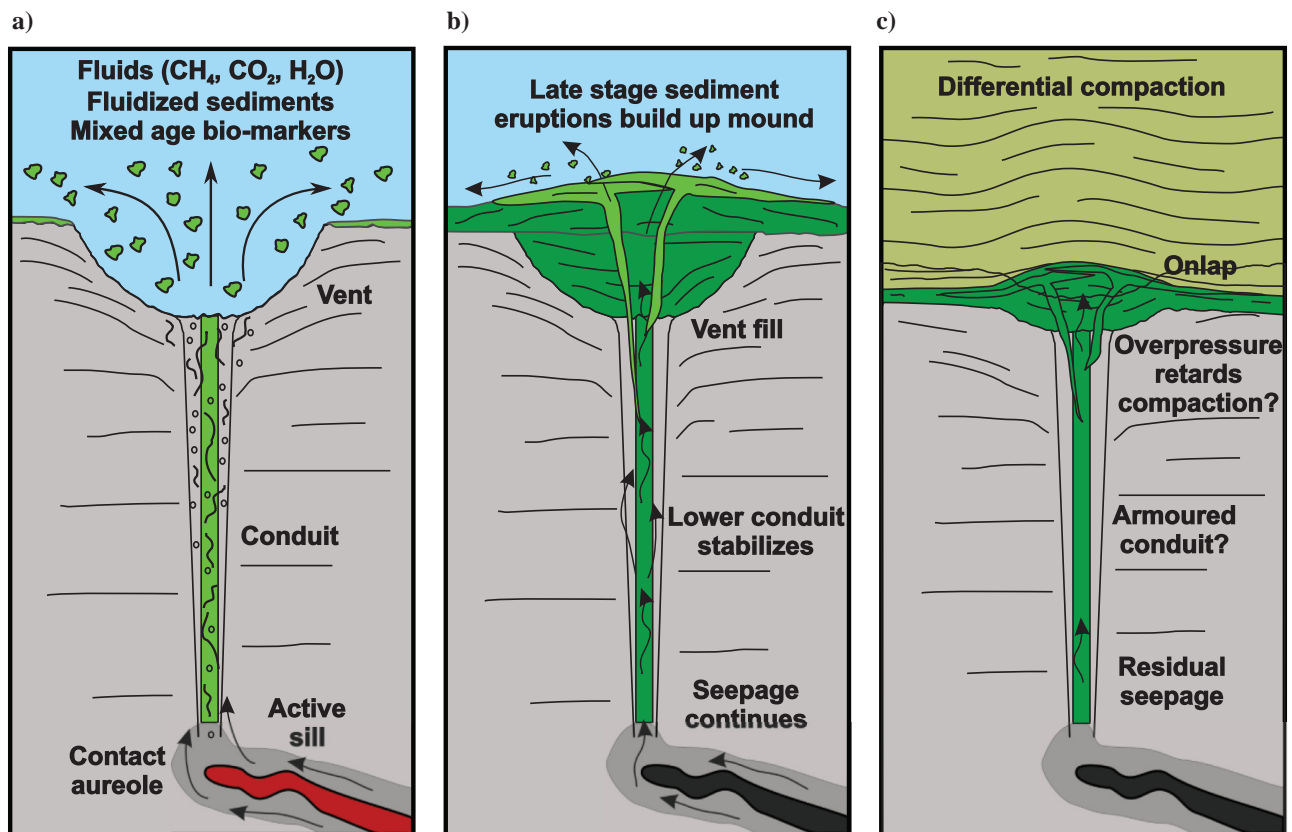

Figure 12. Schematic model displaying key development stages during vent formation. (a) Emplacement of intrusion promotes fluid generation and overpressure causing overburden failure and explosive hydrothermal venting, which blankets the surrounding area with vent material and older sediments. Large volumes of carbon out gassed into the water column and atmosphere. (b) After the initial high-energy venting, activity gradually wanes with long-lived gas seepage occurring over many thousands of years and periodically promoting small-scale sediment eruptions, which fill the crater and build up a shallow angle dome. (c) Post venting sedimentation blankets the dome and builds up a potentially sealing cover over thousands to millions of years. Compaction of surrounding strata may exceed that of the hardened or potentially over-pressured vent material resulting in differential compaction and the accentuation of the dome feature.

produced are generically similar, there are clear structural differences. One of the most prominent characteristics when comparing the 25°–45° max dip is how the reflections in the images are displayed (Figure 13). By widening the survey distance and migration aperture in the model, steeper reflection dips at a given reference point are obtained. Perfect illumination has the widest survey/migration aperture, and 25° is the narrowest. Comparing the seismic and the synthetic section, the near-horizontal reflections are displayed properly, but this is not the case for the dipping reflections. The combination of the survey aperture and layer dip makes for two different structural interpretations of the seismograms. When comparing these results to the actual seismic section of the HTVCs, we find that the dipping reflections in the conduit zone rarely exceed c. 45°–50°. From the seismic modeling, we found out that 45° max illumination dip was reasonable for the considered overburden model and a standard migration aperture value. This may imply that the processed data are unable to properly visualize reflections above this angle. A reasonable maximum illuminated dip is taken to be approxi-

mately 45°, and it seems to fit between our modeling estimation and what is observed on the actual images.

A direct implication of this is that strongly dipping structural features within the HTVCs can be overlooked or misinterpreted (Figure 13). The synthetic modeling thereby provides a method for more confident interpretations of geologic features, plus the ability to validate seismic attributes and artifacts to avoid pitfalls and misinterpretations.

Age and evolution of the Møre Basin vent complexes

Age determination of the HTVCs in this study is based on the seismic interpretation, well-tie correlations and published palynological data focusing on the sediments at the upper HTVC interval. The interval between the HV1 and HV3 horizons represents the development and emplacement of the HTVCs. These observations include the intrusive nature of the conduit zone below this transition zone, down-lapping domes, radial faults and tuffaceous claystone at the paleosurface of HV1. From the well data and check shots, the measured depth of this
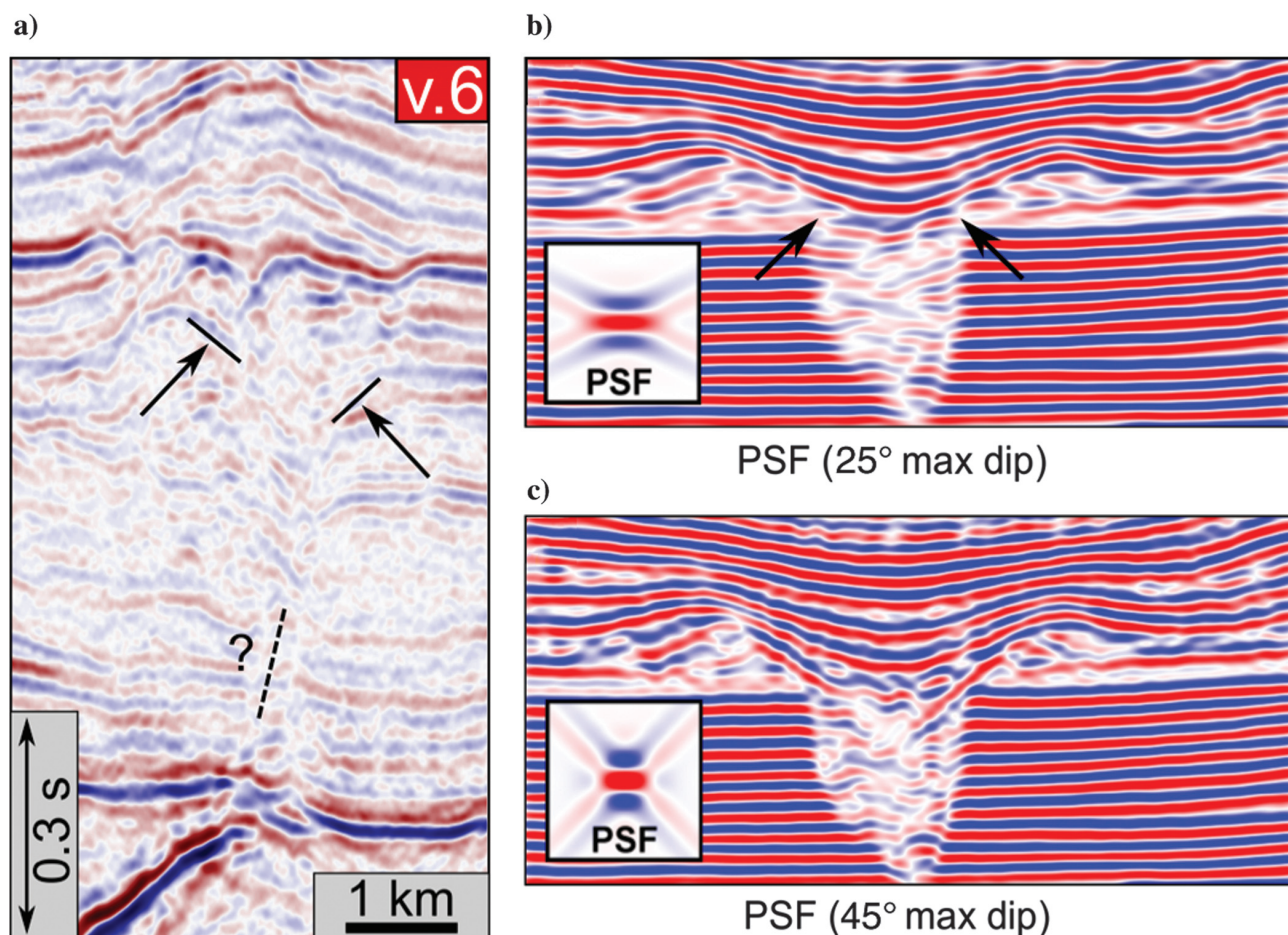

Figure 13. (a) HTVC (v.6) seismic section, illustrating how the dipping reflections are displayed in the image, and the uncertainty that follows with steeper dipping reflections. (b) 25° max dip illumination in the seismogram. Restricted illuminated reflections greater than 25°. The black arrows indicate structural differences between the two angel-dependent models. (c) 45° max dip illumination in the seismogram. The dominant frequency of the seismic is 20 Hz.

interval is correlated to be between 3350 and 3450 m (Figures 14 and 15).

The biostratigraphic evidence from this transition zone comprises a somewhat enigmatic assemblage with mixed-age biostratigraphic indicators between the clear signatures from the underlying Tang and overlying Tare Formations. Clear and clean occurrences of the dinocyst *Apectodinium augustum* are identified at 3350

a)

Sample depth (m)	TWT (s)	Key taxa	Palyno zones	Time scale	Fm	Age Ma
3090–3120	3.574–3.607	*Diphyes colligerum (LO)*	TP8A			41.30–ca. 42.80
3180	3.671	*Eatonicysta ursulae & Azolla spp.*	TP6D2		Brygge	50.02–ca. 50.10
3200–3220	3.688–3.704	*Dracodinium politum (LO)*	TP6B	Eocene		50.29–ca. 50.50
3240–3250	3.725–3.733	*Deflandrea oebisfeldensis (LO)*	TP5B4		Tare	51.50–53.61
3270–3330	3.750–3.800	*Cerodinium wardenense*	TP5B2			54.60–54.70
3350–3400	3.820–3.862	*Apectodinium augustum*	TP5A		TZ	54.90–55.80
3450–3570	3.902–4.003	*Glaphyrocysta 'oligacantha'*	TP3B3	Paleocene	Tang	57.40–57.90

b)
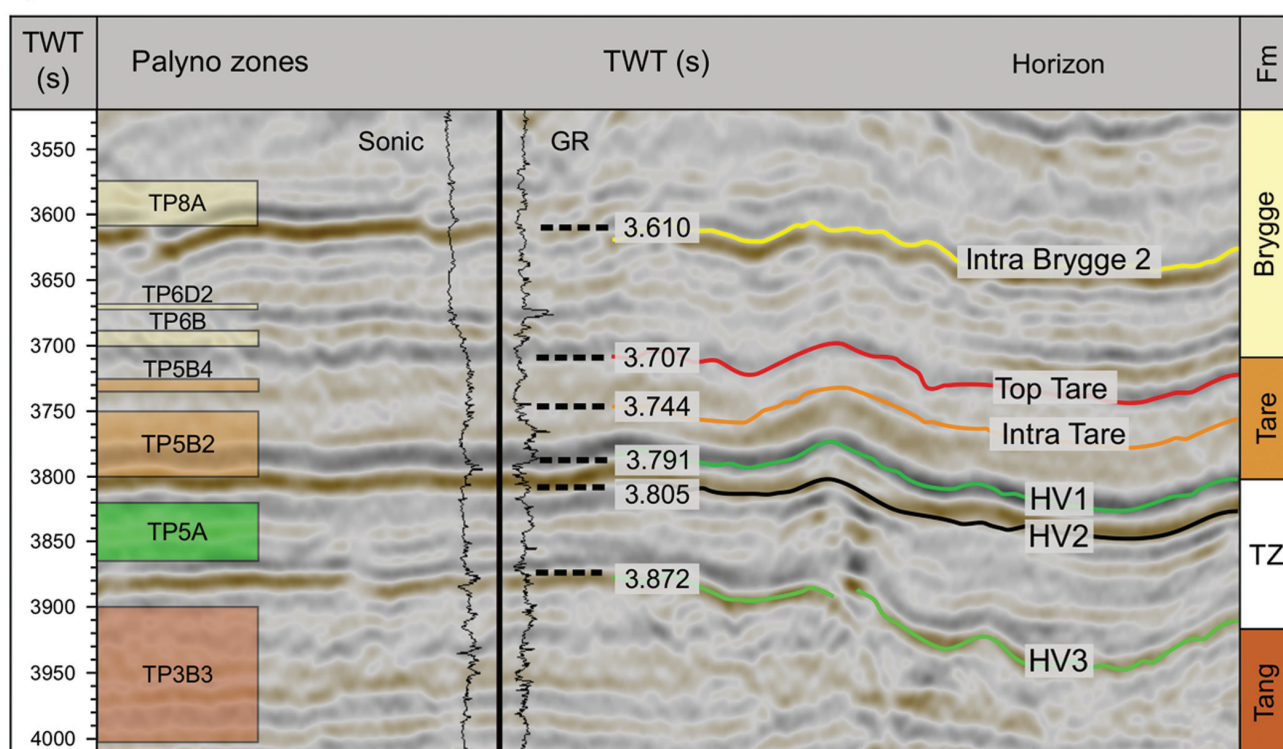
Figure 14. Summary of biostratigraphic age constraints of the venting interval. (a) Table showing the key taxa distributions correlated with relative age and horizons interpreted at the HTVC interval. Palynozones correspond to taxa distribution at given time stages. (b) Seismic section and taxa resolution of the HTVC interval. Depth of the seismic horizons calibrated with check-shot data from well 6302/6-1.

and 3390 m (last natural occurrence, LO in the well) which suggests that the interval most likely comprises the TP5A zone of the Earliest Eocene (Figure 14). This species is widely used as a marker species for the Paleocene-Eocene transition (Ali and Jolley, 1996; Schmitz et al., 2004; Sluijs et al., 2006; Passey and Jolley, 2009). Classification of the interval is complicated by the occurrence of older Paleocene palynomorphs (e.g., Tang markers such as *Alisocysta margarita*, *Palaeoperidinium pyrophorum*, *Areoligera gippingensis*, *Spiniferites "membranispina"*; note that these did not occur in the expected order) along with the frequent occurrence of Cretaceous fossils like *Sidridinium borealis*, "ancient" bisaccates, and Upper Triassic *Ricciisporites tuberculatus*. The interval may therefore represent the upper parts of the Tang Formation with abundant caving from zone TP5A, or alternatively in situ TP5A with reworking from Tang and older formations. The mixed nature of the assemblage supports significant reworking within the interval, and therefore the clear occurrences of *A. augustum* are used to support an Earliest Eocene (54.9–55.8 Ma) age for the transition zone and therefore the HTVC development within the Møre Basin study area (Figure 14).

A wide range in thermal maturity of the retrieved fossils is documented from the transition zone suggesting a source near the sill. For instance, some of the Cretaceous and older reworked fossils are almost black in 3410–3440 m. Tuffaceous material was also identified within the interval. Along with the high temperature signatures, older sediments and volcanic detritus indicate that local and basin-wide eruptions, causing plumes of mixed age sedimentary rocks along with their biomarkers (Schofield et al., 2015), could have contributed to the mixed assemblages of the transition zone at this time.

Paleocene-Eocene thermal maximum

The HTVC formation coincides with one of the most extreme transient shifts in climate during the Cenozoic. The PETM occurred at approximately 56 Ma and lasted between 100 and 200 kyr (Norris and Röhl, 1999; Westerhold et al., 2009). This event is associated with a significant temperature rise of the oceans and the atmosphere, together with changes in ocean chemistry and extinction of benthic foraminiferal species traceable in the biostratigraphical record (Kennett and Stott, 1991; Röhl et al., 2000; Röhl et al., 2007).

The PETM is coeval with the initial opening of the northeast Atlantic Ocean (Storey et al., 2007), which has been linked to magma emplaced in the Møre Basin (Svensen et al., 2004; Frieling et al., 2016). Although no direct evidence for contact aureoles have been identified during the seismic interpretation, contact metamorphism around sills is well understood and led to the generation of CH_4, CO_2, and H_2O from heating of organic-bearing sedimentary rocks (Aarnes et al., 2015). Vent complex statistics from the Møre and Vøring Basins by Planke et al. (2005) indicate that potentially thousands of individual HTVCs formed within the PETM and may have acted as one of the main sources for carbon (Svensen et al., 2004). Sedimentary basins influenced by large igneous provinces may thus represent settings characterized by rapid release of carbon-bearing gas.
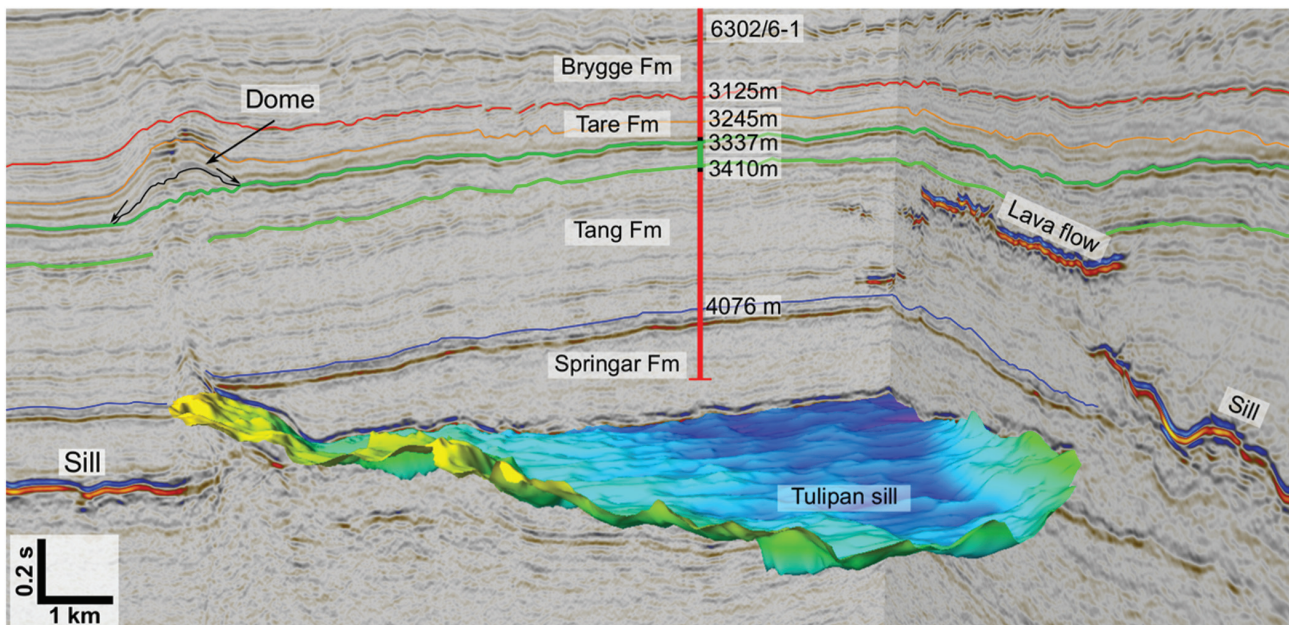

Figure 15. Figure summarizing different data implemented to resolve the key questions regarding the HTVCs in the Møre Basin. The investigation focus on (1) the vent complex geometries, (2) the induced surface deformation patterns, (3) the intrusions (heat source) relation, as well as (4) the emplacement depth and age of the hydrothermal vent complexes.

Conclusions

Seismic mapping in the Møre Basin offshore mid-Norway has documented an extensive hydrothermal vent complex of Paleocene-Eocene age. Thirteen individual vent complexes have been mapped within the 310 km^2 large study area. All the observed venting structures are located above sill intrusions and are therefore assumed to have developed as a direct consequence of sill emplacement and contact metamorphism. The complex architecture of the HTVCs may be explained by mobilization of sedimentary rocks from above the sills, caused by local fluid overpressure and fluid migration. The HTVCs were formed primarily during explosive eruption of gases, liquids, and sedimentary rocks, resulting in depressions and craters at the seafloor. The upper parts of the HTVCs are dominated by domes and mounded features measuring up to 2.5 km in diameter and 120 m in height. The upper parts of the vent complexes terminate consistently at the Paleocene-Eocene transition above the Tang Formation. This study has used state-of-the-art methods to produce unique 3D images of seismic reflection data together with simulated modeling to map out the HTVCs within the Møre Basin. The methods used demonstrate how the final analyses can provide new images of sediment deformation and fluid/gas migration patterns using 3D seismic and modeling procedures. Combining these makes it possible to recognize geometries with considerable confidence, along with mapping important relationships between fluid-flow pathways and structural behavior with high precision.

By implementing well-tie correlations and biostratigraphical analysis, the ages of these structures are within the 54.9–55.8 Ma range. This period is characterized by intrusive events during the initial volcanism phase at the mid-Norwegian margin, corresponding to the northeast Atlantic breakup. The hydrothermal vent complexes were likely active for a substantial time period in the earliest Eocene. The vent formation likely corresponds to a c. 100 m thick Tang/Tare transition zone with *A. augustum* and reworked Cretaceous and older fossils displaying high maturities possibly caused by contact metamorphism. The timing of the HTVCs coincides with one of the most extreme climatic shifts in the Cenozoic, the PETM, and our data and conclusions stress the link between the generation and release of carbon gases from the Møre Basin and the global environmental change.

REFERENCES

Aarnes, I., S. Planke, M. Trulsvik, and H. Svensen, 2015, Contact metamorphism and thermogenic gas generation in the Vøring and Møre basins, offshore Norway, during the Paleocene–Eocene thermal maximum: Journal of the Geological Society, **172**, 588–598, doi: 10.1144/jgs2014-098.

Aarnes, I., H. Svensen, J. A. Connolly, and Y. Y. Podladchikov, 2010, How contact metamorphism can trigger global climate changes: Modeling gas generation around igneous sills in sedimentary basins: Geochimica et Cosmochimica Acta, **74**, 7179–7195, doi: 10.1016/j.gca.2010.09.011.

Ali, J. R., and D. W. Jolley, 1996, Chronostratigraphic framework for the Thanetian and lower Ypresian deposits of southern England: Geological Society, London, Special Publications 101, 129–144.

Bell, B., and H. Butcher, 2002, On the emplacement of sill complexes: Evidence from the Faroe-Shetland Basin: Geological Society, London, Special Publications 197, 307–329.

Berndt, C., C. Hensen, C. Mortera-Gutierrez, S. Sarkar, S. Geilert, M. Schmidt, V. Liebetrau, R. Kipfer,, F. Scholz, M. Doll, S. Muff, J. Karstens, S. Planke, S. Petersen, C. Böttner, W.-C. Chi, M. Moser, R. Behrendt, A. Fiskal, M. A. Lever, C.-C. Su, L. Deng, M. S. Brennwald, and D. Lizarralde, 2016, Rifting under steam—How rift magmatism triggers methane venting from sedimentary basins, Geology, **44**, 767, doi: 10.1130/G38049.1.

Brekke, H., 2000, The tectonic evolution of the Norwegian Sea continental margin, with emphasis on the Vøring and Møre basins: Special Publication-Geological Society of London, **167**, 327–378.

Dalland, A., D. Worsley, and K. Ofstad, 1988, A Lithostratigraphic scheme for the Mesozoic and Cenozoic and succession offshore Mid-and Northern Norway: Oljedirektoratet.

Deagan, C., and B. Scull, 1977, A proposed standard lithostratigraphic nomenclature for the Central and Northern Sea: Annual Report: Institute of Geological Sciences, Report no. 77/25: Bulletin NPD, no. 1.

Doré, A. G., E. R. Lundin, L. N. Jensen, Ø. Birkeland, P. E. Eliassen, and C. Fichler, 1999, Principal tectonic events in the evolution of the northwest European Atlantic margin: Geological Society of London, Geological society, London, petroleum geology conference series 5, 41–61.

Faleide, J. I., F. Tsikalas, A. jBreivik, R. Mjelde, O. Ritzmann, O. Engen, J. Wilson, and O. Eldholm, 2008, Structure and evolution of the continental margin off Norway and the Barents Sea: Episodes, **31**, 82–91.

Frieling, J., H. H. Svensen, S. Planke, M. J. Cramwinckel, H. Selnes, and A. Sluijs, 2015, Thermogenic methane release as a cause for the long duration of the PETM, 2015 AGU Fall Meeting, Agu.

Frieling, J., H. H. Svensen, S. Planke, M. J. Cramwinckel, H. Selnes, and A. Sluijs, 2016, Thermogenic methane release as a cause for the long duration of the PETM: Proceedings of the National Academy of Sciences 12059–12064, doi: 10.1073/pnas.1603348113.

Galland, O., G. R. Gisler, and Ø. T. Haug, 2014, Morphology and dynamics of explosive vents through cohesive rock formations: Journal of Geophysical Research, 119, 4708–4728, doi: 10.1002/2014JB011050.

Gernigon, L., J. C. Ringenbach, S. Planke, B. Le Gall, and H. Jonquet-Kolstø, 2003, Extension, crustal structure and magmatism at the outer Vøring Basin, Norwegian margin: Journal of the Geological Society, 160, 197–208, doi: 10.1144/0016-764902-055.

Gibb, F., and R. Kanaris-Sotiriou, 1988, The geochemistry and origin of the Faeroe-Shetland sill complex: Geological Society, London, Special Publications 39, 241–252.

Grapes, R., 2010, Pyrometamorphism: Springer Science & Business Media.

Grove, C., 2013, Submarine hydrothermal vent complexes in the Paleocene of the Faroe-Shetland Basin: Insights from three-dimensional seismic and petrographical data: Geology, 41, 71–74, doi: 10.1130/g33559.1.

Hansen, J., J. Cartwright, M. Huuse, and O. R. Clausen, 2005, 3D seismic expression of fluid migration and mud remobilization on the Gjallar Ridge, offshore mid-Norway: Basin Research, 17, 123–139, doi: 10.1111/j.1365-2117.2005.00257.x.

Haug, Ø. T., O. Galland, and G. R. Gisler, 2013, Experimental modelling of fragmentation applied to volcanic explosions: Earth and Planetary Science Letters, 384, 188–197, doi: 10.1016/j.epsl.2013.10.004.

Heggland, R., 1998, Gas seepage as an indicator of deeper prospective reservoirs: A study based on exploration 3D seismic data: Marine and Petroleum Geology, 15, 1–9, doi: 10.1016/S0264-8172(97)00060-3.

Hjelstuen, B. O., O. Eldholm, and J. Skogseid, 1997, Vøring Plateau diapir fields and their structural and depositional settings: Marine Geology, 144, 33–57, doi: 10.1016/S0025-3227(97)00085-6.

Iyer, K., L. Rüpke, and C.Y. Galerne, 2013, Modeling fluid flow in sedimentary basins with sill intrusions: Implications for hydrothermal venting and climate change: Geochemistry, Geophysics, Geosystems, 14, 5244–5262, doi: 10.1002/2013GC005012.

Jackson, C. A.-L., 2012, Seismic reflection imaging and controls on the preservation of ancient sill-fed magmatic vents: Journal of the Geological Society, 169, 503–506, doi: 10.1144/0016-76492011-147.

Jamtveit, B., H. Svensen, Y. Y. Podladchikov, and S. Planke, 2004, Hydrothermal vent complexes associated with sill intrusions in sedimentary basins: Physical Geology

of High-Level Magmatic Systems, 234, 233–241, doi: 10.1144/GSL.SP.2004.234.01.15.

Kennett, J., and L. Stott, 1991, Abrupt deep-sea warming, palaeoceanographic changes and benthic extinctions at the end: Nature, 353, 225–229, doi: 10.1038/353225a0.

Lecomte, I., P. L. Lavadera, I. Anell, S. J. Buckley, D. W. Schmid, and M. Heeremans, 2015, Ray-based seismic modeling of geologic models: Understanding and analyzing seismic images efficiently: Interpretation, 3, SAC71–SAC89, doi: 10.1190/INT-2015-0061.1.

Lecomte, I., P. L. Lavadera, C. Botter, I. Anell, S. J. Buckley, C. H. Eide, A. Grippa, V. Mascolo, and S. Kjoberg, 2016, 2(3)D convolution modelling of complex geological targets beyond 1D convolution: FB Special Topic, no. First Break 34, 64–72.

Magee, C., C. A.-L. Jackson, and N. Schofield, 2014, Diachronous sub-volcanic intrusion along deep-water margins: Insights from the Irish Rockall Basin: Basin Research, 26, 85–105, doi: 10.1111/bre.12044.

Miles, A., and J. Cartwright, 2010, Hybrid flow sills: A new mode of igneous sheet intrusion: Geology, 38, 343–346.

Mosar, J., E. A. Eide, P. T. Osmundsen, A. Sommaruga, and T. H. Torsvik, 2002, Greenland–Norway separation: A geodynamic model for the North Atlantic: Norwegian Journal of Geology, 82, 281–298.

Nermoen, A., O. Galland, E. Jettestuen, K. Fristad, Y. Podladchikov, H. Svensen, and A. Malthe-Sørenssen, 2010, Experimental and analytic modeling of piercement structures: Journal of Geophysical Research: Solid Earth, 115, 1–15, doi: 10.1029/2010JB007583.

Norris, R. D., and U. Röhl, 1999, Carbon cycling and chronology of climate warming during the Palaeocene/Eocene transition: Nature, 401, 775–778, doi: 10.1038/44545.

Passey, S. R., and D. W. Jolley, 2009, A revised lithostratigraphic nomenclature for the Palaeogene Faroe Islands Basalt group, NE Atlantic Ocean: Earth and Environmental Science Transactions of the Royal Society of Edinburgh 99, 127–158, doi: 10.1017/S1755691009008044.

Planke, S., T. Rasmussen, S. Rey, and R. Myklebust, 2005, Seismic characteristics and distribution of volcanic intrusions and hydrothermal vent complexes in the Vøring and Møre basins: Geological Society of London, Proceedings Geological Society, London, Petroleum Geology Conference series 6, 833–844.

Planke, S., H. Svensen, M. Hovland, D. A. Banks, and B. Jamtveit, 2003, Mud and fluid migration in active mud volcanoes in Azerbaijan: Geo-Marine Letters, 23, 258–268. doi: 10.1007/s00367-003-0152-z.

Planke, S., H. Svensen, R. Myklebust, S. Bannister, B. Manton, and L. Lorenz, 2015, Geophysics and remote sensing: Advances in Volcanology, IAVCEI: Springer International Publishing.

Röhl, U., T. Bralower, R. Norris, and G. Wefer, 2000, New chronology for the late Paleocene thermal maximum and its environmental implications: Geology, 28, 927–930, doi: 10.1130/0091-7613(2000)28<927:ncftlp>2.0.co;2.

Röhl, U., T. Westerhold, T. J. Bralower, and J. C. Zachos, 2007, On the duration of the Paleocene-Eocene thermal maximum (PETM): Geochemistry, Geophysics, Geosystems, **8**, doi: 10.1029/2007GC001784.

Schmiedel, T., S. Kjoberg, S. Planke, C. Magee, O. Galland, N. Schofield, C. A.-L. Jackson, and D. A. Jerram, 2017, Mechanisms of overburden deformation associated with the emplacement of the Tulipan sill, mid-Norwegian margin: Interpretation, **5**, 1–15, doi: 10.1190/INT-2016-0155.1.

Schmitz, B., B. Peucker-Ehrenbrink, C. Heilmann-Clausen, G. Åberg, F. Asaro, and C.-T. A. Lee, 2004, Basaltic explosive volcanism, but no comet impact, at the Paleocene–Eocene boundary: High-resolution chemical and isotopic records from Egypt, Spain and Denmark: Earth and Planetary Science Letters, **225**, 1–17, doi: 10.1016/j.epsl.2004.06.017.

Schofield, N., S. Holford, J. Millett, D. Brown, R. Jolley, S. Passey, D. Muirhead, C. Grove, C. Magee, J. Murray, M. Hole, A.-L. Jackson, and C. Stevenson, 2015, Regional magma plumbing and emplacement mechanisms of the Faroe-Shetland Sill Complex: Implications for magma transport and petroleum systems within sedimentary basins: Basin Research, **29**, 41–63, doi: 10.1111/bre.12164.

Schofield, N, D. W. Jolley, S. Holford, S. G. Archer, D. Watson, A. J. Hartley, J. Howell, D. Muirhead, J. Underhill, and P. Green, 2017, Challenges of future exploration within the UK Rockhall Basin.

Schroot, B. M., and R. T. Schüttenhelm, 2003, Shallow gas and gas seepage: Expressions on seismic and otheracoustic data from the Netherlands North Sea: Journal of Geochemical Exploration, **78**, 305–309, doi: 10.1016/S0375-6742(03)00112-2.

Skogseid, J., T. Pedersen, O. Eldholm, and B. T. Larsen, 1992, Tectonism and magmatism during NE Atlantic continental break-up: The Vøring Margin: Geological Society, London, Special Publications, **68**, 305–320.

Sluijs, A., S. Schouten, M. Pagani, M. Woltering, H. Brinkhuis, J. S. S. Damsté, G. R. Dickens, M. Huber, G.-J. Reichart, and R. Stein, 2006, Subtropical Arctic Ocean temperatures during the Palaeocene/Eocene thermal maximum: Nature, **441**, 610–613, doi: 10.1038/nature04668.

Smallwood, J. R., and J. Maresh, 2002, The properties, morphology and distribution of igneous sills: Modelling, borehole data and 3D seismic from the Faroe-Shetland area, in D. W. Jolley, and B. R. Bell, eds., The North Atlantic Igneous Province: Stratigraphy, tectonic, volcanic and magmatic processes: Geological Society, London, Special Publications **197**, 271–306.

Storey, M., R. A. Duncan, and C. C. Swisher, 2007, Paleocene-Eocene thermal maximum and the opening of the northeast Atlantic: Science, **316**, 587–589, doi: 10.1126/science.1135274.

Svensen, H., and B. Jamtveit, 2010, Metamorphic fluids and global environmental changes: Elements, **6**, 179–182, doi: 10.2113/gselements.6.3.179w.

Svensen, H., B. Jamtveit, S. Planke, and L. Chevallier, 2006, Structure and evolution of hydrothermal vent complexes in the Karoo Basin, South Africa: Journal of the Geological Society, **163**, 671–682, doi: 10.1144/1144-764905-037.

Svensen, H., S. Planke, L. Chevallier, A. Malthe-Sørenssen, F. Corfu, and B. Jamtveit, 2007, Hydrothermal venting of greenhouse gases triggering Early Jurassic global warming: Earth and Planetary Science Letters, **256**, 554–566, doi: 10.1016/j.epsl.2007.02.013.

Svensen, H., F. Corfu, S. Polteau, Ø. Hammer, and S. Planke, 2012, Rapid magma emplacement in the Karoo Large Igneous Province: Earth and Planetary Science Letters, **325–326**, 1–9, doi: 10.1016/j.epsl.2012.01.015.

Svensen, H., S. Planke, A. Malthe-Sørenssen, B. Jamtveit, R. Myklebust, T. R. Eidem, and S. S. Rey, 2004, Release of methane from a volcanic basin as a mechanism for initial Eocene global warming: Nature, **429**, 542–545, doi: 10.1038/nature02566.

Svensen, H. H., S. Planke, B. Jamtveit, and T. Pedersen, 2003, Seep carbonate formation controlled by hydrothermal vent complexes: A case study from the Vøring Basin, the Norwegian Sea: Geo-Marine Letters, **23**, 351–358, doi: 10.1007/s00367-003-0141-2.

Wang, D., and M. Manga, 2015, Organic matter maturation in the contact aureole of an igneous sill as a tracer of hydrothermal convection: Journal of Geophysical Research: Solid Earth, **120**, 4102–4112, doi: 10.1002/2015JB011877.

Westerhold, T., U. Röhl, H. K. McCarren, and J. C. Zachos, 2009, Latest on the absolute age of the Paleocene–Eocene thermal maximum (PETM): New insights from exact stratigraphic position of key ash layers +19 and–17: Earth and Planetary Science Letters **287**, 412–419, doi: 10.1016/j.epsl.2009.08.027.

Whitaker, S., 1986, Flow in porous media I: A theoretical derivation of Darcy's law: Transport in porous media, **1**, 3–25, doi: 10.1007/BF01036523.

Zachos, J., M. Pagani, L. Sloan, E. Thomas, and K. Billups, 2001, Trends, rhythms, and aberrations in global climate 65 Ma to present: Science, **292**, 686–693, doi: 10.1126/science.1059412.

Zachos, J. C., R. G. Dickens, and R. E. Zeebe, 2008, An early Cenozoic perspective on greenhouse warming and carbon-cycle dynamics: Nature, **451**, 279–283, doi: 10.1038/nature06588.

Zhao, F., S. Wu, Q. Sun, M. Huuse, W. Li, and Z. Wang, 2014, Submarine volcanic mounds in the Pearl River Mouth Basin, northern South China Sea: Marine Geology, **355**, 162–172, doi: 10.1016/j.margeo.2014.05.018.

Biographies and photographs of authors are not available.

A.3 Publication III

III

Schmiedel, T., Galland, O., Breitkreuz, C., (2017). Dynamics of sill and laccolith emplacement in the brittle crust: role of host rock strength and deformation mode. Journal of Geophysical Research: Solid Earth 122, 8860–8871. doi: 10.1002/2017JB014468

Dynamics of Sill and Laccolith Emplacement in the Brittle Crust: Role of Host Rock Strength and Deformation Mode

T. Schmiedel[1] ![ORCID], O. Galland[1] ![ORCID], and C. Breitkreuz[2]

[1]Physics of Geological Processes, Department of Geosciences, University of Oslo, Oslo, Norway, [2]Geological Institute, Technical University Bergakademie Freiberg, Freiberg, Germany

Abstract Igneous intrusions in sedimentary basins exhibit a great diversity of shapes from thin sheets (e.g., dikes, sills and cone sheets) to massive intrusions (e.g., laccoliths and plugs). Presently, none of the established models of magma emplacement have the capability to simulate this diversity because they account for either purely elastic or purely plastic or purely viscous host rocks, whereas natural rocks are complex visco-elasto-plastic materials. In this study, we investigate the effects of elasto-plastic properties of host rock on magma emplacement using laboratory experiments made of dry granular materials of variable cohesion. Our results show how the deformation mechanism of the host rock controls the emplacement of magma: thin sheet sills form in high-cohesion materials, which dominantly deform by elastic bending, whereas massive intrusions such as punched laccoliths form in low-cohesion materials, which dominantly deform by shear failure. Our models also suggest that combined elastic/shear failure deformation modes likely control the emplacement of cone sheets. Our experiments are the first to spontaneously produce diverse, geologically relevant intrusion shapes. Our models show that accounting for the elasto-plastic behavior of the host rock is essential to filling the gap between the established elastic and plastic models of magma emplacement, and so to reveal the dynamics of magma emplacement in the Earth's brittle crust.

1. Introduction

Igneous intrusions in the upper brittle crust exhibit diverse shapes ranging from thin sheets, such as dikes, sills, saucer-shaped sills, and cone sheets, to thick, massive intrusions such as laccoliths, bysmaliths, plutons, and plugs (Figure 1) (e.g., Breitkreuz & Petford, 2004; Bunger & Cruden, 2011; Delpino et al., 2014; Galland et al., 2017; Gilbert, 1877; Habert & de Saint-Blanquat, 2004; Phillips, 1974). Each intrusion shape reflects a distinct mode of magma emplacement (Galland et al., 2017). Such diversity illustrates the complex physical behavior of magma-host rock systems during magma emplacement, mostly as a result of the wide range of magma viscosities (100–10^{18}) (Dingwell et al., 1993; Scaillet et al., 1997) and the wide range of elasto-plastic rheologies of the host rock (Galland et al., 2017; Ranalli, 1995).

To date, two end-member types of magma emplacement models exist. On one hand, models for sheet intrusions consider "relatively low," often neglected, viscosity magma into purely elastic rock (Bunger & Cruden, 2011; Galland & Scheibert, 2013; Kavanagh et al., 2015; Malthe-Sørenssen et al., 2004; Michaut, 2011; Pollard & Johnson, 1973; Thorey & Michaut, 2016). On the other hand, models for massive intrusions consider very viscous magma intruding into a weak, usually plastic host rock (e.g., Brothelande et al., 2016; Merle & Borgia, 1996; Montanari et al., 2010; Roman-Berdiel et al., 1995). Field observations (de Saint-Blanquat et al., 2006; Spacapan et al., 2017; Wilson et al., 2016) and seismic data (Jackson et al., 2013; Schmiedel et al., 2017, and references therein), however, indicate that both elastic and plastic deformation contemporaneously accommodate magma emplacement. In addition, plastic (Haug et al., 2017) and elasto-plastic (Scheibert et al., 2017) models suggest that inelastic deformation of the host rock might significantly affect the dynamics of magma propagation, even if inelastic deformation is restricted to an area of negligible size compared to that of the intrusion. Therefore, the end-member emplacement models are oversimplified with respect to natural rock behavior. As a consequence, none of them are able to reproduce the diversity of intrusion shapes and the modes of host rock deformation that accommodate their emplacement.

We present laboratory experiments of magma emplacement in realistic elasto-plastic brittle crust, which is modeled using dry granular materials of variable cohesion. Depending on the cohesion of the model rock, the modeled intrusion shapes and host rock deformation modes ranged from thin, sill-like sheets to
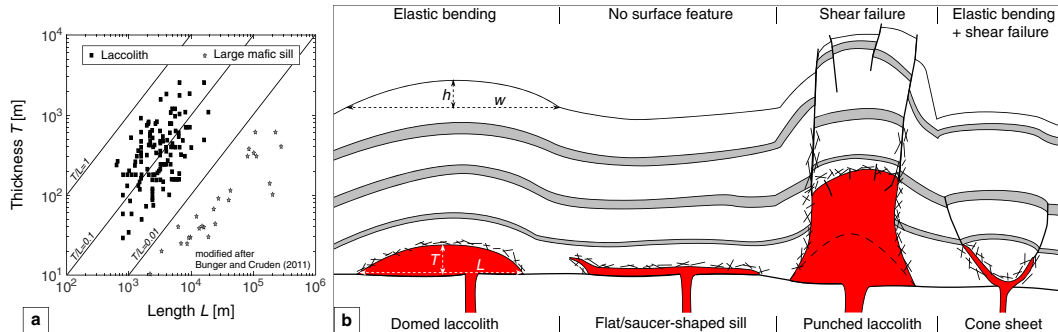
Figure 1. (a) Plot of thickness as a function of length of laccoliths and large mafic sills in nature, modified after Bunger and Cruden (2011). Lines display constant aspect ratios T/L. (b) Schematic sketch of the characteristic intrusion shapes and the associated overburden deformation in the Neuquén Basin/Argentina modified after Delpino et al. (2014) and Rodriguez Monreal et al. (2009). Intrusion thickness T, intrusion diameter L, dome amplitude h, and dome width w.

massive, punched laccoliths, and from gentle bending to prominent shear failure, respectively. Our experiments, the first that spontaneously simulate both sheet and massive intrusions, bridge the existing end-member magma emplacement models and highlight the importance of the host rock strength and associated deformation mode.

2. Experimental Methods

We used dry Coulomb granular materials of variable strengths as model rock (Table 1) (Abdelmalak et al., 2016; Galland et al., 2006): (1) a high-cohesion (~600 Pa) end-member consisting of fine-grained crystalline silica flour (SF), simulating competent rocks such as limestone; (2) a low-cohesion (~100 Pa) end-member consisting of glass microspheres (GMs), simulating weak rocks such as shale; and (3) materials with intermediate cohesion consisting of homogeneous SF-GM mixtures with different proportions (Table 1). The cohesion of the SF-GM mixtures is linearly correlated with their mixing proportions (Abdelmalak et al., 2016). The model magma consists of molten vegetable oil of viscosity $\eta = 2 \times 10^{-2}$ Pa s at 50°C (Galland et al., 2006). The relevance of these materials and the scaling of the models are described in detailed by Galland et al. (2014), Galland et al. (2006), and Abdelmalak et al. (2016) and in section 4.2.

The preparation procedure was the same as that of the layered models of Galland et al. (2009). The experiments were contained in a 40×40 cm box (Figure 2). They consisted of two layers of the same compacted granular material with a density difference of <5% (Galland et al., 2009). For the compaction procedure we first measured a mass of granular material for the lower layer (final thickness of the layer is equal to the inlet height), which we compacted using a high-frequency compressed-air shaker (Houston Vibrator, model GT-25). Subsequently, we placed a flexible net onto the surface of this first layer, and poured a second mass of granular material. The whole system was compacted until reaching the desired thickness of the overburden above the inlet (0.03 m). This procedure allows for a homogeneous, repeatable, and fast compaction of the granular materials, and ensures a good control of their density (<5% uncertainty), and so of their cohesion.

Table 1
Overview of the Experimental Series and Materials

Experiment no.	Model rock materials (GM/SF[a] wt %)	Compacted density (kg/m³)	Cohesion (Pa)[b]	Experiment duration t_e (s)	Intrusion shape
Experiment 1	0/100	1100	559.91	101	Saucer-shaped sill
Experiment 2	50/50	1450	374.96	29	Saucer-shaped sill
Experiment 3	80/20	1605	313.1	7	Cone sheet
Experiment 4	90/10	1620	239.5	21	Laccolith
Experiment 5	100/0	1435	142.3	18	Laccolith

Note. Galland et al. (2006) determined the angle of friction for GM and SF with 26° and 39°, respectively.
[a]GMs = glass microspheres/SF = silica flour.　[b]After Abdelmalak et al. (2016).
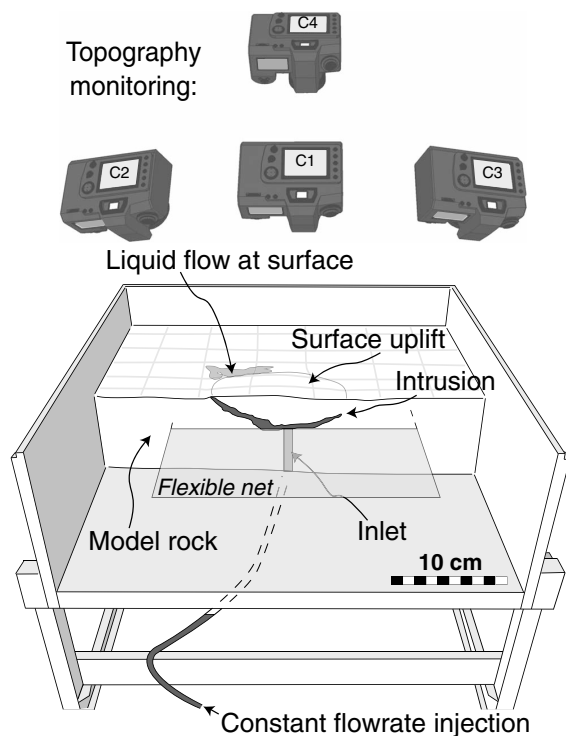
Figure 2. Drawing of the experimental setup (modified after Galland et al., 2016).

The flexible net simulated a weak interface between sedimentary layers, but quantifying its mechanical effects is challenging. We assume that the net approximately simulates strength contrasts in layered rocks, which can be as high as several orders of magnitude (Hoek et al., 1998; Schellart, 2000). The horizontal extent of the net in the experiments was significantly larger than the final intrusion diameters; therefore, the edges of the net had no effects on oil emplacement.

A volumetric pump injected the vegetable oil at constant flow rate (40 mL min^{-1}), which corresponds to an average inlet velocity of v_i = 0.026 m s^{-1} through a d = 5 mm diameter inlet. We designed the experiments such that the net is located just at the inlet. This way the oil flows directly along the net; therefore, the experiments do not simulate the feeder-sill transition, and the inlet in the experiments is not to be compared to sill feeders in nature. The oil initially followed the flexible net as a stratigraphic weakness (resembling an initial sill stage) before propagating upward. The intrusion of the oil triggered deformation of the experimental surface, which was monitored using a photogrammetry setup consisting of four synchronized DSLR cameras (Figure 2) (Galland et al., 2016). This system produced high-resolution (<0.1 mm) and high-precision (~0.05 mm) topographic maps and horizontal displacement maps. The monitoring frequency was 1 Hz. The end of the experiment (t_e) coincided with the eruption of oil at the surface (Table 1). After the end of the experiment, the oil solidified, the resulting intrusion was excavated, and its shape was computed using the same photogrammetry system (Galland et al., 2016). Thus, this photogrammetry system allows direct comparison between the intrusion shape and the associated surface deformation. During cooling, the oil percolates into the granular host material. Visual observations show that this percolation takes many minutes; i.e., it takes a longer time than the duration of the experiments. We infer that the oil percolation is negligible and has no effect during the emplacement of the oil. Note that our models do not take into account the thermal effects of magma emplacement on the host rock rheology. These effects have been documented by Karlstrom et al. (2017) for the incremental growth of large, deep plutonic complexes. However, given that our models intend to simulate the emplacement of relatively small intrusions in the shallowest, cold parts of the brittle crust, we consider these mechanisms to be negligible.

In this paper, we present a series of experiments in which the cohesion of the model rock was variable from high-cohesion (100% SF) to low-cohesion (100% GM), with intermediate-cohesion mixtures (Table 1). Both the injection depth (3 cm) and the injection flow rate (40 mL min^{-1}) were kept constant. The dimensional analysis of the models and their similarity to their geological prototypes are discussed in section 4.2.

3. Model Results

In experiment 1 (high cohesion, 100% SF; Table 1), the resulting intrusion was a typical saucer-shaped sill, with a circular inner sill of diameter ~10 cm (Figure 3) emplaced along the net, connected outward to gently dipping (15°–35°) inclined sheets that flattened out to outer sills (Figure 3) (Polteau et al., 2008). The associated surface deformation in Figure 3a exhibited a wide, low-amplitude (amplitude-to-width ratio h/w < 0.03; Figure 4) bell-shaped dome, which exhibited gradual slope variations (maximum slopes <3°), except locally prior to oil eruption at the outer margin of the dome (Figure 3a). At the end of experiment 1, the horizontal extent of the dome correlated with that of the underlying intrusion (Figure 3).

In experiments 2 and 3, the cohesion of the model rock was lower than in experiment 1 (Table 1). The resulting bodies were also saucer-shaped sheet intrusions. However, with decreasing cohesion the diameter of the inner horizontal sill decreased (5–4 cm; Figure 3b), and the dip angle of the inclined sheets increased (Figure 3b). In experiment 3, the inner sill was so small that the intrusion can be defined as a cone sheet
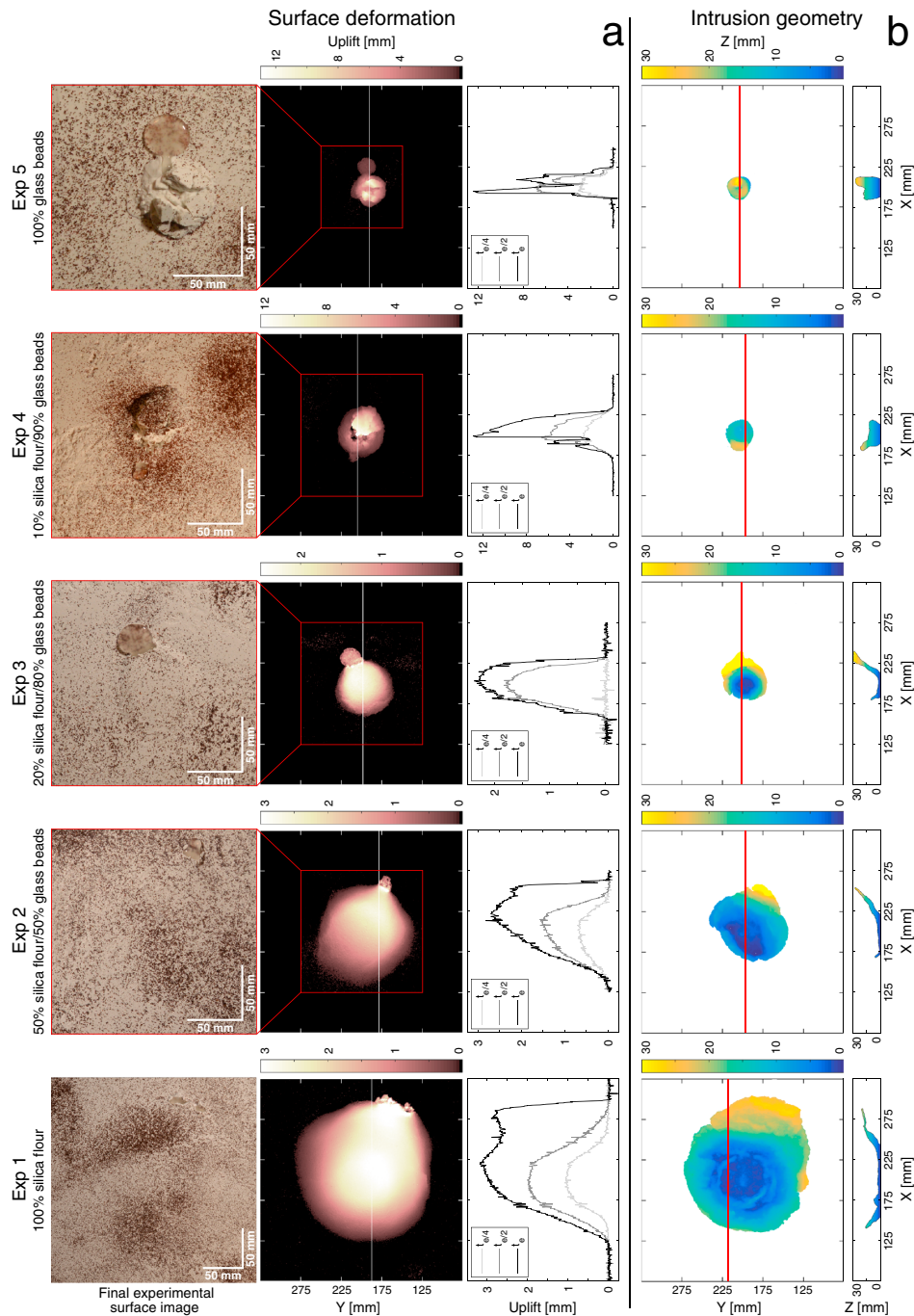
Figure 3. (a) Experimental results of the overburden deformation. (top row) Ortho-rectified images of the final model surface. (middle row) Topographic maps of the final model surface. (bottom row) Topographic profiles of the surface uplift for three time steps. The experiment duration is given by t_e. White lines in topographic maps locate the profiles of the profiles and plots (note the different vertical scales in topographic maps and profiles). (b) Experimental results on the intrusion geometry. Topographic maps of the top surface of excavated intrusion in our experiments, from high-cohesion host (crystalline silica flour; experiment 1) to low-cohesion host (glass microspheres; experiment 5). (top row) Red lines locate the profiles displayed in bottom row. (bottom row) Plots of profiles across intrusions displayed in top row maps.

Intrusion type vs. host rock strength

Figure 4. Plot of the maximum uplift to diameter ratio *h/w* versus host rock strength (cohesion) in our models. Open symbols correspond to sheet intrusions (saucer-shaped sills and cone sh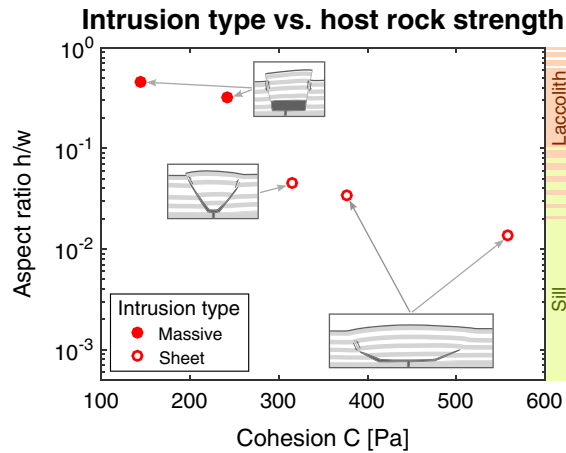eets), and full symbols correspond to massive intrusions (laccoliths). Colored bar to the right side of the plot indicates the natural ranges of *h/w* for sills (light green) and laccoliths (orange) estimated from field observations and seismic interpretations (Bunger & Cruden, 2011; Hansen & Cartwright, 2006; Schmiedel et al., 2017, and references therein).

(Figure 3b) (Burchardt et al., 2013; Galland et al., 2014). The associated surface deformations were low-amplitude domes (*h/w* < 0.05; Figures 3a and 4) as well, but their width decreased with decreasing cohesion of the model rock (Figure 3a). The domes were less smooth than that of experiment 1: the top parts were relatively flat, whereas their edges were steeper (4.5° to 5.5°; Figure 3a).

Experiments 4 and 5 (i.e., low cohesion) showed drastically different results. The intrusions were massive, not sheet intrusions. They exhibited roughly vertical plug-like shapes, with flat ~3 cm wide bottom and subvertical sidewalls (Figure 3b); i.e., the intrusions resembled punched laccoliths as shown in Figure 1 (Corry, 1988). The surface deformation displayed high-amplitude domes (*h/w* < 0.45) with sharp, steep (>45°) margins (Figure 3a). The tops of the domes were blocky (Figure 3a) and some blocks collapsed during the dome growth. After the start of eruption, we stopped the pump, and the dome kept collapsing as the oil was draining out from the underlying intrusion.

4. Interpretations and Discussion

4.1. Interpretation

Our results highlight a trend between the intrusion shapes and the cohesion of the overburden (Figure 3). The intrusions emplaced into the high- to intermediate-cohesion model rock (experiments 1–3) are sheet intrusions, whereas the intrusions in the low-cohesion model rock (experiments 4 and 5) are massive laccolith intrusions (Figure 3b). Even among the sheet intrusions our results show a gradual trend from wide, gently dipping saucer-shaped sills in experiment 1 (high cohesion) to narrow, steeply dipping cone sheet in experiment 3 (Figure 3b). In addition, in all experiments the injection occurs at the same depth (*H* = 3 cm); however, the diameter *L* of the intrusions and so the aspect ratio *H/L* strongly vary as a function of the cohesion of the overburden: intrusions are narrow (*H/L* ≈ 1) for laccoliths emplaced in low-cohesion host rock, whereas intrusions are wide (*H/L* < 1) for sills emplaced in high-cohesion host rock. These results clearly show that host rock strength is a key factor controlling magma emplacement.

An trend emanates between uplifted surface morphology (dome) and the cohesion of the overburden (Figures 3a and 4). In the high-cohesion experiment (experiment 1), the dome exhibits gentle slopes (1.8° to 2.7°) and curvatures and small *h/w* aspect ratios (Figure 4). We infer that the overburden dominantly deformed by elastic bending, as considered in theoretical (Bunger & Cruden, 2011; Galland & Scheibert, 2013; Michaut, 2011; Pollard & Johnson, 1973; Scheibert et al., 2017) and laboratory (Kavanagh et al., 2015; Pollard & Johnson, 1973) elastic models. An exception is the region near the point of eruption, where the dome edge was steeper (Figure 3a) and failure of the experimental surface occurred, similarly to the plastic models of Haug et al. (2017). In contrast, low-cohesion model rock experiments (experiments 4 and 5) feature domes with steep slopes and abrupt surface scarps marked by locally high curvatures (Figure 3a) and drastically higher (1 order of magnitude) *h/w* aspect ratios (Figure 4). We infer that the overburden dominantly deformed by shear failure. Finally, in experiments 2 and 3 (intermediate cohesion), the slopes at the surface ranged between those in experiment 1 and experiment 4 (Figure 3a). We infer that the overburden deformed by a combination of elastic bending and local shear failure. In conclusion, the cohesion greatly controls the deformation mode of intrusion host rock.

The points discussed above highlight a relation between the shapes of the intrusions and the deformation mode of their overburden. The massive laccoliths of experiments 4 and 5 are associated with dominant shear (mode II) failure in the low-cohesion overburden, in good agreement with the "punched laccolith" emplacement model (Corry, 1988; Gilbert, 1877) and the end-member plastic models of Roman-Berdiel et al. (1995). In contrast, the flat-lying, saucer-shaped sills of experiments 1 and 2 are associated with dominant elastic bending of the overburden, in good agreement with the end-member elastic models of Galland and Scheibert (2013), Malthe-Sørenssen et al. (2004), and Pollard and Johnson (1973). This suggests that the

Table 2
Values and Equations for the Dimensional Analysis

Values	Experiments	Nature
	General	
g (m s^{-2})	9.81	9.81
	Magma	
T (m)	0.0034–0.018	10–3,000
L (m)	0.04–0.24	500–10^5
ρ_m (kg m^{-3})	890	2,500–2,700
η (Pa s)	0.02	100–10^7
v (m s)	0.0072–0.038	0.00034–0.1
	Host	
H (m)	0.03	1,000–5,000
h ($\approx T$) (m)	0.0034–0.018	10–3,000
w ($\approx L$) (m)	0.04–0.24	500–10^5
ρ_r (kg m^{-3})	1,100–1,600	2,500
C (Pa)	100–600	10^6–10^8
ϕ (°)	26–39	25–45
	Dimensionless parameters	
$\Pi_1 = \frac{\rho_r g H}{C}$	0.54–4.71	0.25–122.63
$\Pi_2 = \phi$	26–39	25–45
$\Pi_3 = Re = \frac{\rho_m v T}{\eta}$	1.09–30.63	0.83×10^{-9}–81,000
$\Pi_4 = \frac{T}{L} \approx \frac{h}{w}$	0.014–0.45	0.0001–6
$\Pi_5 = \frac{H}{L} \approx \frac{H}{w}$	0.125–0.75	0.01–10
$\Pi_6 = \frac{\eta v}{C T}$	1.34×10^{-5}–0.0022	1.1×10^{-15}–1
$\Pi_7 = 1 - \frac{\rho_m}{\rho_r}$	0.19–0.44	−0.08–0

emplacement of the magma dominantly occurs by mode I (tensile opening) failure of the host rock. We cannot rule out, however, that local shear failure occurred, e.g., at the inner sill-to-inclined sheet transition (Galland et al., 2009; Haug et al., 2017; Scheibert et al., 2017). In between these plastic and elastic end-members, our experiments suggest that the cone sheet of experiment 3 is associated with a combination of elastic bending and mode II failure of the overburden, which corroborates the conclusions of Phillips (1974) and Galland et al. (2014). In addition, our conclusion is very similar to those of Abdelmalak et al. (2012), who showed that the formation of *V*-shaped sheet intrusions in 2-D experiments can be controlled by local shear failure of the host rock. All these results highlight the first-order control of host rock damage on magma propagation, which is in good agreement with progressive damage models of volcano deformation in response to inflating magma body (Carrier et al., 2015; Go et al., 2017). Overall, we conclude that the deformation mode of the host rock is a primary parameter governing magma emplacement in the Earth's brittle crust.

4.2. Dimensional Analysis and Scaling

In this section, we discuss the geological relevance of our laboratory results through the dimensional analysis of the modeled system and its similarity to their corresponding geological objects (Galland et al., 2017; Gibbings, 2011; Merle, 2015). The dimensional analysis is challenging because we need to account for (1) the elastic/inelastic deformation mode of the host rock, (2) the flow regime of the viscous flow, and (3) the coupling between the flowing viscous fluid and the deforming host. Because of the complexity of the physical system, there is no mathematical model from which scaling parameters can be extracted (see e.g., Bunger & Cruden, 2011; Michaut, 2011); therefore, we apply the dimensional analysis procedure as described by Gibbings (2011). In addition, the discussion of the similarity of our models to its geological equivalent is not straightforward because of (1) the broad range of magma viscosities and (2) contrasting deformation mechanisms in the host (Galland et al., 2017). The procedure described below follows the main lines of those implemented by Merle and Borgia (1996), Galland (2012), and Galland et al. (2014, 2009).

Our experiments are designed to model processes at basin scale; i.e., 1 cm represents ~1 km in nature. The physical parameters ruling magma flow in our experiments are (Table 2) (1) magma velocity in the intrusions *v*, (2) magma viscosity η, (3) magma density ρ_m, and (4) the resulting diameter *L* and thickness *T* of the intrusion (Figure 1). Note here that the diameter *L* and the thickness *T* of the intrusion are not prescribed a priori, but they are experimental results. Note as well, as mentioned above, that we do not consider the feeder-sill transition; therefore, we do not account for the inlet geometry/size in the dimensional analysis. The physical parameters governing the brittle host rock and its deformation in our experiments are (Table 2) (1) thickness of the overburden *H*; (2) rock density ρ_r; (3) cohesion *C*, i.e., host rock shear strength; and (4) angle of friction ϕ. Here the overburden thickness *H* corresponds to the injection depth in our experiments. We measure the host rock deformation through the uplift *h* and the diameter *w* of the dome (Figure 1), which are assumed in our analysis to represent realistic approximate values of the intrusion thickness *T* and intrusion diameter *L*, respectively. Our results indeed confirm that millimeter-scale uplifts in experiment 1 to experiment 3 reflect millimeter-scale sheet intrusion thickness, whereas >1 cm uplifts in experiment 4 and experiment 5 reflect >1 cm massive intrusion thickness (Figure 3). Similarly, 20 cm dome diameter reflects the 18–20 cm intrusion radius, whereas the 4 cm dome diameter reflects the 3–4 cm intrusion diameter (Figure 3). Therefore, we consider $h \approx T$ and $w \approx L$, so that two parameters are considered in our dimensional analysis instead of four. The whole system is subject to gravity *g*. Thus, according the Buckingham Π theorem (e.g., Gibbings, 2011), 10 variables minus three variables with independent dimensions lead to seven independent dimensionless numbers (Table 2). These seven dimensionless numbers characterize the physics of the modeled processes; our models are similar to its geological

equivalent if the values of these dimensionless ratios in both experiments and nature are similar. In the following paragraphs, we discuss successively the dimensionless parameters that account for (1) the host rock behavior, (2) the magma flow, and (3) the physical coupling between the host and the magma.

The first dimensionless parameter to scale the brittle host rock is the ratio of gravitational stress to cohesion $\Pi_1 = \rho_r\, g\, H/C$ (Table 2). In our experiments, injection is at 3 cm depth, and the model rock cohesion varies from ~100 to ~600 Pa (Abdelmalak et al., 2016). The values of Π_1 thus range between 0.54 and 4.71. In nature, rocks have an average density of about 2500 kg m^{-3}; their cohesion spans between 10^6 and 10^8 Pa (Schellart, 2000, and references therein). In sedimentary basins, intrusion depths are typically between 1 and 5 km. The values of Π_1 in nature thus range between 0.25 and 122.63 (Table 2). The model values of Π_1 are within the range of values of Π_1 in nature; therefore, the brittle deformation regime in our experiments is representative of those of the corresponding geological systems. Note that the values of Π_1 in our models correspond to the lower range of Π_1 in nature (Table 2); thus, our models do not account for gravity-dominated systems in nature ($\Pi_1 >> 1$).

The second dimensionless parameter to scale the brittle host rock is the angle of internal friction $\Pi_2 = \phi$ (Table 2). The angle of internal friction of the granular materials ranges between 26° and 39° (Abdelmalak et al., 2016; Galland et al., 2006). This is within the range of those measured for natural rocks (Table 2) (Schellart, 2000, and references therein).

The first dimensionless ratio to scale the magma flow regime is the Reynolds number $Re = \Pi_3 = \rho_m\, v\, T/\eta$, i.e., the ratio between inertial and viscous forces within the fluid. We use Π_3 to describe the flow behavior within the intrusion. Therefore, we need to estimate the magma velocity v within the intrusion using a simple conversion formula $v = v_i\, d/T$, where d is the thickness of the inlet/feeder. In our experiments, $v_i = 0.026$ m s^{-1}, $d = 0.005$ m, and T is variable from 0.0034 to 0.018 m; therefore, the values of Re in our experiments are in the range of 1.09–30.63 (Table 2). This shows that the magma flow in the model intrusions is laminar. In nature, the magma density ranges from 2500 to 2700 kg m^{-3} for felsic to mafic magma, respectively (Galland et al., 2017, and references therein). Magma velocity v_i in feeder dikes vary between 0.01 and 1 m s^{-1} (Battaglia & Bachèlery, 2003; Clemens & Mawer, 1992; Petford et al., 1993; Roman et al., 2004; Spence & Turcotte, 1985), thickness of feeder dikes d typically vary between 1 and 10 m, and the intrusion thickness T typically vary between 10 and 3000 m. Therefore, in nature the values calculated for Re range between 0.83×10^{-9} and 81,000 (Table 2). Note that the highest values of Re would correspond to 3000 m thick mafic intrusions with magma velocity of 1 m s^{-1}, which is unlikely. Therefore, a geologically relevant upper bound for Re may be significantly lower, which indicate that in most common cases, the magma flow within intrusions is laminar. Therefore, the laminar fluid flow in our model intrusions is representative of most magma flow regimes within intrusions in nature.

The second dimensionless ratio to scale the magma intrusion is the resulting geometric aspect ratio $\Pi_4 = T/L \approx h/w$ of the intrusions. In our experiments, the values of Π_4 range between ~0.014 for sills and ~0.45 for laccoliths (Table 2 and Figure 4), which overlap with the values of Π_4 in nature ranging between 0.0001 and 6 (Table 2). Our model intrusions are thus overall geometrically similar to those in nature (Figure 4).

We consider now the dimensionless ratios that account for the physical coupling between the intrusions and the overburden. The first dimensionless parameter to account for this is the geometric ratio $\Pi_5 = H/L \approx H/w$, which describes whether the intrusion is larger than its depth ($\Pi_5 < 1$, i.e., considered as a large shallow intrusion) or narrower than its depth ($\Pi_5 > 1$, i.e., considered as a narrow deep intrusion). Theoretical models of sill emplacement based on thin plate theory require that $\Pi_5 < 0.1$ (e.g., Galland & Scheibert, 2013; Michaut, 2011). In our experiments, the values of Π_5 range between ~0.125 for laccoliths and ~0.75 for sills (Table 2). The respective values of Π_5 for our model sills and laccoliths are in the range of their equivalent values in nature (0.01–10), which implies that our model intrusions are similar to their geological equivalent (Table 2). Note that most values of Π_5 are larger than 0.1, which implies that the established theoretical models are generally not applicable to thick sills and laccoliths.

The second dimensionless parameter $\Pi_6 = \eta\, v/C\, T$, which quantifies the balance between the viscous stresses within the flowing magma and the cohesion (strength) of the host rock. Note that this Π_6 ratio is the same as the Π_2 ratio defined by Galland et al. (2014). In our experiments, the values of Π_6 span between 1.34×10^{-5} and 0.0022 (see Table 2). In nature, the broad range of magma viscosities in sheet intrusions and massive

intrusions due to, e.g., magma composition (mafic-felsic), leads to a wide theoretical range of values of Π_6 in nature between 1.1×10^{-15} and 1 (Table 2) (Galland et al., 2014). Thus, the values of Π_6 in our models are in the same range as those of Π_6 in geological systems, showing that our models are similar to their geological equivalent in terms of balance between viscous stresses and host rock strength. Note that our experiments do not consider cooling effects: magma cooling induces viscosity increase which may locally affect the value of Π_6 in nature (Thorey & Michaut, 2016).

The final dimensionless parameter $\Pi_7 = 1 - \rho_m/\rho_r$ is the ratio of hydrostatic to lithostatic forces, i.e., buoyancy of the magma (Table 2). In our experiments Π_7 ranges from 0.19 to 0.44 (Table 2). If ($\Pi_7 < 0$), the magma is heavier than the host rock, and locally negatively buoyant; in contrast, if $\Pi_7 > 0$, the magma is lighter than the host rock, so that the magma is locally buoyant. In nature Π_7 is neutrally buoyant to negatively buoyant, whereas the oil in our experiments is positively buoyant (Table 2). Therefore, there is a discrepancy between the experiments and the geological systems. However, as sills and laccoliths are (sub)horizontal conduits, the effect of the buoyancy is very small, even negligible in the modeled systems as discussed in previous works (e.g., Galland et al., 2009).

To summarize, the systematic overlap of the values of the Π numbers in both model and nature show that the processes modeled in our experiments are similar to magma emplacement processes in nature.

4.3. Discussion

As mentioned above, both oil percolation and intrusion drain-out occurred after the end of the experiments. Thus, the shapes of the excavated intrusions do not reflect their exact shapes during their emplacement. Consequently, we cannot use the final excavated intrusions to estimate their in situ aspect ratios (T/L) during their emplacement. Alternatively, we assume that the aspect ratios of the domes (h/w) measured at the surface of the experiments during the experiments are better estimates of the aspect ratios of the underlying intrusions. In the following paragraphs, we will discuss the aspect ratios T/L of the intrusions in our experiments using the values of the aspect ratios h/w of their associated domes.

Our laboratory models simulate for the first time the emplacement of both thin sheet (saucer-shaped sills and cone sheets) and massive (punched laccolith) intrusions, as illustrated in Figure 1. Our experiments reproduce spontaneously a large range of aspect ratios of natural sills and laccoliths, covering several orders of magnitude without prescribing the intrusion geometry (thin sheet versus massive; Figure 4). These results imply that our models capture the first-order mechanisms of magma emplacement in a realistically complex host rock. This was only possible by accounting for variable complex elasto-plastic mechanical properties of the host rock.

The geometrical aspect ratios $\Pi_4 = T/L$ for laccoliths in our experiments concur with values from field observations and seismic interpretation, i.e., 0.02–1 for laccoliths and thick sills (Figure 4) (Bunger & Cruden, 2011; Cruden et al., 2017; de Saint-Blanquat et al., 2006; Delpino et al., 2014; Magee et al., 2017, and references therein; McCaffrey & Petford, 1997; Schmiedel et al., 2015). Thus, we conclude that our models are able to simulate the diversity of observed intrusion geometries in nature. The values of Π_4 for our model sills (0.014 to 0.02) are in the range, close to the upper bound, of those for sills in nature (0.0001 to 0.05) (Bunger & Cruden, 2011; Cruden et al., 2017; Hansen & Cartwright, 2006; Schmiedel et al., 2017). This suggests that our models simulate the emplacement of magmas that are more viscous than mafic magmas, e.g., andesite to rhyolite sills (Breitkreuz et al., 2017, and references therein). Other possibilities are that neither the elastic properties of the silica flour, i.e., it is too soft with respect to natural rocks, nor do the properties of intrusion-induced dilation or compaction of the host material properly simulate those of natural rocks. However, constraining the elastic properties, and so the elastic scaling, of the silica flour is challenging.

The main difference between our models and the established elastic models of sills and laccoliths is the ability of the overburden to fail along shear fractures (Kavanagh et al., 2006; Pollard & Johnson, 1973). Several studies discuss that overburden failure is likely of primary importance for understanding magma emplacement mechanisms (e.g., Abdelmalak et al., 2012; Cruden et al., 2017; Guldstrand et al., 2017; Haug et al., 2017), and our models confirm that the elasto-plastic deformation modes of the overburden play an important role on magma emplacement. Similar to our results, the numerical models of Bunger and Cruden (2011) also reproduced the natural range of laccoliths aspect T/L ratios, up to 0.6 (Figures 1 and 4).

However, the mathematical formulation of their model is that of a thin stiff plate; the assumptions of which are (Ventsel & Krauthammer, 2001) (1) the thin plate formulation implies shallow intrusions, i.e., intrusion diameter should be larger than 10 times its depth ($L/H \geq 10$) (criterion used by, e.g., Galland & Scheibert, 2013 & Scheibert et al., 2017), and (2) the stiff plate formulation implies small deflection of the overburden, i.e., the overburden thickness should be 5 times greater than the intrusion thickness ($H/T \geq 5$). Combining the thin plate and stiff plate criteria implies that the intrusion diameter should be 50 times greater than intrusion thickness ($L/T > 50$ or $T/L < 0.02$). This critical value of T/L is 1 to 2 orders of magnitude smaller than those of laccoliths in nature, and so those calculated from the thin, stiff plate models of Bunger and Cruden (2011). Hence, most of the laccolith calculations (>90%) presented by Bunger and Cruden (2011) are outside the mathematical assumptions of their mathematical model, and the resulting large deflections are expected to produce nonrealistically large stresses due to local extreme bending of the overburden. The strong mismatch between the critical value $T/L < 0.02$ for the validity of thin stiff plate models and the values of $T/L > 0.01$ of natural laccoliths explains the mismatch between the elastic assumption of the models and the inelastic deformation observed in the field (e.g., Agirrezabala, 2015; de Saint-Blanquat et al., 2006; Spacapan et al., 2017; Wilson et al., 2016). This analysis confirms that the inelastic deformation observed in the field likely plays a significant role during magma emplacement; hence, inelastic deformation should be accounted in magma emplacement models.

Further, our experiments simulate conical intrusion shapes, which resemble cone sheet intrusions described in nature (e.g., Burchardt et al., 2013; Galland et al., 2014; Gudmundsson et al., 2014). Our results show their formation as transition stage between sills and laccolith under intermediate host rock strength conditions (Figure 3). These cone sheet intrusions have never been accounted for in sill or laccolith models. However, seismic data and the field observations show that such features are in fact present in volcanic basins (Burchardt et al., 2013; Gudmundsson et al., 2014; Sun et al., 2014). That means our models address the mechanism of magma emplacement in a more realistic way, simulating both (1) the established end-member shapes of intrusions (sheet and massive) and additionally, (2) the poorly understood occurrence of cone sheet intrusions.

In our experiments the oil viscosity was constant, although magma viscosity plays a major role on magma emplacement mechanism (e.g., Rubin, 1993). However, Galland et al. (2014) showed that the emplacement of magma in the brittle crust is neither governed by the flowing viscous magma nor the deforming host rock alone, but by the mechanical coupling between them as expressed by the dimensionless ratios Π_6 (Π_2 of Galland et al. (2014); Table 2). This dimensionless number quantifies the ratio between the viscous stresses in the magma and the cohesion of the brittle host rock. This ratio shows that decreasing the cohesion of the host rock, as we did in our experiments, is equivalent to increasing the viscosity of the magma. Our results are corroborated by many field observations, as punched laccoliths (1) are commonly observed in weak rocks and/or (2) are made of magma of dominantly high viscosity. We are aware that the elastic properties of our silica flour and glass beads are unconstrained, such that elastic stresses in our models might not be properly scaled. Thus, we did not quantify the relative elastic or plastic contributions to the deformation of the overburden. We are also aware that the dilation and compaction properties of our granular materials might not be identical to those of natural rocks. Our experiments investigate one aspect only of the magma-host rock systems, and future work should investigate systematically the combined effects of magma viscosity and host rock strength. This will ensure filling the gap between the formerly distinct sheet intrusion and massive intrusion models of magma emplacement.

5. Conclusions

This paper describes the results of laboratory experiments of magma emplacement in the brittle crust with horizontal layering. We performed a parameter study to test the effect of the cohesion (strength) of the model host rock, while the depth of magma injection and magma injection rates were kept constant. The main results of our studies are the following:

1. Our laboratory models simulate—for the first time—the emplacement of both sheet intrusions (thin saucer-shaped sills and cone sheets) and massive intrusions (punched laccoliths) in a controlled manner.
2. Saucer-shaped sills form in high-cohesion host material, punched laccolith intrusions form in low-cohesion host material, and cone sheets form in intermediate-cohesion material.

3. Our models show that the diameter of the intrusion decreases with the cohesion of the overburden: at same depth, thin saucer-shaped sills emplaced in high-cohesion host rock are broader than massive laccoliths emplaced in low-cohesion host rock.
4. The overburden deformation modes accommodating saucer-shaped sill and laccolith emplacement are dominated by elastic bending and shear failure, respectively; the emplacement of cone sheets may be accommodated by mixed elastic bending and shear failure of the overburden.

Our laboratory experiments show that cohesion, as a measurement for the host rock strength and associated deformation mode, is an important factor controlling magma emplacement. In addition, our results show the necessity to account for both elastic deformation and shear failure of the host to realistically address the emplacement of magma in the brittle upper crust.

References

Abdelmalak, M. M., Bulois, C., Mourgues, R., Galland, O., Legland, J. B., & Gruber, C. (2016). Description of new dry granular materials of variable cohesion and friction coefficient: Implications for laboratory modelling of the brittle crust. *Tectonophysics*, *684*, 39–51. https://doi.org/10.1016/j.tecto.2016.03.003

Abdelmalak, M. M., Mourgues, R., Galland, O., & Bureau, D. (2012). Fracture mode analysis and related surface deformation during dyke intrusion: Results from 2D experimental modelling. *Earth and Planetary Science Letters*, *359-360*, 93–105. https://doi.org/10.1016/j.epsl.2012.10.008

Agirrezabala, L. M. (2015). Syndepositional forced folding and related fluid plumbing above a magmatic laccolith: Insights from outcrop (Lower Cretaceous, Basque-Cantabrian Basin, western Pyrenees). *Geological Society of America Bulletin*, *127*(7–8), B31192.1–B3111000. https://doi.org/10.1130/b31192.1

Battaglia, J., & Bachèlery, P. (2003). Dynamic dyke propagation deduced from tilt variations preceding the March 9, 1998, eruption of the Piton de la Fournaise volcano. *Journal of Volcanology and Geothermal Research*, *120*(3-4), 289–310. https://doi.org/10.1016/S0377-0273(02)00410-9

Breitkreuz, C., Ehling, B.-C., & Pastrik, N. (2017). The subvolcanic units of the Late Paleozoic Halle volcanic complex, Germany: Geometry, internal textures and emplacement mode. In C. Breitkreuz & S. Rocchi (Eds.), *Physical geology of shallow magmatic systems—Dykes, sills and laccoliths* (pp. 1–13). Berlin: Springer. https://doi.org/10.1007/11157_2014_2

Breitkreuz, C., & Petford, N. (2004). Physical geology of high-level magmatic systems. *Geological Society of London Special Publications*, 262. https://doi.org/10.1144/GSL.SP.2004.234.01.17

Brothelande, E., Peltier, A., Got, J. L., Merle, O., Lardy, M., & Garaebiti, E. (2016). Constraints on the source of resurgent doming inferred from analogue and numerical modeling—Implications on the current feeding system of the Yenkahe dome–Yasur volcano complex (Vanuatu). *Journal of Volcanology and Geothermal Research*, *322*, 225–240. https://doi.org/10.1016/j.jvolgeores.2015.11.023

Bunger, A. P., & Cruden, A. R. (2011). Modeling the growth of laccoliths and large mafic sills: Role of magma body forces. *Journal of Geophysical Research: Solid Earth*, *116*, B02203. https://doi.org/10.1029/2010JB007648

Burchardt, S., Troll, V. R., Mathieu, L., Emeleus, H. C., & Donaldson, C. H. (2013). Ardnamurchan 3D cone-sheet architecture explained by a single elongate magma chamber. *Scientific Reports*, *3*(1), 1–7. https://doi.org/10.1038/srep02891

Carrier, A., Got, J.-L., Peltier, A., Ferrazzini, V., Staudacher, T., Kowalski, P., & Boissier, P. (2015). A damage model for volcanic edifices: Implications for edifice strength, magma pressure, and eruptive processes. *Journal of Geophysical Research: Solid Earth*, *120*, 567–583. https://doi.org/10.1002/2014JB011485

Clemens, J. D., & Mawer, C. K. (1992). Granitic magma transport by fracture propagation. *Tectonophysics*, *204*(3-4), 339–360. https://doi.org/10.1016/0040-1951(92)90316-X

Corry, C. E. (1988). *Laccoliths; Mechanics of emplacement and growth*, (p. 114). *Geological Society of America Special Papers*, Boulder, CO. https://doi.org/10.1130/SPE220-p1

Cruden, A. R., McCaffrey, K. J. W., & Bunger, A. P. (2017). Geometric scaling of tabular igneous intrusions: Implications for emplacement and growth. In C. Breitkreuz & S. Rocchi (Eds.), *Physical geology of shallow magmatic systems—Dykes, sills and laccoliths* (pp. 1–28). Berlin: Springer. https://doi.org/10.1007/11157_2017_1000

de Saint-Blanquat, M., Habert, G., Horsman, E., Morgan, S. S., Tikoff, B., Launeau, P., & Gleizes, G. (2006). Mechanisms and duration of non-tectonically assisted magma emplacement in the upper crust: The Black Mesa pluton, Henry Mountains, Utah. *Tectonophysics*, *428*(1-4), 1–31. https://doi.org/10.1016/j.tecto.2006.07.014

Delpino, D., Bermúdez, A., Vitulli, N., & Loscerbo, C. (2014). Sistema de Petróleo no convencional relacionado con lacolitos Eocenos de intraplaca. In *Área altiplanicie del Payún, cuenca Neuquina, paper presented at IX Congreso de Exploración y Desarrollo de Hidrocarburos* (pp. 223–242). Instituto Argentino del Petróleo y el Gas: Mendoza.

Dingwell, D. B., Bagdassarov, N., Bussod, G., & Webb, S. L. (1993). Magma rheology. In R. W. Luth (Ed.), *Experiments at high pressure and applications to the Earth's mantle—Short course handbook* (Chapter 5), (pp. 131–196). Edmonton, Alberta: Mineralogical Association of Canada.

Galland, O. (2012). Experimental modelling of ground deformation associated with shallow magma intrusions. *Earth and Planetary Science Letters*, *317-318*, 145–156. https://doi.org/10.1016/j.epsl.2011.10.017

Galland, O., Bertelsen, H. S., Guldstrand, F., Girod, L., Johannessen, R. F., Bjugger, F., … Mair, K. (2016). Application of open-source photogrammetric software MicMac for monitoring surface deformation in laboratory models. *Journal of Geophysical Research: Solid Earth*, *121*, 2852–2872. https://doi.org/10.1002/2015JB012564

Galland, O., Burchardt, S., Hallot, E., Mourgues, R., & Bulois, C. (2014). Dynamics of dikes versus cone sheets in volcanic systems. *Journal of Geophysical Research: Solid Earth*, *119*, 6178–6192. https://doi.org/10.1002/2014JB011059

Galland, O., Cobbold, P. R., Hallot, E., de Bremond d'Ars, J., & Delavaud, G. (2006). Use of vegetable oil and silica powder for scale modelling of magmatic intrusion in a deforming brittle crust. *Earth and Planetary Science Letters*, *243*(3-4), 786–804. https://doi.org/10.1016/j.epsl.2006.01.014

Galland, O., Holohan, E., van Wyk de Vries, B., & Burchardt, S. (2017). Laboratory modelling of volcano plumbing systems: A review. In C. Breitkreuz, & S. Rocchi (Eds.), *Physical geology of shallow magmatic systems—Dykes, sills and laccoliths* (pp. 1–68). Berlin: Springer. https://doi.org/10.1007/11157_2015_9

Galland, O., Planke, S., Neumann, E.-R., & Malthe-Sørenssen, A. (2009). Experimental modelling of shallow magma emplacement: Application to saucer-shaped intrusions. *Earth and Planetary Science Letters*, *277*(3-4), 373–383. https://doi.org/10.1016/j.epsl.2008.11.003

Galland, O., & Scheibert, J. (2013). Analytical model of surface uplift above axisymmetric flat-lying magma intrusions: Implications for sill emplacement and geodesy. *Journal of Volcanology and Geothermal Research*, *253*, 114–130. https://doi.org/10.1016/j.jvolgeores.2012.12.006

Gibbings, J. C. (2011). *Dimensional analysis* (p. 297). London: Springer Science & Business Media. https://doi.org/10.1007/978-1-84996-317-6

Gilbert, G. K. (1877). *Report on the geology of the Henry Mountains*. Region, Washington: U. S. Geographical Geological Survey of the Rocky Mountain. https://doi.org/10.5962/bhl.title.51652

Go, S. Y., Kim, G. B., Jeong, J. O., & Sohn, Y. K. (2017). Diatreme evolution during the phreatomagmatic eruption of the Songaksan tuff ring, Jeju Island, Korea. *Bulletin of Volcanology*, *79*(3), 23. https://doi.org/10.1007/s00445-017-1103-2

Gudmundsson, A., Pasquarè, F. A., & Tibaldi, A. (2014). Dykes, sills, laccoliths, and inclined sheets in Iceland (pp. 1–14), Berlin: Springer. https://doi.org/10.1007/11157_2014_1

Guldstrand, F., Burchardt, S., Hallot, E., & Galland, O. (2017). Dynamics of surface deformation induced by dikes and cone sheets in a cohesive Coulomb brittle crust. *Journal of Geophysical Research: Solid Earth*, *122*, 1–14.

Habert, G., & de Saint-Blanquat, M. (2004). Rate of construction of the Black Mesa bysmalith, Henry Mountains, Utah. *Geological Society, London, Special Publications*, *234*(1), 163–173. https://doi.org/10.1144/gsl.sp.2004.234.01.10

Hansen, D. M., & Cartwright, J. (2006). The three-dimensional geometry and growth of forced folds above saucer-shaped igneous sills. *Journal of Structural Geology*, *28*(8), 1520–1535. https://doi.org/10.1016/j.jsg.2006.04.004

Haug, Ø. T., Galland, O., Souloumiac, P., Souche, A., Guldstrand, F., & Schmiedel, T. (2017). Inelastic damage as a mechanical precursor for the emplacement of saucer-shaped intrusions. *Geology*, *45*, 1099–1102. https://doi.org/10.1130/G39361.1

Hoek, E., Marinos, P., & Benissi, M. (1998). Applicability of the geological strength index (GSI) classification for very weak and sheared rock masses. The case of the Athens schist formation. *Bulletin of Engineering Geology and the Environment*, *57*(2), 151–160. https://doi.org/10.1007/s100640050031

Jackson, C. A.-L., Schofield, N., & Golenkov, B. (2013). Geometry and controls on the development of igneous sill-related forced folds: A 2-D seismic reflection case study from offshore southern Australia. *Geological Society of America Bulletin*, *125*(11-12), 1874–1890. https://doi.org/10.1130/b30833.1

Karlstrom, L., Paterson, S. R., & Jellinek, A. M. (2017). A reverse energy cascade for crustal magma transport. *Nature Geoscience*, *10*(8), 604–608. https://doi.org/10.1038/ngeo2982

Kavanagh, J. L., Boutelier, D., & Cruden, A. R. (2015). The mechanics of sill inception, propagation and growth: Experimental evidence for rapid reduction in magmatic overpressure. *Earth and Planetary Science Letters*, *421*, 117–128. https://doi.org/10.1016/j.epsl.2015.03.038

Kavanagh, J. L., Menand, T., & Sparks, R. S. J. (2006). An experimental investigation of sill formation and propagation in layered elastic media. *Earth and Planetary Science Letters*, *245*(3-4), 799–813. https://doi.org/10.1016/j.epsl.2006.03.025

Magee, C., Bastow, I. D., van Wyk de Vries, B., Jackson, C. A.-L., Hetherington, R., Hagos, M., & Hoggett, M. (2017). Structure and dynamics of surface uplift induced by incremental sill emplacement. *Geology*, *45*(5), 431–434. https://doi.org/10.1130/g38839.1

Malthe-Sørenssen, A., Planke, S., Svensen, H., & Jamtveit, B. (2004). Formation of saucer-shaped sills, In C. Breitkreuz & N. Petford, *Physical geology of high-level magmatic systems* (pp. 215–227). *Geological Society, London, Special Publications*, 234. https://doi.org/10.1144/gsl.sp.2004.234.01.13

McCaffrey, K. J. W., & Petford, N. (1997). Are granitic intrusions scale invariant? *Journal of the Geological Society*, *154*(1), 1–4. https://doi.org/10.1144/gsjgs.154.1.0001

Merle, O. (2015). The scaling of experiments on volcanic systems. *Frontiers in Earth Science*, *3*(26). https://doi.org/10.3389/feart.2015.00026

Merle, O., & Borgia, A. (1996). Scaled experiments of volcanic spreading. *Journal of Geophysical Research: Solid Earth*, *101*(B6), 13805–13817. https://doi.org/10.1029/95JB03736

Michaut, C. (2011). Dynamics of magmatic intrusions in the upper crust: Theory and applications to laccoliths on Earth and the Moon. *Journal of Geophysical Research: Solid Earth*, *116*, B05205. https://doi.org/10.1029/2010JB008108

Montanari, D., Corti, G., Sani, F., Del Ventisette, C., Bonini, M., & Moratti, G. (2010). Experimental investigation on granite emplacement during shortening. *Tectonophysics*, *484*(1-4), 147–155. https://doi.org/10.1016/j.tecto.2009.09.010

Petford, N., Kerr, R. C., & Lister, J. R. (1993). Dike transport of granitoid magmas. *Geology*, *21*(9), 845–848. https://doi.org/10.1130/0091-7613(1993)021%3C0845:dtogm%3E2.3.co;2

Phillips, W. J. (1974). The dynamic emplacement of cone sheets. *Tectonophysics*, *24*(1-2), 69–84. https://doi.org/10.1016/0040-1951(74)90130-9

Pollard, D. D., & Johnson, A. M. (1973). Mechanics of growth of some laccolithic intrusions in the Henry mountains, Utah, II: Bending and failure of overburden layers and sill formation. *Tectonophysics*, *18*(3-4), 311–354. https://doi.org/10.1016/0040-1951(73)90051-6

Polteau, S., Mazzini, A., Galland, O., Planke, S., & Malthe-Sørenssen, A. (2008). Saucer-shaped intrusions: Occurrences, emplacement and implications. *Earth and Planetary Science Letters*, *266*(1-2), 195–204. https://doi.org/10.1016/j.epsl.2007.11.015

Ranalli, G. (1995). *Rheology of the Earth*. London: Springer Science & Business Media.

Rodriguez Monreal, F., Villar, H. J., Baudino, R., Delpino, D., & Zencich, S. (2009). Modeling an atypical petroleum system: A case study of hydrocarbon generation, migration and accumulation related to igneous intrusions in the Neuquen Basin, Argentina. *Marine and Petroleum Geology*, *26*(4), 590–605. https://doi.org/10.1016/j.marpetgeo.2009.01.005

Roman, D. C., Power, J. A., Moran, S. C., Cashman, K. V., Doukas, M. P., Neal, C. A., & Gerlach, T. M. (2004). Evidence for dike emplacement beneath Iliamna Volcano, Alaska in 1996. *Journal of Volcanology and Geothermal Research*, *130*(3-4), 265–284. https://doi.org/10.1016/S0377-0273(03)00302-0

Roman-Berdiel, T., Gapais, D., & Brun, J. P. (1995). Analogue models of laccolith formation. *Journal of Structural Geology*, *17*(9), 1337–1346. https://doi.org/10.1016/0191-8141(95)00012-3

Rubin, A. M. (1993). On the thermal viability of dikes leaving magma chambers. *Geophysical Research Letters*, *20*(4), 257–260. https://doi.org/10.1029/92GL02783

Scaillet, B., Holtz, F., & Pichavant, M. (1997). Rheological properties of granitic magmas in their crystallization range. In J. L. Bouchez, D. H. W. Hutton, & W. E. Stephens (Eds.), *Granite: From segregation of melt to emplacement fabrics* (pp. 11–29). Dordrecht, Netherlands: Springer. https://doi.org/10.1007/978-94-017-1717-5_2

Scheibert, J., Galland, O., & Hafver, A. (2017). Inelastic deformation during sill and laccolith emplacement: Insights from an analytic elasto-plastic model. *Journal of Geophysical Research: Solid Earth*, *122*, 923–945. https://doi.org/10.1002/2016JB013754

Schellart, W. P. (2000). Shear test results for cohesion and friction coefficients for different granular materials: Scaling implications for their usage in analogue modelling. *Tectonophysics*, *324*(1-2), 1–16. https://doi.org/10.1016/S0040-1951(00)00111-6

Schmiedel, T., Breitkreuz, C., Görz, I., & Ehling, B.-C. (2015). Geometry of laccolith margins: 2D and 3D models of the Late Paleozoic Halle volcanic complex (Germany). *International Journal of Earth Sciences*, *104*(2), 323–333. https://doi.org/10.1007/s00531-014-1085-7

Schmiedel, T., Kjoberg, S., Planke, S., Magee, C., Galland, O., Schofield, N., … Jerram, D. A. (2017). Mechanisms of overburden deformation associated with the emplacement of the Tulipan sill, mid-Norwegian margin. *Interpretation*, *5*(3), SK23–SK38. https://doi.org/10.1190/INT-2016-0155.1

Spacapan, J. B., Galland, O., Leanza, H. A., & Planke, S. (2017). Igneous sill and finger emplacement mechanism in shale-dominated formations: A field study at Cuesta del Chihuido, Neuquén Basin, Argentina. *Journal of the Geological Society*, *174*, 422–433. https://doi.org/10.1144/jgs2016-056

Spence, D. A., & Turcotte, D. L. (1985). Magma-driven propagation of cracks. *Journal of Geophysical Research: Solid Earth*, *90*(B1), 575–580. https://doi.org/10.1029/JB090iB01p00575

Sun, Q., Wu, S., Cartwright, J., Wang, S., Lu, Y., Chen, D., & Dong, D. (2014). Neogene igneous intrusions in the northern South China Sea: Evidence from high-resolution three dimensional seismic data. *Marine and Petroleum Geology*, *54*, 83–95. https://doi.org/10.1016/j.marpetgeo.2014.02.014

Thorey, C., & Michaut, C. (2016). Elastic-plated gravity currents with a temperature-dependent viscosity. *Journal of Fluid Mechanics*, *805*, 88–117. https://doi.org/10.1017/jfm.2016.538

Ventsel, E., & Krauthammer, T. (2001). *Thin plates and shells: Theory, analysis, and applications*. New York: CRC Press. https://doi.org/10.1201/9780203908723

Wilson, P. I. R., McCaffrey, K. J. W., Wilson, R. W., Jarvis, I., & Holdsworth, R. E. (2016). Deformation structures associated with the Trachyte Mesa intrusion, Henry Mountains, Utah: Implications for sill and laccolith emplacement mechanisms. *Journal of Structural Geology*, *87*, 30–46. https://doi.org/10.1016/j.jsg.2016.04.001

A.5 Talks, posters, and co-authored publications

Talks

Schmiedel, T., Galland, O., *Dynamics of sub-volcanic systems in sedimentary basins and related mechanisms of host rock deformation*. Invited talk Utrecht University TecLab, Utrecht/Netherlands.

Schmiedel, T., Kjoberg, S., Planke, S., Magee, C., Galland, O., Schofield, N., Jackson, C.A.-L., Jerram, D.A., *Mechanisms of overburden deformation associated with the emplacement of the Tulipan sill, mid-Norwegian margin*. EGU General Assembly 2017, Vienna/Austria.

Schmiedel, T., Kjoberg, S., Planke, S., Magee, C., Galland, O., Schofield, N., Jackson, C.A.-L., 2017. *Mechanisms of overburden deformation associated with the emplacement of the Tulipan sill, mid-Norwegian margin*. 32rd Nordic Geological Winter Meeting 2017, Oslo/Norway.

Schmiedel, T., Galland, O., Breitkreuz, C., *The control of host rock strength on sill and laccolith emplacement*. GeoMod 2016, Montpellier/France.

Schmiedel, T., Galland, O., Planke, S., *Multidisciplinary research on magmatic intrusions and their associated overburden deformation*. Invited talk Imperial College 2016, London/UK.

Posters

Haug, Ø.T., Galland, O., Souloumiac, P., Souche, A., Guldstrand, F., Schmiedel, T., 2018. *Inelastic damage as a mechanical precursor for the emplacement of saucer-shaped intrusions*. 33rd Nordic Geological Winter Meeting 2018, Coppenhagen/Denmark.

Schmiedel, T., Galland, O., Breitkreuz, C., *The Control of Host Rock Strength on Sill and Laccolith Emplacement: Insights from Quantitative Laboratory Models*. GeoHazard Day 2018, Oslo/Norway.

Schmiedel, T., Galland, O., Breitkreuz, C., *The Control of Host Rock Strength on Sill and Laccolith Emplacement: Insights from Quantitative Laboratory Models*. IAVCEI Scientific Assembly 2017, Portland/USA.

Co-authored Publications

Palma, O., Burchardt, S., Galland, O., Schmiedel, T., Jerram, D.A., Mair, K., Leanza, H.A., (in prep.). *Structure and evolution of the plumbing system of an andesitic-dacitic volcano – Example of the Upper Miocene Chachahuén Volcano, southern Mendoza Province, Argentina.*

Galland, O., Bertelsen, H.S., Eide, C.H., Guldstrand, F., Haug, Ø.T., Leanza, H.A., Mair, K., Palma, O., Planke, S., Rabbel, O., Schmiedel, T., Souche, A., Spacapan, J.B., (2018). *Storage and Transport of Magma in the Layered Crust-Formation of Sills and Related Flat-Lying Intrusions*, in: Burchardt, S. (Ed.), Volcanic and Igneous Plumbing Systems, 1st ed, Elsevier, 111-136. doi: 10.1016/B978-0-12-809749-6.00005-4

Galland, O., Schmiedel, T., Bertelsen, H., Guldstrand, F., Haug, Ø.T., Souche, A., 2018. *Geomechanical Modeling of Fracturing and Damage induced by Igneous Intrusions: Implications for Fluid Flow in Volcanic Basins*, X Congreso de Exploración y Desarrollo de Hidrocarburos (conference proceeding). Instituto Argentino del Petróleo y el Gas, Mendoza, 1-16

Haug, Ø.T., Galland, O., Souloumiac, P., Souche, A., Guldstrand, F., Schmiedel, T., Maillot, B., 2018. *Shear versus tensile failure mechanisms induced by sill intrusions – Implications for emplacement of conical and saucer-shaped intrusions*. Journal of Geophysical Research - Solid Earth 123, 1-20. doi: 10.1002/2017JB015196

Haug, Ø.T., Galland, O., Souloumiac, P., Souche, A., Guldstrand, F., Schmiedel, T., 2017. *Inelastic damage as a mechanical precursor for the emplacement of saucer-shaped intrusions*. Geology 45, 1099-1102. doi: 10.1130/G39361.1